Multifluid Shock Waves in Molecular Clouds

Andrew Lehmann

Supervisor: Prof. Mark Wardle
Co-Supervisor: Dr. Birendra Pandey

MACQUARIE
University
SYDNEY·AUSTRALIA

February 18, 2017
A thesis submitted for the degree of Doctor of Philosophy in the Department of Physics and Astronomy and Faculty of Science and Engineering

Statement of Originality

The material presented in this thesis is original (except where cited) and has not been submitted to any university.

Each of Chapters 2 to 5 is a journal article that has been reformatted for the thesis. My co-authors in all these projects contributed general discussions for the work and the simulation results in chapter 3, but the development of code, analysis and interpretation of results, and writing was led by me.

The foundation of the work in chapter 2 was laid prior to starting this PhD, which includes developing the minimal functioning code and initial analysis. Everything after (and including) the section "Rotational Lines" was begun during the PhD, but the previous sections were also updated and expanded upon. This article has been published in *The Monthly Notices of the Royal Astronomical Society* (MNRAS), Volume 455, Issue 2, under the title *Signatures of fast and slow magnetohydrodynamic shocks in turbulent molecular clouds* (Lehmann and Wardle, 2016). Chapter 3 has been published in MNRAS, Volume 463, Issue 1, under the title SHOCKFIND - *An algorithm to detect the turbulence-driven shock waves in magnetohydrodynamic simulations* (Lehmann et al., 2016). Finally, chapter 5 has been submitted to MNRAS under the title *Two-fluid dusty shocks: simple benchmarking problems and applications to protoplanetary discs*.

Andrew Lehmann
February 18, 2017

Typeset in LaTeX 2_ε.

Abstract

Nonthermal linewidths in molecular clouds reveal the presence of highly supersonic turbulence, which inevitably dissipates by a network of shock waves. A multifluid treatment of these shocks is necessitated by low ionization fractions and strong magnetic field gradients.

In this thesis, a two-fluid model of magnetised radiative shocks is developed in which neutrals are heated by ion-neutral friction and cooled by ro-vibrational molecular lines. The structure of fast and slow magnetohydrodynamic shocks are compared at velocities of the order of the Alfvén velocity, appropriate for shocks driven by turbulence. Slow shocks are hotter than fast shocks at the same velocity, and their radiative signatures fit observations of infrared dark clouds in the Milky Way and giant molecular clouds near the Galactic Centre. An algorithm is developed to characterise the shocks in simulations of molecular cloud turbulence. Both fast and slow shocks are present, and the distributions of shock speeds, Alfvénic Mach numbers and preshock conditions are used to produce synthetic emission maps of CO and to predict the volume of shock-heated gas.

Finally, two-fluid dusty gas shocks in protoplanetary discs are considered. Two distinct shock solutions analogous to C- and J-type magnetised shocks are identified and these shocks are ideal benchmarking problems for numerical codes seeking to simulate dusty gas in protoplanetary discs. In addition, a J-type dusty shock is used to model the accretion shock above protoplanetary discs. Two-fluid effects are most important for grains larger than 1 μm, and dust emission from the shock is sensitive to the dust-to-gas ratio of the infalling material.

Acknowledgments

The four years of work put into this thesis could not be possible without the support of other people. My motivation, health and sanity was supplied, rejuvinated and maintained by many others to whom I'd like to express my gratitude here.

I greatly appreciate the guidance of my supervisors Mark and Pandey. Thanks for the interesting projects, for the stimulating conversations, for keeping me on track, for challenging me to figure it out. Additional thanks goes to Christoph for your encouragement and mentoring even though I wasn't your student.

Without distractions provided by friends, I don't see how I could have stayed sane throughout these years. I would like to especially thank my regular coffee companions Shane, James (also for the computer wizardry), Colin, Danica, Vincent and Chris for indulging my escapist speculation. For the adventures that took my mind away from stressful work to the beautiful Australian wilderness, I thank Dean, Joao, Erik, Tiffany, Glen, Reece and Matt.

To my parents and siblings (and siblings in law), thank you for the constant encouragement. Your enthusiasm restored me when things weren't working. I hope this makes you proud.

Finally, without the love and support of my better half Christina none of this would have happened, and it wouldn't be worth it anyway.

For Christina, my love.

Contents

Appendices

Chapter 1

Introduction

The interstellar medium, comprising all the material in a galaxy not locked up in stars or stellar remnants, is a complex system of varying physical conditions. Its structure and characteristics are governed by a wide variety of physical processes. Supernovae blast waves produce a hot ionized medium, which cools predominantly by emitting X-rays (McCray and Snow, 1979; Spitzer, 1990). A warm atomic medium is heated by ultraviolet starlight from newly formed stars and cooled by atomic line emission (Wolfire et al., 1995; Hollenbach and Tielens, 1999). The coldest phase, composed of dense molecular clouds, is shielded from ionizing radiation by dust grains, penetrated by relativistic cosmic-rays (Gredel et al., 1989) and stirred up from the inside by protostellar outflows and jets (Mac Low and Klessen, 2004). Large scale motions may also be driven by shear due to galactic rotation (Fleck, 1981). This diversity of physical conditions and processes ensures studies of the interstellar medium remain challenging and interesting.

Despite the complexity of the interstellar medium, stars form almost exclusively in just one phase: the dense molecular clouds. Determining the precise conditions of this phase is vitally important to constrain the physical processes that govern star formation. Magnetic fields, turbulence and stellar feedback have been identified as key processes to explain different aspects of the structure and evolution of molecular clouds, but open problems remain. It is still relatively unknown exactly what controls, for example, the rate at which stars form and the distribution of stellar masses at birth (see reviews by Hennebelle and Falgarone, 2012; Krumholz, 2014a).

Molecular clouds are dynamic, violent objects with a number of situations giving rise to shock waves. In regions of densely packed molecular clouds such as near the centres of galaxies, cloud-cloud collisions produce shocks that strongly disturb each cloud (Takahira et al., 2014). Supernovae blast waves disperse a cloud from the inside (Kim and Ostriker, 2015), or compress a cloud from the outside triggering the formation of new stars. Supersonic turbulence, driven by expanding HII regions and supernovae (Mac Low and Klessen, 2004), provides nonthermal pressure to

support against gravitational collapse, but is eventually dissipated by a network of shocks (Basu and Murali, 2001). In the densest clumps, gravitationally accelerated material passes through an accretion shock as it settles onto a protoplanetary disc (Shu et al., 1987). At a later stage of protostellar evolution, bipolar outflows or jets launched from the disc shock the surrounding medium (Lada, 1985; Bally, 2016). Detailed studies of the ubiquitous shock waves can therefore shed light on many aspects of molecular cloud evolution and star formation.

Shock waves are typically considered as simple discontinuities in the fluid variables as a high pressure region drives material into a low pressure region (e.g. de Hoffmann and Teller, 1950; Kennel et al., 1989). The material is viscously heated inside the shock front, and the flow behind this front cools due to radiation from a variety of atoms, molecules and dust grains. Accurately modeling the radiative cooling is not only important to properly model the structure of the shock—because the fluid density and velocity will be coupled to its temperature—but also to provide signatures of the shock parameters such as its velocity and preshock chemical composition, which in turn gives information about the gas being shocked.

In certain conditions single fluid treatments of shock waves are inaccurate. In a partially ionized fluid, magnetic pressure gradients lead to a decoupling of the neutrals and ions within a shock front (Mullan, 1971; Draine, 1980). Similar decoupling occurs between gas particles and dust grains above a critical grain size (Carrier, 1958; Kriebel, 1964). In these circumstances a single-fluid description does not accurately predict the temperature of coolants because it will overlook the frictional heating due to the relative velocities of the decoupled fluid components. It may also miss chemical pathways opened up by the increased kinetic energy from the relative velocities of reaction products (Flower et al., 1985). Thus a multifluid description (e.g. Draine, 1986) is needed to accurately model both the structure of shock waves and their radiative signatures.

The focus of this thesis is on two-fluid treatments of low-velocity magnetised shocks in turbulent molecular clouds and dusty accretion shocks in protoplanetary discs. In the remainder of this introduction, I give an overview of turbulent molecular clouds, considering their observed properties and theoretical models in the context of low-velocity shocks; and the early stages of star formation, in which protoplanetary discs are deeply embedded by infalling dust and gas. Throughout the introduction I will highlight the multifluid nature of these systems. This introductory chapter concludes with an outline of the structure of the thesis.

1.1 Turbulent Molecular Clouds

1.1.1 Typical Conditions

The densest, coldest phase of the interstellar medium is contained within giant molecular cloud complexes. In the disc of the Milky Way, molecular clouds are observed with the following characteristic properties. The clouds are composed almost entirely of molecular hydrogen (H_2), with trace amounts of other molecules and dust grains. Adopting the convention of Bergin and Tafalla (2007), they range in size from 2–15 pc, have gas temperatures of $\sim$10 K and average number densities between 10^2 and 10^3 cm^{-3}. In these conditions the sound speed is $c_s \sim 0.2$ km s^{-1}. The clouds are also threaded by large scale magnetic fields with strengths of the order of $\sim 10\mu$G. In addition, they contain $10^3 - 10^4$ M$_\odot$ of material, with only a small fraction ($\lesssim$5%) of this eventually collapsing to form stars (e.g. Myers et al., 1986) before the cloud is dispersed in 3–30 Myr (Blitz and Shu, 1980; Shu et al., 1987).

Most of a molecular cloud's material cannot be observed, because the lowest-lying allowable rotational transition of H_2 ($J = 2 - 0$ quadrupole transition) lies 510 K above the ground state, well above the cold cloud temperatures. Observers have therefore relied on indirect means of measuring the properties of molecular clouds. The most commonly observed molecule has been carbon monoxide (CO), which radiates in low-J rotational lines very easily due to collisional excitation with H_2. A contour map of the CO J=1-0 emission from a typical molecular cloud is shown in Fig. 1.1. The map shows the clumpy, filamentary spatial structure of molecular clouds.

Molecular line radiation is not only a tracer of H_2, it is also important for setting the thermal balance of molecular clouds. Cosmic-ray ionization is the dominant heating process as dust-attenuation and H_2 self-shielding efficiently blocks UV radiation from all but the edges. The cosmic-ray heating rate is balanced by CO cooling due to low-lying rotational lines at $\sim$10 K, giving the typical temperature of molecular clouds.

Linewidths are typically observed to be much larger ($\sim 1-10$ kms^{-1}) than can be explained by thermal broadening (e.g. Larson, 1981; Solomon et al., 1987). Fig. 1.2 shows an example of broad linewidths of CO emission from two molecular clouds. The linewidth, Δv, of a cloud of size L is observed to obey a power-law relation $\Delta v \propto L^\alpha$. The power-law index was initially measured as $\sim$0.38 (Larson, 1981), reminiscent of the Kolmogorov scaling of turbulent eddy velocities, v, with respect to the eddy size, l: $v \propto l^{1/3}$ (Kolmogorov, 1962). This law arises in incompressible turbulence when considering how kinetic energy cascades down from large scale motions to small scale motions until the energy is lost to heat. The power law follows

Figure 1.1 removed due to copyright

Figure 1.1: A CO $J = 1 \rightarrow 0$ emission map of molecular clouds in the Orion-Monoceros region. Image taken from Wilson et al. (2005).

assuming the energy transfer rate does not depend on the size of the motion considered. The assumption of incompressibility is inapplicable to interstellar clouds, and the assumption of homogeneity is broken by magnetic fields (discussed in the next section) providing a directionality in clouds. Hence it is unclear whether turbulence in molecular clouds should even resemble the model from Kolmogorov. However, extensions of the Kolmogorov theory into the compressible regime have had some success. Kritsuk et al. (2007) find that the original Kolmogorov laws hold for the density weighted fluid velocity, $\rho^{1/3}\mathbf{v}$, in simulations of compressible hydrodynamic turbulence. The scaling of this quantity appears to hold in the power spectrum and has been confirmed by other authors (Kritsuk et al., 2009; Price and Federrath, 2010; Federrath, 2013).

Subsequent observations of molecular cloud linewidths discovered a steeper relation to the cloud size, with exponents ranging from 0.48–0.65 (Leung et al., 1982; Myers, 1983; Sanders et al., 1985; Solomon et al., 1987; Ossenkopf and Mac Low, 2002; Brunt and Heyer, 2002; Heyer and Brunt, 2004). This steeper relation has been interpreted as resulting from the *supersonic* nature of the molecular cloud turbulence (Vázquez-Semadeni et al., 1997). Supersonic flows have a large scale dissipative mechanism in shock waves, which compress and heat the gas. This means

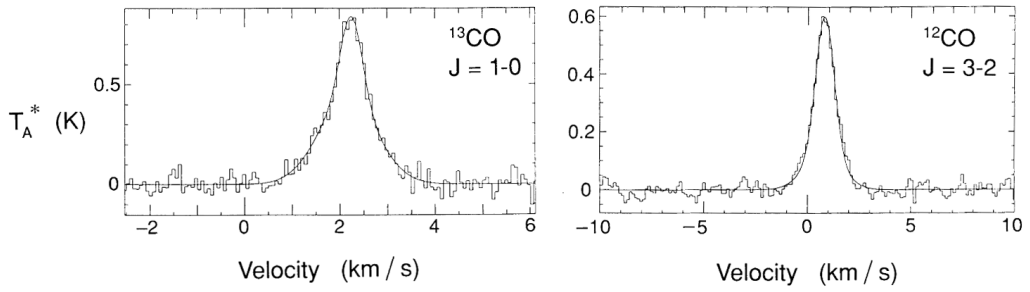

Figure 1.2: Typical line profiles of CO line emission from two molecular clouds. Figure taken from Falgarone and Phillips (1990).

there is less energy available to cascade down to smaller motions, so that there are preferentially more high velocity motions than in subsonic turbulence.

The velocity dispersion, measured from the linewidth, gives a measure of the turbulent kinetic energy. It is generally found that this is of the order of the gravitational potential of a cloud, and so the turbulence must be dynamically important to the evolution of molecular clouds. At large scales turbulence provides a non-thermal pressure support against gravitational collapse of the whole cloud, however it may also be important in triggering collapse to form protostars at small scales (Mac Low and Klessen, 2004). In fact, the distribution of stellar masses at birth, the initial mass function (IMF), can be explained if one assumes that protostars form in the density enhancements caused by shock waves (Padoan et al., 1997; Padoan and Nordlund, 1999, 2002). If shock waves set the initial conditions for star formation, then detailed shock models provide observational tests for this theory of the IMF (Holdship and Viti, 2016).

The turbulence interpretation of the large nonthermal linewidths was initially controversial because such highly supersonic motions should dissipate too quickly to be sustainable (Goldreich and Kwan, 1974). The timescale for turbulent decay is on the order of the time it takes a strong shock to traverse a cloud. This timescale turns out to be much shorter than the assumed long lifetime of molecular clouds. Thus a constant supply of driving energy would be required to maintain the turbulent motions, and a source of such energy needed to be discovered. On the other hand, short cloud lifetimes have been proposed where a small fraction of a cloud quickly forms stars before stellar feedback disperses the remaining gas (Elmegreen, 2000, 2007; Mac Low and Klessen, 2004). Alternatively, the hydromagnetic nature of molecular clouds may alter this result.

1.1.2 Alfvénic Turbulence

In an ionized fluid of mass density ρ, containing a magnetic field with strength B, the fluid has a characteristic speed of wave motions, $v_{\rm A} = B/\sqrt{4\pi\rho}$, called the Alfvén velocity. Zeeman splitting of molecular line emission, while challenging to observe, has been used to measure line-of-sight magnetic field strengths in some molecular clouds. Crutcher et al. (2010) compiled observations of the Zeeman effect from OH (Crutcher, 1999; Troland and Crutcher, 2008), CN (Falgarone et al., 2008), and HI (Heiles and Troland, 2004), and found magnetic field strengths in clouds that give Alfvén velocities of the order of the velocity dispersion of the cloud. This result suggests that magnetic fields will be dynamically important.

Alfvén waves are incompressible modes of an MHD fluid, and so the addition of a magnetic field provided a promising avenue to extend the lifetime of turbulence. For an MHD wave interpretation of molecular cloud turbulence, the particles of a molecular cloud have to be well coupled to the magnetic field. Only charged particles are directly coupled to the field via the Lorentz force, so some minimum amount of ionization is required to couple the neutral particles to the charged particles via collisions. In molecular clouds, cosmic-ray protons penetrate the dense gas to collisionally ionize a fraction of gas. The resulting electrons can further ionize nearby particles. This cascade transfers energy to the cloud and sets the overall ionization rate. Typical molecular clouds have cosmic-ray ionization rates $\zeta \sim 10^{-16}$ s^{-1} H^{-1}, leading to ionization fractions of about 1 part per 10^6 (Hollenbach et al., 2012). In addition, the Alfvén velocity must be large compared to the gas sound speed in the medium. These conditions were outlined by Arons and Max (1975), who also discovered that for MHD waves with wavelengths small compared to the cloud size, friction of the neutrals on the charged particles damp out the waves at timescales much shorter than the lifetimes of clouds, thus requiring a driving source of the waves if they are to be responsible for supporting the cloud. On the other hand, long wavelength MHD waves corresponding to oscillations of large subregions of a cloud do not damp out as quickly. For example, Alfvén waves propagating along the direction of the magnetic field are the longest living mode (Zweibel and Josafatsson, 1983). Friction between the neutral and ion components of the gas provides a constant damping but steepening of the wave profiles into shock waves dominates the dissipation of this mode.

The presence of shock waves is an inescapable outcome of supersonically turbulent molecular clouds, whether or not a magnetic field is included. As a primary source of dissipation, shocks determine the decay timescale of turbulence and therefore the lifetime of a cloud. In simulations of compressible MHD turbulence, Stone et al. (1998) found that the inclusion of a magnetic field did not significantly lengthen the decay timescale compared to hydrodynamical turbulence. As in the hydrodynamic case, shock waves were found to be an important energy sink, accounting for

around half of the dissipation turbulent kinetic energy. The cascade of turbulent energy from large scale motions to small results in a distribution of shock velocities. Smith et al. (2000b) found that weak shocks in a large range of velocities were responsible for the majority of dissipation in simulations of decaying turbulence. In contrast, a small range of stronger shocks dissipated turbulence that was being driven (Smith et al., 2000a). The heating of compressed gas in a thin post-shock region uniquely drives chemistry and radiative cooling. Thus the radiative characteristics and chemical signatures of turbulent dissipation will be strongly shaped by the detailed cooling and chemistry in shocks. This is the primary motivation for the MHD shock models presented in chapter 2 and chapter 4. In the next section, I review previous studies of MHD shock waves.

1.1.3 Magnetohydrodynamic Shock Waves

For a purely hydrodynamic (i.e. nonmagnetic) shock wave, in the frame of reference comoving with the shock—called the shock frame—the preshock fluid flows with speed v_s towards a thin, viscous shock front faster than the sound speed c_s and undergoes an effectively discontinuous transition to below the sound speed across the shock front. Conservation of mass, momentum and energy imply that in this situation the pressure and temperature will also undergo discontinuous jumps.

In an ideal MHD fluid three linear wave modes are supported, the fast, intermediate and slow waves. The six ways for a fluid to transition across these speeds allows for three distinct families of shocks. Fast MHD shocks cross the fast wave speed only, intermediate shocks cross the intermediate wave speed (but could cross the others), and slow shocks cross the slow wave speed only. Single fluid treatments of fast shocks including detailed microphysics have been used to study interstellar shocks (e.g. Kwan et al., 1977; Hollenbach and McKee, 1979), but the other families have been largely ignored. Intermediate and slow shocks have sub-Alfvénic velocities—$v_{\rm A} \lesssim 10$ km s^{-1} in molecular clouds—and so are far less luminous than the fast shocks typically studied with velocities in the tens of km s^{-1} (e.g. Draine and Katz, 1986a; Neufeld and Dalgarno, 1989; Smith and Brand, 1990). However, turbulent dissipation is dominated by shocks with velocities of the order of the cloud velocity dispersion, so the sub-Alfvénic shocks can have comparable luminosities to fast shocks.

Molecular clouds are penetrated by cosmic-rays which produce an ionized component of the order of 1 part per million. The ionized component decouples from the neutral component due to strong magnetic field gradients so that a two-fluid treatment of shock waves is required. With such a treatment Mullan (1971) and Draine (1980) discovered that fast shock fronts are not necessarily discontinuous. Fast waves in the ion fluid can travel ahead of the shock front, collisionally heating the neutral fluid in a "magnetic precursor". If the magnetic field is stronger

than some critical strength, the precursor completely smooths the shock front allowing for all the fluid variables to transition continuously to their post-shock values. Such a shock is called a C-type shock—in contrast to a J-type shock with a jump discontinuity—and has been extensively studied in various interstellar medium conditions. Before C-type shocks were discovered, one-fluid treatments of shocks in molecular clouds had the problem of being too hot. These shocks would heat up the gas beyond the dissociation temperature of H_2 for velocities $v_s \gtrsim 24$ km s^{-1} (Kwan et al., 1977; Hollenbach and McKee, 1980), contradicting observations of this molecule at high velocities ($\gtrsim 30$ km s^{-1}) in molecular regions. C-type shocks solved this problem because they heat up the gas more gently than J-type shocks. Thus a primary motivation for C-type shock studies was to explain low temperatures in moderate to high velocity shocks ($v_s \gtrsim 10$ km s^{-1}) produced by violent events. In addition, C-type shocks have been used to explain the observed overabundance of the CH^+ molecule with respect to other chemical models of diffuse clouds (e.g. Draine and Katz, 1986b; Flower and Pineau Des Forêts, 1998). Finally, the large relative velocities of ion and neutral species can increase sputtering and shattering of dust grains in shocks caused by protostellar outflows, explaining observed large abundances of gas phase SiO (e.g. Flower et al., 1996; Schilke et al., 1997; Guillet et al., 2007).

Previous studies considered single shocks at high velocities to model emission from large-scale coherent structures like expanding ionization fronts or supernovae blast waves. In contrast, supersonic turbulence in molecular clouds decays by a network of shocks at very low velocities ($v_s \lesssim 5$ km s^{-1}). The only study (before this one) of MHD shocks at these velocities is that of Pon et al. (2012). They consider observational diagnostics due to turbulent dissipation in *fast* MHD shocks. Comparing these models to observations of anomalously bright high-J CO line emission has been more successful than models of photon-dominated regions (Pon et al., 2014, 2015; Larson et al., 2015). In chapter 2, the first published two-fluid models of *slow* MHD shocks are presented. Slow shocks are hotter than fast shocks of the same velocity and observations of high-J CO lines are better fit by shocks from this family. Recent high-J CO line measurements have shown that both fast and slow MHD shocks are consistent with the observational data (Pon et al., 2016a).

While this is observational evidence for the presence fast and slow MHD shocks in turbulent regions, it is still unclear what mixture of shock families *should* be produced by MHD turbulence. Balsara (1996) and Tilley and Balsara (2011) find that the fast and Alfvèn modes are strongly damped by ion-neutral collisions leaving the slow modes to propagate with little damping. Thus nonlinear steepening into slow shocks might be expected to preferentially occur in molecular clouds. In chapter 3, I present the first published prediction of the mixture of shock families in a turbulent molecular cloud. We also use the detailed shock models of chapter 2 to produce

synthetic maps of turbulent dissipation in MHD shocks. The goal of that work is to eventually tie the radiative characteristics of shocks to the parameters of turbulence. Simulations of molecular clouds have shown that the star formation rate and efficiency depend on whether the turbulence is solenoidally or compressively driven (Federrath and Klessen, 2012, 2013), and that the stellar initial mass function is sensitive both to non-ideal MHD effects such as ambipolar diffusion (McKee et al., 2010) and to the driving and Mach number of the turbulence (Hennebelle and Chabrier, 2009, 2013; Hopkins, 2013). If these and other parameters of turbulence could be linked to distributions of shock waves, then shock modeling can provide observational tests of models of excitation and decay of turbulence.

1.2 Dusty Protoplanetary Discs

1.2.1 Dust-gas numerical codes

In molecular clouds and protoplanetary discs, dust is found to play a key role. Warm gas transfers energy to dust via collisions, which then cools via thermal radiation. This radiation, usually in the near-infrared, plays a significant thermodynamic role and allows observers to indirectly measure gas properties at higher resolution than molecular line emission usually at radio wavelengths. The formation of H_2 by gas phase chemical reactions is too inefficient to form the observed molecular fraction in molecular clouds. It has long been recognized that reactions on the surfaces of dust grains are required (Gould and Salpeter, 1963). As a major source of opacity, dust attenuation helps shield the inner parts of molecular clouds from UV radiation (Hollenbach and Tielens, 1999). This attenuation is a key reason molecular clouds can cool down to 10 K (Glover and Clark, 2012), allowing for gravitational collapse to form protostars and protoplanetary discs. In these discs, the gaseous component rotates at sub-Keplerian velocities due to pressure gradients. The pressureless dusty component however, rotates at the Keplerian velocity and so the two fluids are decoupled. A multifluid approach is therefore key to accurately modeling these systems.

Thermal dust emission can be observed with infrared and submillimetre space telescopes like *Spitzer* (e.g. Stephens et al., 2014), *Herschel* (e.g. Launhardt et al., 2013), and *Planck* (e.g. Planck Collaboration et al., 2011), and next generation ground based telescopes like ALMA (e.g. ALMA Partnership et al., 2015). Observations of dust emission from protoplanetary discs with ALMA have discovered dust-cleared concentric rings (Isella et al., 2016) or cavities (Walsh et al., 2016). Such dust gaps have been explained as due to the presence of planets (e.g. Dipierro et al., 2015; Kanagawa et al., 2015) or to other effects such as dust-trapping in vortices (Ruge et al., 2016). To relate observations of dust to properties of gas, it is

crucially important to understand their coupled evolution.

The importance of coupled gas-dust modeling has motivated the development of numerical codes designed to simulate gas and dust in protoplanetary discs, as well as other astrophysical systems. Monaghan and Kocharyan (1995) extended the smoothed particle hydrodynamics code of Gingold and Monaghan (1977) to model dusty gas by treating the dust as a collisionless fluid coupled to the gas via drag. Hopkins and Lee (2016) also model dust in this way, by representing an ensemble of grains as a collection of 'superparticles' in the mesh-free, Lagrangian simulation code GIZMO (Springel, 2005; Hopkins, 2015). They found large dust-to-gas variations in turbulent molecular clouds and that dust filaments do not necessarily correlate with gas filaments. Paardekooper and Mellema (2006b) extend the Eulerian hydrodynamics code RODEO (Paardekooper and Mellema, 2006a) to solve the flow equations for both gas and dust. They show that dust-gaps are cleared more easily than gas-gaps in protoplanetary discs. The finite-difference MHD code PENCIL CODE (Brandenburg and Dobler, 2002) has been extended to model dust grains as individual particles in order to study the Kelvin-Helmholtz instability in protoplanetary discs (Johansen et al., 2006). This code was used to study the growth of boulders in turbulent protoplanetary discs (Johansen et al., 2007) and has recently been updated to treat stiff drag conditions (Yang and Johansen, 2016). Bai and Stone (2010b) implemented a hybrid particle-gas integration scheme into a grid-based code, ATHENA (Stone et al., 2008), designed to simulate compressible MHD. In their code, they consider dust particles coupled with gas via aerodynamic drag. Using this code, Bai and Stone (2010a) found that radial gradients of gas pressure in protoplanetary discs induce dust clumping leading to planetesimal formation.

Both grid-based (e.g. Johansen et al., 2006; Bai and Stone, 2010b) and particle-based smoothed particle hydrodynamics codes (e.g. Laibe and Price, 2012a; Lorén-Aguilar and Bate, 2014) have been used to study dusty gas flows in protoplanetary discs. However, Laibe and Price (2011) highlight a lack of simple analytic solutions to benchmark dusty gas codes in astrophysical conditions. In addition, existing methods innacurately reproduce the few analytic solutions in the limit of strong drag (Laibe and Price, 2012a). Having more simple analytic solutions is crucial in aiding the development of more accurate dusty gas codes. A common benchmarking test is the Sod shock-tube problem (Sod, 1978), in which a fluid is initially set up to contain a large discontinuity. The fluid variables are then evolved with time, and then compared to the analytic solution of the problem. In the pure hydrodynamical case, the simple initial discontinuity breaks up into a shock wave, rarefaction wave and a contact discontinuity. Unfortunately, in the two-fluid dusty gas case, there is no analytic solution to this problem. Fig. 1.3 shows the Sod shock-tube test performed with a numerical simulation of two-fluid dusty gas (Saito et al., 2003). This figure shows that while the two-fluid version of the test gives qualitatively

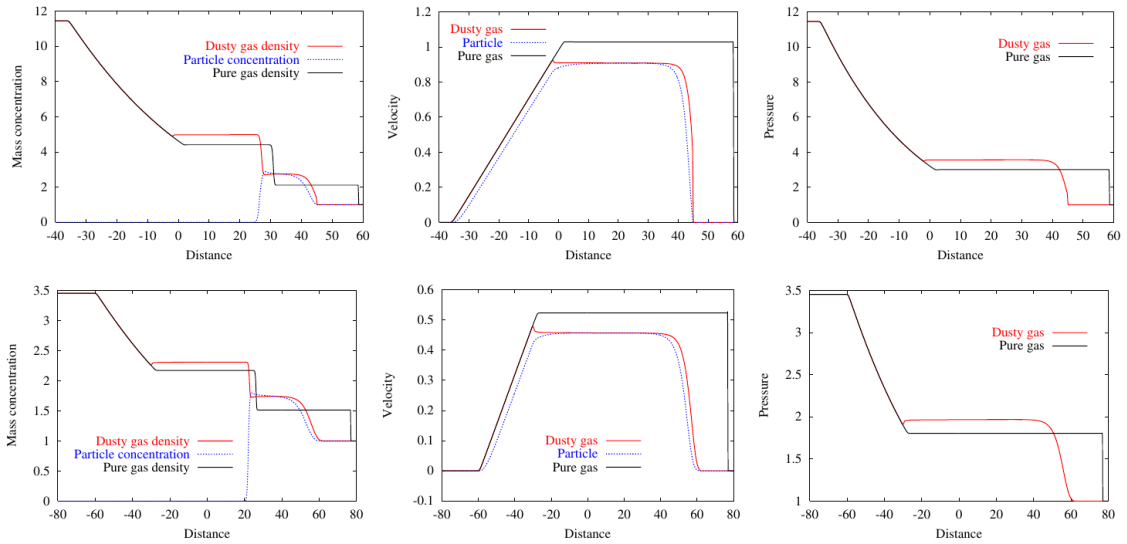

a Mass concentration **b** Velocity **c** Pressure

Figure 1.3: Sod shock-tube problem in a two-fluid dusty gas. Figure adapted from Saito et al. (2003). The upper and lower panels are for different initial discontinuities.

similar results to the pure hydrodynamical case, there are significant differences. With no analytic solution to compare to, it is not clear how dusty gas numerical codes are supposed to perform, so authors have resorted to comparing the results of this test against each other. Saito et al. (2003) notes, however, that a steady-state two-fluid shock structure reasonably fits one of the resulting components in this test problem.

In chapter 5, I extend the insight of Saito et al. (2003) by focusing on steady shocks as a simple test problem. Unlike the standard shock-tube tests, steady shocks comprise only one hydrodynamic component with a structure that can be computed from simply integrating the governing ordinary differential equations. The numerical simulation is also simple: drive a piston into a uniform medium by using reflective boundary conditions. The variables of the fluid traveling into this wall can be simply obtained from the jump conditions on the combined dust-gas fluid. This simple test can be used to benchmark how numerical codes behave with different dust-to-gas ratios, drag coefficients and different forms of the drag, e.g. linear, quadratic, Epstein and so on.

1.2.2 Shocks and Protostellar Evolution

Two-fluid dusty shocks are not just ideal benchmarks for numerical codes. When a pocket of gas in a molecular cloud collapses under gravity to form a low-mass star, the protostar evolves through four phases shown schematically in Fig. 1.4. In these

phases, the protostar emits distinct infrared spectral energy distributions (SED) due to different physical conditions of their constituent dust, until the pre-main sequence star dominates as a hot black-body.

The initial self-gravitating clump (Fig. 1.4a) results from a turbulent density enhancement which may be due to a shock. In this phase, the protostar is surrounded by an envelope of cold dust, emitting as a cold black body (~ 30 K) to give a Class 0 protostellar SED.

Figure 1.4 removed due to copyright

Figure 1.4: Evolution of a protostar. Image taken from (Shu et al., 1987).

As the clump evolves, a centrifugally supported protoplanetary disc forms around the protostar (Fig. 1.4b). The whole structure is still surrounded by an envelope of material seen as a Class I SED now with some contribution from the stellar black-body. In the self-similar collapse model of Shu (1977) an inside-out collapse begins to takes place in this phase. This idealised model will never occur in detail, but provides a qualitative description of protostellar collapse that roughly holds true even in the presence of magnetic fields and rotation (Larson, 2003). Starting from the centre, material loses thermal support and starts to fall freely towards the density peak. A rarefaction wave then travels away from the centre at the speed of sound.

The infalling material must pass through an accretion shock before settling onto the protoplanetary disc. The initial density peak comprises a small fraction of the mass of the eventual protostar, with most of the mass accreted during these protostellar phases (Larson, 2003). This means that the chemical processing inside the accretion shock is largely responsible for the composition of the protoplanetary disc and protostar. Hence detailed modeling of this accretion disc is key to understanding the subsequent chemical evolution of protostars.

When the density and temperature grows enough, deuterium fusion begins. In this phase, seen as a Class IId SED, strong stellar winds or collimated jets from the disc eventually penetrate the dusty envelope to form bipolar outflows, as sketched in Fig. 1.4c. The detailed mechanism for launching jets from discs remains an open problem, though it is generally thought to involve magnetic fields. One popular model is the magnetocentrifugal theory, in which the accretion flow in the disc drags the magnetic field into a configuration that flings material vertically from the disc (Blandford and Payne, 1982). The outflows from this phase produce moderate to high velocity bow shocks ($v_s > 10$ km s^{-1}) when they run against the surrounding interstellar medium. Detailed chemistry in MHD shock models can probe the nature of the outflow (e.g. Flower et al., 2003; Flower and Pineau des Forêts, 2013; Holdship et al., 2016), and ultimately could test jet launching mechanisms.

In the final stage, sketched in Fig. 1.4d, the protostellar outflows have fully dispersed the envelope of infalling material, revealing the pre-main sequence star now powered by hydrogen fusion. The Class II SED characterising this phase is dominated by black-body radiation from the new star and sometimes showing an infrared excess due to the presence of a disc.

Shocks are found throughout the phases of protostellar evolution. Detailed studies of shocks can therefore shed light on a variety of physical processes important to star formation. In chapter 5 I show that a two-fluid dusty gas treatment is important to understanding the accretion shock that occurs in the phase shown in Fig. 1.4b. The simplified model shows the shock structure is sensitive to fluid parameters such as the dust-to-gas ratio and dust grain size. This motivates a detailed study of accretion shocks, given their importance in setting the initial composition of the protostellar material.

1.3 Structure of Thesis

In chapter 2, I numerically solve the equations of two-fluid MHD in order to investigate low-velocity ($v_s \lesssim 4$ km s^{-1}) steady-state, planar shock waves in molecular cloud conditions. A simplified model is used to highlight different families of MHD shock waves, and presents the first published two-fluid treatment of slow-mode MHD shocks. This kind of shock is observationally distinct from the well studied C-type

fast-mode shocks and a comparison with literature observational data shows evidence of slow-mode shocks in observed molecular clouds.

The detailed MHD shock models presented in chapter 2 motivates the study of which family of shocks we *expect* in turbulent molecular clouds. I address this question in chapter 3, which presents a publicly available algorithm, SHOCKFIND, to detect and characterise the MHD shocks in simulations. The algorithm is applied to a simulation of a turbulent molecular cloud, and I present the first prediction for the mixture of MHD shock families produced by supersonic turbulence. I use the results of the detailed shock modeling (chapter 2) to create synthetic maps of observables and quantify the effects of shock heating in clouds.

In chapter 4 I update and extend the previous shock models (chapter 2) to include more heating and cooling processes. I also extend the chemical network to include nitrogen- and sulphur-bearing species, and model new kinds of reactions. These models are used to study chemical anomalies in the unusual molecular clouds located near the centre of the Milky Way galaxy. The high temperatures of clouds found in this region have been explained as due to the dissipation of turbulence. In this chapter I provide chemical predictions of this dissipitation, provided by the unique chemical processing taking place within shock fronts.

A multi-fluid treatment of dusty shock waves is presented in chapter 5. These shocks are ideal benchmarking tests for numerical codes seeking to simulate dusty gas. I show there are two distinct shock solutions analogous to C- and J-type MHD shocks. I also apply these shocks to the study of accretion shocks in the early stages of protostellar disc formation. Two-fluid effects are found to be important for large dust grains ($\gtrsim$1 μm), and the peak dust temperature probes the dust-to-gas ratio of the infalling material. These results suggests that more detailed treatments of this shock could be fruitful in uncovering the initial composition of material that will eventually form planets.

Finally, I summarise the thesis and consider future directions in Chapter 6.

Chapter 2

Fast and slow magnetohydrodynamic shocks

Abstract

The character of star formation is intimately related to the supersonic magnetohydrodynamic (MHD) turbulent dynamics of the molecular clouds in which stars form. A significant amount of the turbulent energy dissipates in low velocity shocks. Fast and slow MHD shocks differ in how they compress and heat the molecular gas, and so their radiative signatures reveal distinct physical conditions.

We use a two-fluid model to compare one-dimensional fast and slow MHD shocks propagating at low speeds (a few km/s). Fast shocks are magnetically driven, forcing ion species to stream through the neutral gas ahead of the shock front. This magnetic precursor heats the gas sufficiently to create a large, warm transition zone where all the fluid variables smoothly change in the shock front. In contrast, slow shocks are driven by gas pressure, and neutral species collide with ion species in a thin hot slab that closely resembles an ordinary gas dynamic shock.

We consider shocks at velocities $v_s = 2{-}4$ km s^{-1} and preshock Hydrogen nuclei densities $n_{\rm H} = 10^2 - 10^4$ cm^{-3}. We include simple oxygen chemistry and cooling by CO, H_2 and H_2O. CO rotational lines above J = 6$\rightarrow$5 are more strongly excited in slow shocks. These slow shock signatures may have already been observed in infrared dark clouds in the Milky Way.

2.1 Introduction

Understanding the internal environment of the giant molecular clouds (GMCs) in which stars form is a necessary precursor to addressing the star formation rate and stellar initial mass function (e.g., Bergin and Tafalla, 2007; McKee and Ostriker, 2007). Large non-thermal linewidths observed in molecular lines (e.g., Larson, 1981; Solomon et al., 1987) have often been attributed to turbulent motions. Furthermore, the kinetic energy associated with these motions is generally found to be on the order of the gravitational potential energy, indicating the importance of turbulence as a dynamical component of molecular clouds. In addition, magnetic fields in GMCs give Alfvén velocities on the order of the observed velocity dispersions (e.g., Crutcher et al., 1993; Crutcher, 1999; Crutcher et al., 2010). This suggests that the turbulence in GMCs is magnetohydrodynamic (MHD) in nature.

The physics underlying the MHD turbulence of molecular clouds is intimately connected with properties of star formation (Mac Low and Klessen, 2004). For example, Federrath and Klessen (2012) and Federrath and Klessen (2013) use three dimensional MHD simulations to analyse different modes of turbulence by comparing compressive driving to solenoidal driving. They showed that the star formation rate and efficiency are both sensitive to these driving modes and Mach number variations. Hence it is desirable to discover observable distinctions between different modes of turbulence.

Supersonic turbulence dissipates via shock waves and vortices (Pety and Falgarone, 2000). In simulations of compressible MHD turbulence Stone et al. (1998) found that shock waves dissipated around 50% of the turbulent energy. The heating of compressed gas in a thin postshock region uniquely drives chemistry and radiative cooling. Thus the radiative characteristics of turbulent dissipation will be strongly shaped by cooling in shocks. Furthermore, Smith et al. (2000b) found that weak shocks in a large range of velocities were responsible for the majority of dissipation in simulations of decaying MHD turbulence. In contrast, a small range of stronger shocks dissipated turbulence that was being driven (Smith et al., 2000a). Hence radiative signatures of shocks could be used to distinguish between these two scenarios.

The observational signatures of the low-velocity shocks that dominate dissipation of MHD turbulence have only recently been considered. Pon et al. (2012) considered C-type fast MHD shocks travelling at speeds of 2–3 km s^{-1} perpendicular to the magnetic field and computed the abundances and emission of H_2, CO and H_2O. By comparing CO rotational line emission from these shocks to those produced in photodissociation regions (PDRs), they found that fast shocks dominate the emission in transitions above $J = 5 \rightarrow 4$. Lesaffre et al. (2013) take a statistical approach by computing observational diagnostics due to a distribution of C- and J-type fast,

perpendicular, MHD shocks at velocities ranging from 3–40 km s^{-1}. They use these shocks to explain the radiation from a turbulent wake formed by a galaxy collision in Stephan's Quintet.

Anomalously bright CO lines above $J = 5 \rightarrow 4$ have been recently observed towards Milky Way molecular clouds (e.g., Pon et al., 2014, 2015; Larson et al., 2015) and from warm molecular gas in external galaxies (e.g., Kamenetzky et al., 2012; Pellegrini et al., 2013). These studies all conclude that PDR models are unable to reproduce the bright high-J CO lines and all suggest MHD shock waves as the heating mechanism. The shock models used or referred to in these studies (Flower and Pineau Des Forêts, 2010; Pon et al., 2012) and other studies of shocks in interstellar clouds (e.g. Draine and Katz, 1986b; Hollenbach and McKee, 1989; Chapman and Wardle, 2006) all consider *fast* MHD shocks. MHD fluids can, however, support three kinds of shocks: fast, intermediate and slow. Unfortunately no study has identified which kinds of shocks would be produced by MHD turbulence. One of the goals of our work is to motivate the classification of MHD shocks in turbulent molecular clouds.

Ideal MHD assumes a fully ionized gas in which the magnetic field is frozen. Molecular clouds are in fact only weakly ionized and the magnetic field acts on the neutral fluid via the ionized fluid. A two-fluid description is therefore more appropriate to molecular cloud studies. Early work by Lithwick and Goldreich (2001) and Lazarian et al. (2004) highlighted the importance of two-fluid effects on the turbulent cascade. Recently it has become feasible to run high resolution three dimensional two-fluid MHD simulations. For example, Meyer et al. (2014) use simulations to show that observations of linewidth differences between line emission from neutral and ion species can be accounted for by two-fluid effects. Furthermore, Burkhart et al. (2015) use simulations to show that the Alfvènic modes do not necessarily dissipate at the ambipolar diffusion scale. They also confirm the analytic results of Balsara (1996) and Tilley and Balsara (2011) that in molecular cloud conditions, the fast and Alfvèn modes are strongly damped by ion-neutral collisions leaving the slow modes to propagate with little damping. Thus nonlinear steepening into slow shocks might be expected to preferentially occur in molecular clouds. In addition, slow shocks reach far higher peak temperatures than fast shocks for two reasons. Firstly, the heating timescale in fast shocks is determined by the long ion-neutral collision timescale while in slow shocks is determined by the short neutral-ion collision timescale. As the cooling timescale of the gas lies between these two, the gas being overrun by fast shocks remains at low temperatures whereas it quickly heats up within slow shocks. Secondly, as we show in section 2.2 the gas in fast shocks necessarily loses some of its kinetic energy to strengthening the magnetic field while in slow shocks it does not. Thus slow shocks have more energy available to heat the gas.

In this chapter, we solve the steady, plane parallel two-fluid MHD equations to model shocks that propagate at any angle to the magnetic field. In section 2.2 we elucidate some of the basic differences of fast and slow MHD shocks. We describe our computational scheme in section 2.3. In section 2.4 we compare fast and slow shocks in the low-velocity regime with molecular cloud conditions. We discuss their radiative characteristics and implications for interpreting emission from turbulent molecular gas. Finally, in section 2.5 we show how these signatures might be used to interpret observations.

2.2 Theory

Cosmic rays streaming through the interstellar medium weakly ionize molecular clouds, generating an ion fluid that interpenetrates the neutral particles. A two-fluid MHD description is developed in section 2.2.1 with the ion fluid coupled to the magnetic field via the Lorentz force and to the neutral fluid via the collisional force, so that

$$\frac{\mathbf{J} \times \mathbf{B}}{c} = \alpha \rho_i \rho_n \left(\mathbf{v}_i - \mathbf{v}_n \right), \tag{2.2.1}$$

where α is the rate coefficient for elastic ion-neutral scattering and ρ and $\mathbf{v}$ are the density and velocity with subscripts i and n referring to ion and neutral fluids respectively. By considering the state of these fluids far away from the shock front, we illustrate how the various families of MHD shocks come about and highlight the different effects they have on the ambient magnetic field.

A simplified chemical model, in which two body reactions and photodissociation affect the abundances of coolants, is presented in section 2.2.2. Finally, the details of how those coolants radiate are outlined in section 2.2.3. Only rotational excitations of molecular species are considered because vibrational excitations do not become significant until temperatures reach $\gtrsim$ 1000 K, which are not achieved in the low velocity shocks computed here.

2.2.1 Two-Fluid MHD

Conservation equations

While turbulence is an inherently three-dimensional problem (e.g. Burkhart et al., 2015, and references therin), shock waves are extremely thin structures within a turbulent system. Hence we follow Draine (1986) by considering a stationary plane-parallel shock travelling in the z direction with the magnetic field initially lying in

the x–z plane. The governing equations of the ion fluid are

$$\frac{d}{dz}\left(\rho_i v_{iz}\right) = 0, \tag{2.2.2}$$

$$\frac{d}{dz}\left(\frac{B_z B_x}{4\pi}\right) = \alpha\rho_i\rho_n\left(v_{ix} - v_{nx}\right), \tag{2.2.3}$$

$$\frac{d}{dz}\left(\frac{B_x^2}{8\pi}\right) = -\alpha\rho_i\rho_n\left(v_{iz} - v_{nz}\right). \tag{2.2.4}$$

The neutral fluid equations are

$$\frac{d}{dz}\left(\rho_n v_{nz}\right) = 0, \tag{2.2.5}$$

$$\frac{d}{dz}\left(\rho_n v_{nz} v_{nx}\right) = \alpha\rho_i\rho_n\left(v_{ix} - v_{nx}\right), \tag{2.2.6}$$

$$\frac{d}{dz}\left(\rho_n v_{nz}^2 + P_n\right) = \alpha\rho_i\rho_n\left(v_{iz} - v_{nz}\right), \tag{2.2.7}$$

$$v_{nz}\frac{dP_n}{dz} + \gamma P_n\frac{dv_{nz}}{dz} = \left(\gamma - 1\right)\left(\Gamma - \Lambda\right), \tag{2.2.8}$$

where P_n is the neutral pressure, Γ is the heating function, Λ is the cooling function, and the internal energy $u = P_n/\left(\gamma - 1\right)$ for adiabatic index γ. Finally, the electromagnetic equations give

$$\frac{d}{dz}\left(v_{iz}B_x - v_{ix}B_z\right) = 0, \tag{2.2.9}$$

$$\frac{d}{dz}\left(B_z\right) = 0. \tag{2.2.10}$$

Solving for the internal structure of intermediate shocks requires equations analogous to equations (2.2.3) to (2.2.10) for the y-direction. We consider only fast and slow shocks here by ignoring this case. Far away from the shock front there is no velocity difference between the fluids. This means there is no frictional heating in those regions, and so the shocks satisfy the isothermal one-fluid jump conditions. The types of shocks allowed are therefore determined by the MHD signal speeds.

Shock Families

When considering small perturbations of density, pressure, the velocity field, and the magnetic field around time independent averages the equations of MHD allow for three linear wave modes: the fast, intermediate and slow waves. These waves

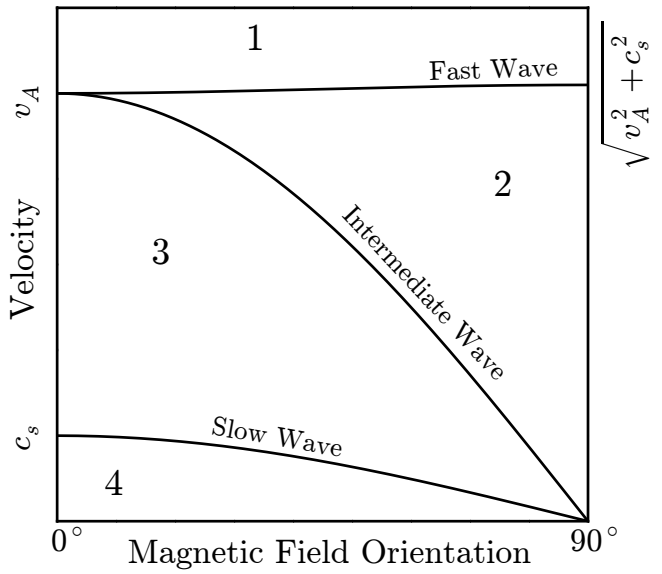

Figure 2.1: The phase velocities of linear MHD wave modes versus the angle between the magnetic field and direction of propagation of those modes for $v_A > c_s$. The wave speeds delineate the regions marked 1 to 4.

travel with phase velocities

$$f = \left(\frac{v_A^2 + c_s^2}{2} + \frac{1}{2}\sqrt{\left(v_A^2 + c_s^2\right)^2 - 4 v_A^2 c_s^2 \cos^2\theta} \right)^{1/2}, \tag{2.2.11}$$

$$i = v_A \cos\theta, \tag{2.2.12}$$

$$s = \left(\frac{v_A^2 + c_s^2}{2} - \frac{1}{2}\sqrt{\left(v_A^2 + c_s^2\right)^2 - 4 v_A^2 c_s^2 \cos^2\theta} \right)^{1/2}, \tag{2.2.13}$$

where $v_A = B/\sqrt{4\pi\rho}$ is the Alfvén velocity, $c_s = \sqrt{k_B T/\mu_m}$ is the isothermal sound speed with Boltzmann constant k_B and mean mass per particle $\mu_m = (7/3)\, m_H$, and θ is the angle between the magnetic field and the direction of propagation under consideration. These speeds are plotted as functions of θ in Fig. 2.1 for the case $v_A > c_s$ (the relevant case in molecular clouds).

In the frame of reference comoving with a shock front, the preshock fluid travels toward the shock front at a shock velocity v_s greater than one of the wave speeds. The three wave speeds demarcate four regions of fluid velocities marked 1 to 4 in Fig. 2.1. Inside of the shock front the fluid must transition down across a wave speed, which allows for six kinds of shock waves collected into three families: fast, intermediate and slow MHD shocks. Fast shocks are those that cross the fast wave speed only ($1 \to 2$), intermediate shocks cross the intermediate wave speed ($1 \to 3$, $1 \to 4$, $2 \to 3$ and $2 \to 4$), and slow shocks cross the slow wave speed only ($3 \to 4$).

Far ahead and far behind a shock where there is no friction between the fluids—and hence $\mathbf{v}_n = \mathbf{v}_i$—one can show from equations (2.2.2) to (2.2.10) that the product

$$\left(\frac{v_z^2 - i^2}{v_z}\right) B_x \tag{2.2.14}$$

is conserved across any shock. This can be used to emphasise some basic differences between the different kinds of shocks. Suppose, for simplicity that $B_x > 0$ in the preshock medium. Recall that a fast shock crosses the fast wave speed only, so that the term in parentheses remains positive but is reduced across the shock. Thus B_x must increase to compensate. In intermediate shocks, the velocity crosses the intermediate wave speed and so the term in parentheses switches sign across the shock. This implies that B_x must switch sign also. Finally, in slow shocks, the velocity crosses the slow wave speed only, so that the term in parentheses is negative and becomes further negative in the postshock medium. This means that B_x must decrease to compensate. These three effects on the magnetic field direction are shown schematically in Fig. 2.2.

The switch in sign of B_x in the intermediate shock is due to a rotation of the magnetic field within the shock front. As the field rotates out of the x-z plane, intermediate shocks require equations analogous to equations (2.2.3) to (2.2.10) for the y-direction. This case is ignored here because it is unclear whether steady state intermediate shocks are physically admissable (e.g., Wu, 1987; Falle and Komissarov, 2001). Furthermore, the $1 \rightarrow 3$ intermediate shock will resemble a fast shock as it crosses the fast speed, the heating in a $2 \rightarrow 4$ shock front will be dominated by a hydrodynamic jump as it crosses the sound speed—see section 2.3—and thus resemble a slow shock, the $2 \rightarrow 3$ shock will only weakly heat the gas as it resembles a rotational discontinuity, and finally the $1 \rightarrow 4$ shock will resemble a fast shock followed by a weak $2 \rightarrow 3$ shock followed by a slow shock, so our models should also roughly capture its structure (Kennel et al., 1989).

As the spacing of field lines is proportional to the magnetic field strength, one can see in Fig. 2.2 that the field strength increases across fast shocks and decreases across slow shocks. This means that some of the kinetic energy of a fast shock is converted into magnetic field energy. Hence, for slow shocks at the same velocity one expects there to be more energy available to heat the gas.

Governing Differential Equations

With some manipulation, equations (2.2.2) to (2.2.10) reduce to two ordinary differential equations determining changes in the x component of the magnetic field

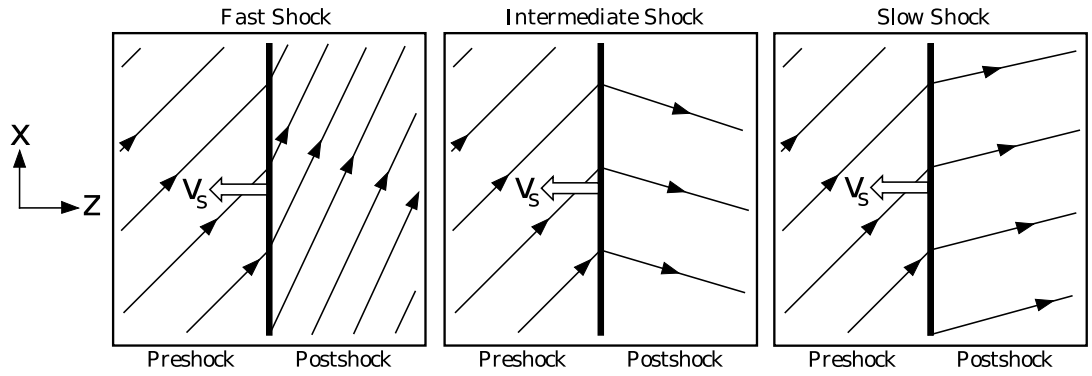

Figure 2.2: The effect on magnetic field orientation of the three classes of MHD shock waves. Fast shocks (left) increase the angle between the field and shock normal, intermediate shocks (middle) reverse the sign of the angle and slow shocks (right) decrease it.

and the neutral fluid temperature:

$$\frac{dB_x}{dz} = \frac{v_s^2 \alpha \rho_{i0} B_0^2}{v_A^2 B_z} \left(\frac{v_{ix} - v_{nx}}{v_{nz} v_{iz}} \right), \tag{2.2.15}$$

$$\frac{dT_n}{dz} = \frac{T_n (\gamma - 1)}{\rho_{n0} v_s^3 (v_{nz}^2 - \gamma \tau v_s^2)} \left(\left(\frac{v_{nz}^2}{\tau} - v_s^2 \right) (\Gamma - \Lambda) - \alpha \rho_i \rho_n (v_{iz} - v_{nz}) v_{nz} v_s^2 \right), \tag{2.2.16}$$

with the velocities

$$v_{nx} = \frac{v_A^2 B_z}{v_s B_0^2} (B_x - B_{x0}), \tag{2.2.17}$$

$$v_{ix} = \frac{v_{iz} B_x - v_s B_{x0}}{B_z}, \tag{2.2.18}$$

$$v_{nz} = \frac{v_s}{2} \left(\beta \pm \sqrt{\beta^2 - 4\tau} \right), \tag{2.2.19}$$

$$v_{iz} = \frac{v_s B_{x0} B_x + B_z (B_x v_{nx} + B_z v_{nz})}{B_0^2}, \tag{2.2.20}$$

the preshock Alfvén velocity

$$v_A = \frac{B_0}{\sqrt{4\pi \rho_{n0}}}, \tag{2.2.21}$$

and

$$\beta = 1 + \frac{k_B T_{n0}}{\mu_m v_s^2} + \frac{1}{2} \frac{v_A^2}{v_s^2} \frac{B_{x0}^2 - B_x^2}{B_0^2}, \tag{2.2.22}$$

$$\tau = \frac{k_B}{\mu_m v_s^2} T_n, \tag{2.2.23}$$

where a subscript 0 denotes preshock values.

equations (2.2.15) and (2.2.16) are not complete without specifying how energy leaves the gas via Λ and enters via Γ. The collisions between the ion and neutral fluids generate frictional heating at a rate

$$\Gamma_F = \alpha \rho_n \rho_i \left(\mathbf{v}_i - \mathbf{v}_n\right)^2 \tag{2.2.24}$$

per unit volume. In addition, we include cosmic-ray heating as a constant injection of energy chosen to balance the preshock cooling rate at 10 K.

The shock heated gas cools by radiating away heat energy stored in the rotational and vibrational modes of its constituents. These modes are collisionally excited, so that the cooling function must be a function of the densities of the coolants, the density of the colliding particles and the temperature of the gas. The abundances of coolants can change due to chemical reactions, and so we present a simple model for the oxygen chemistry occuring in the shock heated gas in the next section before specifying how that gas radiates in section 2.2.3.

2.2.2 Chemistry

Radiative cooling depends on the abundances of the coolants and hence chemical reactions influence the cooling of the gas. The dominant molecular coolants in molecular clouds are CO, H_2 and H_2O (e.g., Neufeld and Kaufman, 1993). Infrared dust emission is also an important cooling mechanism in cold molecular clouds, but in low-velocity shocks has been shown to be insignificant compared to molecular cooling (Pon et al., 2012). and the abundance of the latter is determined in this study by the set of eight reactions listed in Table 2.1, adopted from Wagner and Graff (1987). Previous models of the gas phase chemistry in interstellar environments—using more than 100 reactions—were found to be dominated by a small set of reactions (e.g., Iglesias and Silk, 1978). The reactions of Wagner and Graff are the subset of these dominant reactions that control the abundance of H_2O.

The change in the particle density of a neutral species M through the shock is given by

$$\frac{d}{dz}\left(n(M) v_{nz}\right) = S_M, \tag{2.2.25}$$

where S_M is the rate at which M is created or destroyed. $\sum S_M$ over all neutral species must be zero in order for equation (2.2.5) to remain true. The low densities of molecular clouds mean that only two body chemical reactions and photodissociation processes need to be considered. Two-body reaction rates between species A with particle density $n(A)$ and species B with particle density $n(B)$ take the form

$$k_{AB}(T) n(A) n(B) \text{ cm}^{-3} \text{ s}^{-1}, \tag{2.2.26}$$

Table 2.1: Reaction rate coefficient parameters.

No.	Reaction	α	β	γ
1	$O + H_2 \rightarrow OH + H$	3.14×10^{-13}	2.70	3150.0
2	$OH + H \rightarrow O + H_2$	6.99×10^{-14}	2.80	1950.0
3	$OH + H_2 \rightarrow H_2O + H$	2.05×10^{-12}	1.52	1736.0
4	$H_2O + H \rightarrow OH + H_2$	1.59×10^{-11}	1.20	9610.0
5	$OH + OH \rightarrow H_2O + O$	1.65×10^{-12}	1.14	50.0
6	$H_2O + O \rightarrow OH + OH$	1.85×10^{-11}	0.95	8571.0
7	$O + OH \rightarrow O_2 + H$	4.33×10^{-11}	-0.5	30.0
8	$O_2 + H \rightarrow O + OH$	2.61×10^{-10}	0	8156.0

Notes. The parameters for reaction 7 are taken from Wagner and Graff (1987) instead of RATE12.

where $k_{AB}(T)$ is a rate coefficient. The UMIST Database for Astrochemistry 2012 (RATE12) (McElroy et al., 2013) gives this coefficient in the form

$$k_{AB}(T) = \alpha \left(\frac{T}{300}\right)^{\beta} \exp\left(-\frac{\gamma}{T}\right) \text{ cm}^3 \text{ s}^{-1}, \tag{2.2.27}$$

where α, β and γ are constants. The values of these parameters for the reactions used are shown in Table 2.1. These rates are verified for the temperature range $200 - 2500$ K, so there is some uncertainty when extrapolating down to 10 K. In fact, for the reaction

$$O + OH \rightarrow O_2 + H \tag{2.2.28}$$

the rate coefficient parameters in the RATE12 database give a rate that diverges in the 10–100 K range. For this rate the parameters are taken from Wagner and Graff (1987). In Fig. 2.3, the rates are plotted against temperature. It can be seen that most of the rates only "turn on" at temperatures $T \gtrsim 60$ K, which is why the weak fast shocks considered here only negligibly affect the molecular abundances.

Photodissociation in molecular clouds is caused by ultraviolet radiation generated by secondary electrons in cosmic ray ionization events (Prasad and Tarafdar, 1983). The rates of photodissociation events per volume of species A with particle density $n(A)$ take the form

$$p_A \frac{\zeta_{CR}}{1-\omega} n(A) \text{ cm}^{-3} \text{ s}^{-1}, \tag{2.2.29}$$

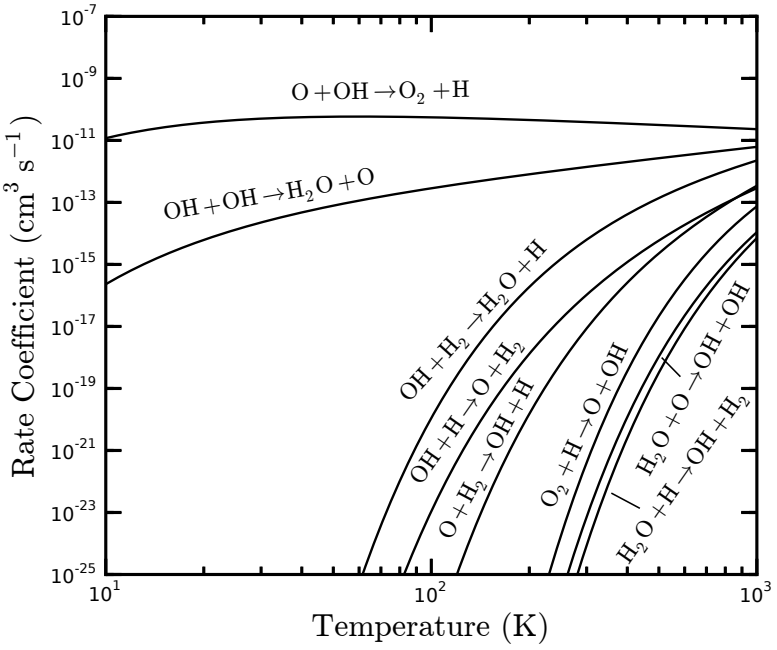

Figure 2.3: Reaction rate coefficients as a function of temperature.

where ζ_{CR} is the cosmic ray ionization rate, ω is the albedo of the dust grains found in molecular clouds and p_A is an efficiency constant. The ionization rate ζ_{CR} is set to 10^{-17} s^{-1}, the albedo w is set to 0.6, and the values of p_A for the reactions considered—taken from Gredel et al. (1989)—are shown in Table 2.2.

With these two rates and using the static, planar assumptions the abundance of species M relative to the hydrogen nuclei density $x_M = n(M)/n_H$ changes as

$$\frac{d}{dz}(x_M) = \frac{n_H^2}{n_0 v_s}\left(\sum k_{AB}(T)x(A)x(B) + \sum p_A \frac{\zeta_{CR}}{1-\omega}x(A)\right), \tag{2.2.30}$$

where n_0 is the preshock H-nuclei density and the sums are taken over reactions that either produce or destroy M.

The end result of this chemistry is to add five more differential equations—coupled to each other through densities and to equations (2.2.15) to (2.2.16) through temperature—to follow the abundances of H, O, OH, O_2 and H_2O. We follow Pon et al. (2012) in using an initial H_2O abundance of 10^{-7}, O abundance of 5.45×10^{-4} and a C abundance of 1.4×10^{-4} which is assumed to be entirely locked up in CO. The CO abundance is assumed to be constant throughout the shock, because it has a dissociation temperature higher than any temperature reached in these weak shocks. The initial H, OH and O_2 abundances are set to 10^{-4}, 10^{-12} and 10^{-10} respectively. H_2 abundance is then computed through the shock using $x_{H_2} = (1/2)(1 - x_H)$.

Table 2.2: Photodissociation rate efficiency.

Reaction	p_A
$H_2O + Photon \rightarrow OH + H$	971
$OH + Photon \rightarrow O + H$	509
$O_2 + Photon \rightarrow O + O$	751

Notes. Photodissociation rate efficiencies taken from Gredel et al. (1989).

2.2.3 Cooling

The cooling function of Neufeld and Kaufman (1993) is adopted for this model. This uses an escape probability to account for the effects of reabsorption by the surrounding media on the rotational level populations. Collisions with H_2 are the only excitations considered as the abundance of H_2 in molecular clouds is orders of magnitude above the next most abundant molecular species. The power radiated by CO, H_2O and H_2 in a wide range of conditions is expressed in terms of a rate coeffecient $L_{\rm M}$ defined such that the power radiated per unit volume by species M is

$$\Lambda_{\rm M} = n({\rm M})n({\rm H_2})L_{\rm M}, \tag{2.2.31}$$

where $L_{\rm M}$ is a function of H_2 density, temperature and an optical depth parameter $\tilde{N}({\rm M})$. $\tilde{N}({\rm M})$ is a correction factor that accounts for reabsorption of radiation by the same species in the surrounding gas. It depends on the geometry of the system in question, the density of M and the local velocity gradient. The expression for a plane-parallel slab of thickness d and characteristic velocity difference Δv,

$$\tilde{N}({\rm M}) = \frac{n({\rm M})d}{9\Delta v}, \tag{2.2.32}$$

is used here. $L_{\rm M}$ is then expressed with a four parameter analytic fit to its density dependence

$$\frac{1}{L_{\rm M}} = \frac{1}{L_0} + \frac{n({\rm H_2})}{L_{LTE}} + \frac{1}{L_0}\left(\frac{n({\rm H_2})}{n_{1/2}}\right)^{\alpha}\left(1 - \frac{n_{1/2}L_0}{L_{LTE}}\right), \tag{2.2.33}$$

where L_0 is the low density limit of the cooling rate coefficient, L_{LTE} is the luminosity per molecule with the level population in local thermodynamic equilibrium and $n_{1/2}$ is the H_2 density at which the cooling rate coefficient is half of L_0. L_0 is a function of temperature only while L_{LTE}, $n_{1/2}$ and α are functions of temperature and $\tilde{N}({\rm M})$.

Preliminary isothermal shocks were computed in order to gain an estimate on the values of d and Δv, and these values checked for self consistency against the results when cooling was included. The average value of $n(M)$ through the shock was used. H_2 is optically thin in all interesting astrophysical conditions, so L_{H_2} does not depend on equation (2.2.32).

The values of L_0, L_{LTE}, $n_{1/2}$ and α for CO, H_2O and H_2 are taken from Neufeld et al. (1995) in the temperature range $T = 10$–100 K, and from Neufeld and Kaufman (1993) in the range $T = 100$–2000 K. We combine the parameters in the $T = 10$–100 K range using an ortho-to-para H_2O ratio of 3:1, which was already assumed in the $T = 100$–2000 K range. The values of L_0, $n_{1/2}$ and α for CO are inconsistent at $T = 100$ K between, with a 20% difference in L_0 and up to 40% difference in $n_{1/2}$ and 100% difference in α. We use the mean of the inconsistent tabulated values at $T = 100$ K, and then used a cubic spline interpolation over the combined tables to define a smooth cooling function over the whole temperature range.

2.3 Numerical Integration

The core of this problem are the first order ordinary differential equations which take the form:

$$\frac{dB_x}{dz} = f_1\left(z, B_x, T\right), \tag{2.3.1}$$

$$\frac{dT}{dz} = f_2\left(z, B_x, T\right), \tag{2.3.2}$$

for f_1 and f_2 defined by equations (2.2.15) and (2.2.16). They must be solved simultaneously with the abundance derivatives which are coupled to these two through their dependence on temperature. When supplied with initial conditions, these equations can be integrated to give B_x, T and the abundances as functions of z. The open source PYTHON module *scikits.odes*[1] was used, which solves initial value problems for ODEs using variable-order, variable-step, multistep methods.

The initial conditions are stationary states—in that their z derivatives are zero—so integrating from these points changes nothing. A perturbation must be added to these initial conditions in the form

$$B_x = B_{x0} + \delta B_x e^{\lambda_x z}, \tag{2.3.3}$$

$$T = T_0 + \delta T e^{\lambda_T z}, \tag{2.3.4}$$

before integrating. The effect of the perturbation can be understood by linearising the differential equations (2.2.15) and (2.2.16). It is illuminating to look at the

[1] https://github.com/bmcage/odes

isothermal case—where $\gamma = 1$—so that only the B field derivative remains. In this case we get the eigenvalue

$$\lambda_x = \frac{\alpha\rho_{i0}}{v_s}\frac{(v_s^2 - f^2)(v_s^2 - s^2)}{v_A^2(v_s^2 - c_s^2)}, \tag{2.3.5}$$

where f and s are the fast and slow signal speeds defined in section 2.2.1. λ_x determines whether the perturbation of B_x grows or decays. By replacing the preshock variables with their postshock counterparts, the eigenvalue can also be used to explore the region of solution space near postshock states.

For fast shocks, the preshock state is in region 1 of Fig. 2.1 so that $v_s > f > i > c_s > s$. This means λ_x is positive so that B_x grows. This describes an unstable stationary point, where any perturbation away from the initial condition grows. The postshock state is in region 2 so that $f > v_f > i > c_s > s$ where v_f is the final velocity. This means λ_x is negative so that this state is a stable stationary point. In section 2.2.1, we noted that the fast shock increases B_x, hence a positive perturbation of the initial B_x is all that is required to finish at the fast postshock state.

For slow shocks, the preshock state is in region 3 of Fig. 2.1 so that $f > i > v_s > c_s > s$ in the supersonic case. This means λ_x is negative and this state is a stable stationary point. Hence there is no way to leave the supersonic slow preshock state in a continuous fashion like in C-type fast shocks. The slow solution is further complicated by a singularity in the equations when crossing the sound speed ($v_{nz} \to c_s$), as a manipulation of equation (2.2.8) gives

$$\frac{dv_{nz}}{dz} = \frac{(\gamma - 1)(\Gamma - \Lambda) - \alpha\rho_n\rho_i(v_{iz} - v_{nz})v_{nz}}{\rho_n(c_s^2 - v_{nz}^2)}. \tag{2.3.6}$$

We cross this sonic point by inserting a gas dynamic jump in the neutrals determined by the hydrodynamic jump conditions:

$$\frac{v_2}{v_1} = \frac{\gamma - 1}{\gamma + 1} + \frac{2}{\gamma + 1}\frac{1}{M^2}, \tag{2.3.7}$$

$$\frac{T_2}{T_1} = \left(1 + \frac{2\gamma}{\gamma + 1}(M^2 - 1)\right)\frac{M^2(\gamma - 1) + 2}{M^2(\gamma + 1)}, \tag{2.3.8}$$

where $M^2 = \rho_1 v_1^2/\gamma P_1$ and v_2 and T_2 are the neutral z velocity and temperature immediately after the gas dynamic jump. The slow postshock state lies in region 4 of Fig. 2.1 so that $f > i > c_s > s > v_f$ and λ_x is negative. This means this state is a stable stationary point, and so jumping across the sound speed (via equation (2.3.7)) will allow the solution to smoothly settle onto the slow postshock state.

For slow shocks with a subsonic preshock state, $f > i > c_s > v_s > s$ so that λ_x is positive and the stationary state is unstable. This means a perturbation that

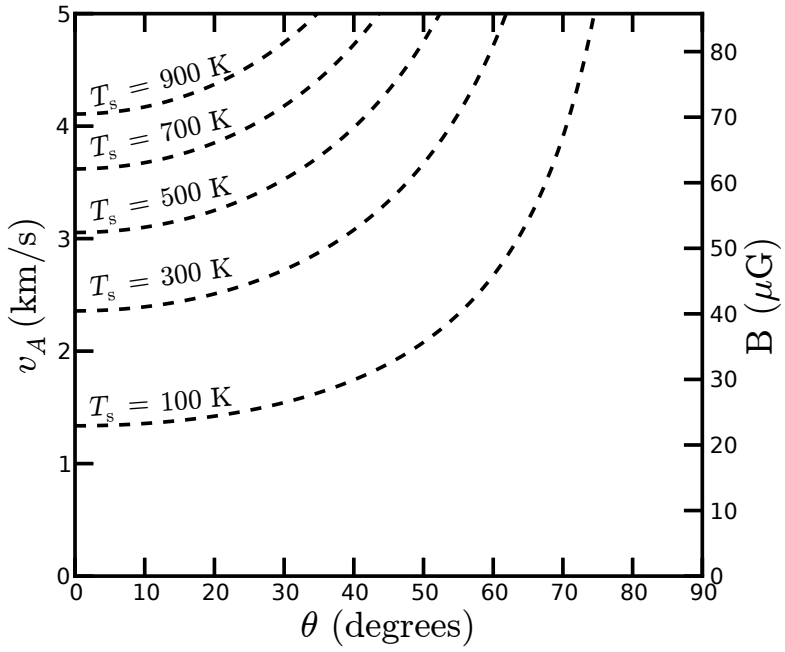

Figure 2.4: Alfvén velocity versus magnetic field orientation, with dashed lines of constant intermediate speed $v_A \cos\theta$ that allow slow MHD shocks to reach the peak temperatures shown. The magnetic field strength on the second vertical axis assumes preshock density $n_0 = 10^3$ cm^{-3}.

reduces B_x will grow smoothly until the solution reaches the slow postshock state. Such a shock is a C-type slow MHD shock, and will be ignored here because it requires high sound speeds and therefore high temperatures that are not obviously relevant for molecular cloud studies.

2.4 Results

Here we compare a set of shock models with parameters shown in Table 2.3. The turbulent cascade of energy ensures the dissipation is dominated by low-velocity shocks, so we follow Pon et al. (2012) in looking at velocities around 3 km s^{-1}. In Fig. 2.4, the Alfvén velocity is plotted against the magnetic field orientation θ with dashed lines of constant intermediate speed $i = v_A \cos\theta$ overlaid. The magnetic field strength on the second vertical axis is computed for a preshock density $n_0 = 10^3$ cm^{-3}. The intermediate speed is the upper bound of possible slow shock velocities—region 3 in Fig. 2.1—and so the dashed lines in Fig. 2.4 trace the minimum field strength required to get slow shocks with peak temperatures shown. We thus chose θ low enough to retain reasonable field strength values. At $\theta = 30°$, a 4 km s^{-1} slow

Table 2.3: Shock Parameters.

Parameters	v_s km/s	$\log \tilde{N}(CO)$ $\log\left(cm^{-2}\ (km/s)^{-1}\right)$	$\log \tilde{N}(H_2O)$
Fast Shocks, $\theta = 89.9°$			
$n_0 = 10^2$ cm^{-3}	2.0	15.9	11.7
$B_0 = 3$ μG	2.5	15.7	11.8
	3.0	15.6	11.9
	3.5	15.5	11.9
	4.0	15.5	11.9
$n_0 = 10^3$ cm^{-3}	2.0	15.8	12.7
$B_0 = 10$ μG	2.5	15.8	12.7
	3.0	15.8	12.6
	3.5	15.8	12.6
	4.0	15.5	12.3
$n_0 = 10^4$ cm^{-3}	2.0	15.9	12.8
$B_0 = 32$ μG	2.5	15.8	12.7
	3.0	15.8	12.8
	3.5	15.7	12.6
	4.0	15.7	12.6
Slow Shocks, $\theta = 30°$			
$n_0 = 10^2$ cm^{-3}	2.0	14.5	11.0
$B_0 = 25$ μG	2.5	14.5	11.0
	3.0	14.5	11.0
	3.5	14.5	11.4
	4.0	14.5	12.3
$n_0 = 10^3$ cm^{-3}	2.0	14.5	11.0
$B_0 = 80$ μG	2.5	14.5	11.0
	3.0	14.5	11.5
	3.5	14.5	12.6
	4.0	14.5	13.2
$n_0 = 10^4$ cm^{-3}	2.0	15.6	12.6
$B_0 = 253$ μG	2.5	15.7	12.7
	3.0	15.1	13.6
	3.5	15.0	14.6
	4.0	15.0	15.1

shock—which will heat the gas to ~ 857 K immediately after the neutral jump—requires an Alfvén velocity of ~ 4.6 km s^{-1}, which is fixed for all the slow shocks at different preshock densities. This gives magnetic field strengths in the range $B_0 = 25$–253 μG. Finally, $\tilde{N}$ was initially chosen for preliminary isothermal shocks, and then recomputed after each shock model for consistency. Table 2.3 shows the self consistent values of $\tilde{\mathrm{N}}(\mathrm{CO})$ and $\tilde{\mathrm{N}}(\mathrm{H_2O})$.

Structural characteristics

In Figs. 2.5 and 2.6 we compare fast and slow shock profiles of ion and neutral velocity, density, temperature, cooling rate and abundances for $v_s = 3$ km s^{-1}. The fast shock propagates at 89.9° to a 10 μG magnetic field, while the slow shock propagates at 30° to an 80 μG field. The preshock density $n_0 = 10^3$ cm^{-3} for both.

In the velocity profiles—upper panels of Figs. 2.5 and 2.6—the neutral and ion velocities in the shock propagation direction are the dashed and dotted lines respectively. These plots are in the frame of reference of the shock wave, and so velocities below the shock velocity represent fluid flowing ahead of the shock front in the lab frame, in which the shock wave travels to the left. Therefore, in the fast shock the ions stream ahead, imparting some of their momentum to the neutrals until both fluids are moving at the same speed in the postshock medium (on the right side of each plot).[2] This process is set by the long ion-neutral collision timescale and therefore happens smoothly over a large distance, and there is no viscous jump as seen in hydrodynamic shocks. In contrast, for the slow shock it is the neutrals that flow ahead of the ions that then get accelerated to the neutral velocity over a small distance—set by the fast neutral-ion collision timescale—giving slow shocks a much thinner structure than the fast shocks. The cooling timescale of the gas lies between the two collision timescales, and so slow shocks will reach higher peak temperatures than fast shocks at the same velocity.

The density profiles—solid black lines in the upper panels—similarly show large differences between the shocks. The fast shock weakly compresses the gas by a factor of ~ 7 in a simple, smooth manner. The slow shock has a complex density profile that ends with a compression ratio of ~ 300 and must be understood in conjunction with the temperature and cooling (see middle panel) taking place. It starts with the neutral jump, governed by equations (2.3.7) and (2.3.8), compressing the gas by a factor of ~ 4 and heating it to ~ 500 K. Combining equations (2.2.4) and (2.2.7) we get

$$\frac{d}{dz}\left(\rho_n v_{nz}^2 + P_n + \frac{B^2}{8\pi}\right) = 0, \tag{2.4.1}$$

[2]Note also that in the postshock region, the velocity must remain above the intermediate and slow MHD speeds, as a fast shock must be a $1 \rightarrow 2$ shock (see discussion in section 2.2.1).

where we identify each term as effective pressure terms: ram pressure $P_{ram} = \rho_n v_{nz}^2$, gas pressure $P_{gas} = P_n = nk_BT$ and magnetic pressure $P_{mag} = B^2/8\pi$. As the neutrals lead the ions in the slow shock, equation (2.2.4) implies that the magnetic pressure must drop. The velocity drop causes the ram pressure to drop, and so gas pressure must increase, which is shown in the third panel of Fig. 2.6. Efficient line emission from CO and H_2 causes the temperature to quickly decrease, so to compensate the density must increase. This occurs smoothly in the $\sim 0.1 \times 10^{16}$ cm after the initial jump, until the density reaches a plateau at a compression ratio of ~ 300. The density finally settles as the neutral and ion velocities equalise.

While the velocity and density structural differences are large, the observational implications are sensitive to the temperature and cooling rate profiles shown in the second panels of Figs. 2.5 and 2.6. These panels show that the peak temperatures differ by an order of magnitude with the slow shock peaking at ~ 487 K and the fast shock peaking at ~ 50 K. At this temperature, the fast shock causes CO emission only slightly above the background level. The slow shock is hot enough to emit significantly in lines of CO and H_2, and also in H_2O above the CO background emission. The fourth panels of Figs. 2.5 and 2.6 also show that the slow shock drives more chemistry than the fast shock due to its high temperature. The strong H_2O emission in the slow shock is partially due to this increase in its abundance.

Following the pressure terms—in the third panels of Figs. 2.5 and 2.6—through the shocks provides an intuitive understanding of the fundamental differences between fast and slow shocks. In the fast shock, the magnetic pressure (dotted lines) is higher in the postshock region than in the preshock region. As the gas pressure (solid lines) is neglible everywhere in this shock it is understood to be magnetically driven, where the high P_{mag} region pushes into the low P_{mag} region. The ion fluid is strongly coupled to the magnetic field, and so the ions are pushed forward ahead of the neutrals. This is why the ions lead the neutrals in the velocity profile. This situation is reversed in the slow shock, where a high gas pressure region pushes the neutrals through the ions. In this case, the ion coupling to the magnetic field deforms it and increases the separation between field lines, which reduces the field strength.

Comparison of fluxes

The cooling discussed in section 2.2.3 can be used to search for observational differences between the kinds of shocks. Integrating the cooling rate—middle panels of Figs. 2.5 and 2.6—through the shocks gives the flux emitted in the direction of the shock normal. In Fig. 2.7, we compare the CO, H_2 and H_2O fluxes of all the fast and slow shocks in Table 2.3.

The CO flux is similar between both kinds and across the velocity range. The H_2 flux is much more temperature sensitive and is therefore stronger in the slow

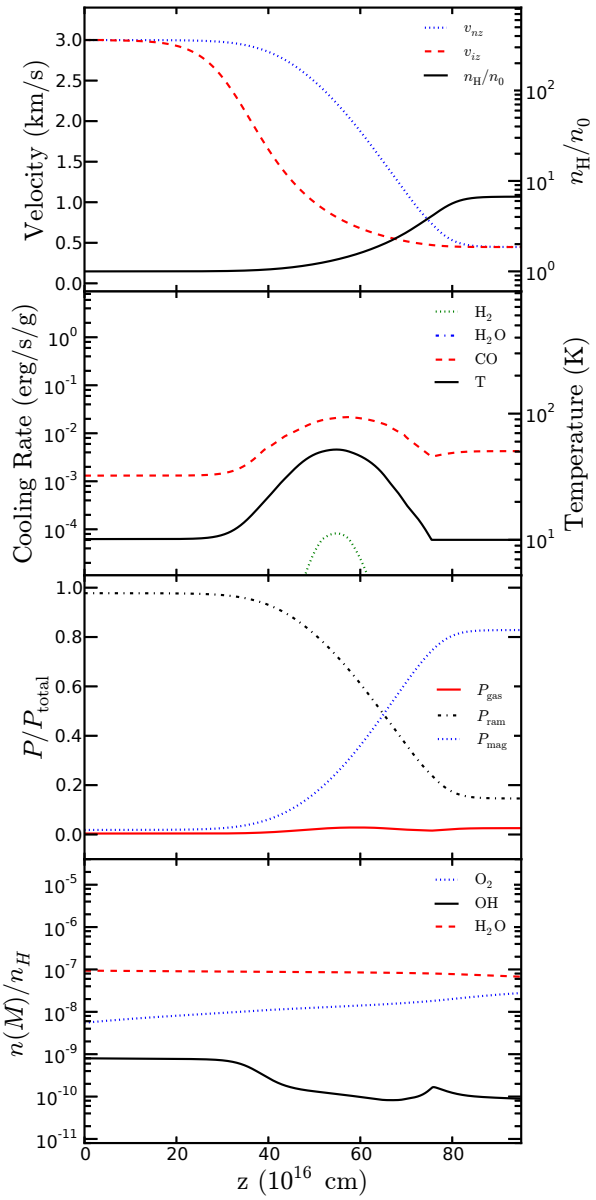

Figure 2.5: Profiles for a $v_s = 3$ km s^{-1} fast MHD shock propagating through a medium with initial number density $n_0 = 10^3$ cm^{-3} at 89.9° to a 10 μG magnetic field. The first panel shows the velocity and density profiles, the second panel shows the temperature and cooling rate profiles, the third panel shows the gas, ram and magnetic pressure profiles, and the fourth panel shows the abundances of selected oxygen molecules.

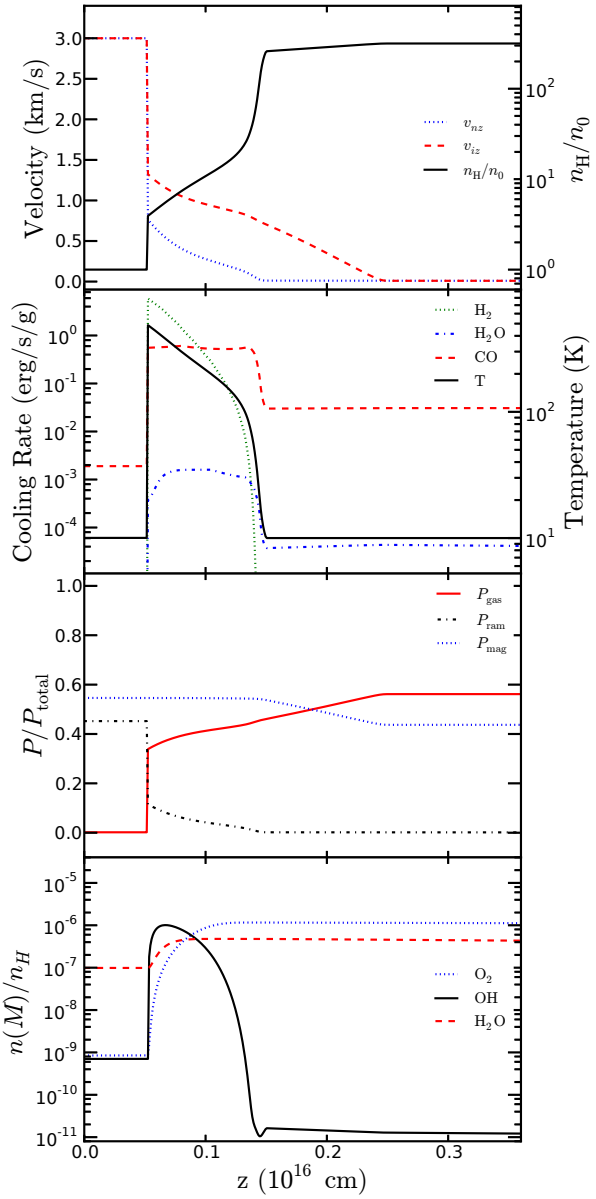

Figure 2.6: Same as Fig. 2.5 but for a $v_s = 3$ km s^{-1} slow shock propagating through a medium with initial number density $n_0 = 10^3$ cm^{-3} at 30° to an 80 μG magnetic field.

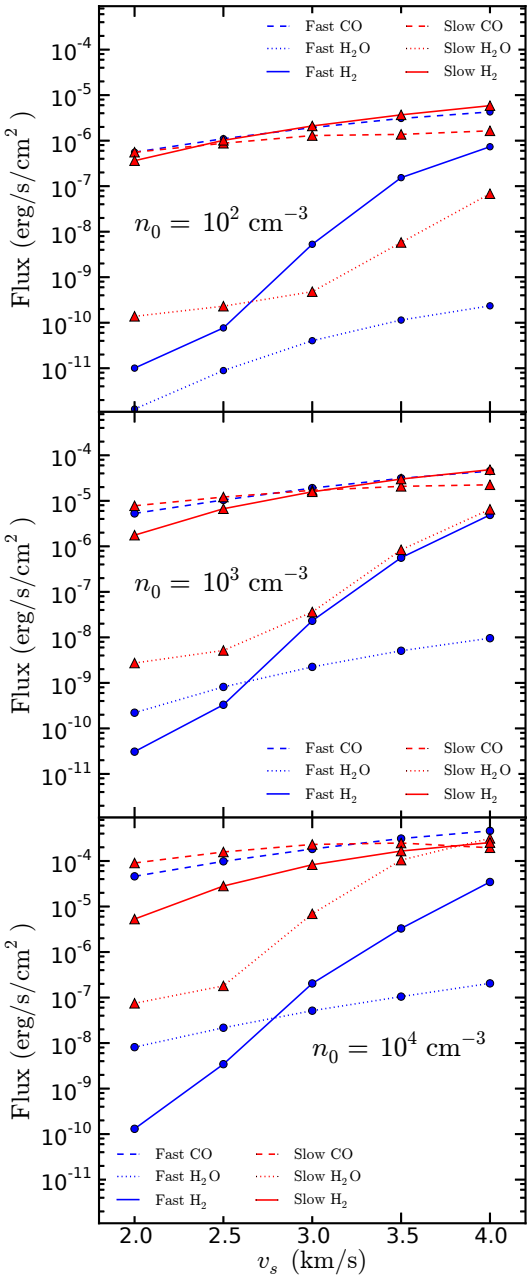

Figure 2.7: Energy flux contributions by different coolants in shocks of initial density $n_0 = 10^2$ cm^{-3} (top), $n_0 = 10^3$ cm^{-3} (middle) and $n_0 = 10^4$ cm^{-3} (bottom), and shock velocities $v_s = 2$–4 km s^{-1}. Blue circles refer to fast shocks and red triangles refer to slow shocks. Solid, dotted and dashed line types indicate whether the coolant is CO, H_2 or H_2O respectively.

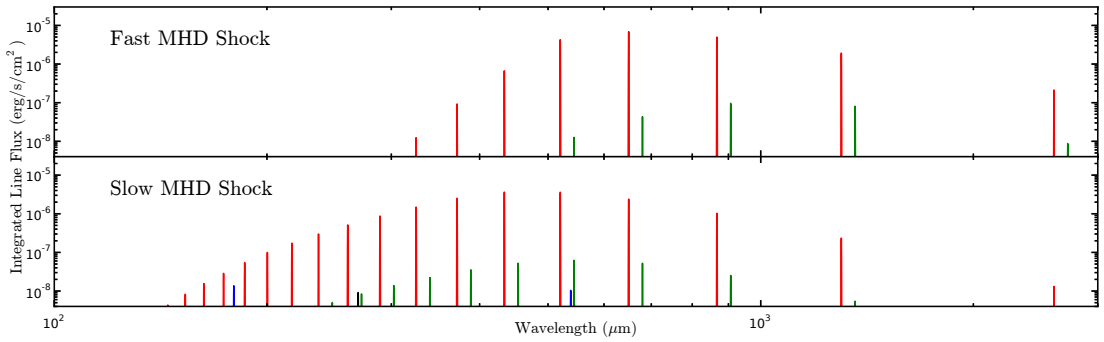

Figure 2.8: Estimates of integrated line fluxes from rotational lines of ^{12}CO (red), ^{13}CO (green), ortho-H_2O (blue) and para-H_2O (black) for the fast (top) and slow (bottom) shocks shown in Figs. 2.5 and 2.6.

shocks by 5 orders of magnitude at the lowest velocity and 1 order of magnitude at the highest. The H_2O flux is also stronger in the slow shock at all velocities.

Fig. 2.7 shows that for slow shocks the CO and H_2 fluxes are within an order of magnitude of each other at all velocities. For fast shocks, however, the CO flux is always stronger by more than an order of magnitude. This feature holds at initial densities $n_0 = 10^2$ and 10^4 cm^{-3}, though the magnitudes of the fluxes are lower and higher respectively by factors of 10 than the $n_0 = 10^3$ cm^{-3} case. This suggests that combining observations of flux from both molecules is a strong indicator of the kind of shock being observed.

Rotational lines

Fig. 2.7 shows similar levels of CO flux for both fast and slow shocks at all the velocities considered here. However, the strength of the individual rotational lines that make up this flux is not expected to be the same given the higher temperatures that slow shocks reach. Here we estimate those those line strengths using the non local thermodynamic equilibrium (LTE) radiative transfer code RADEX (van der Tak et al., 2007).

For a given radiating molecule, RADEX requires as input the density of H_2 as the collisional partner, the column density of the radiating molecule, the temperature and the linewidth. We consider 4 molecules with H_2 as the collisional partner: ^{12}CO, ^{13}CO, ortho-H_2O and para-H_2O. We use a ^{12}CO to ^{13}CO ratio of 61:1, well within the range of measurements given by Milam et al. (2005), and an ortho-to-para H_2O ratio of 3:1 as assumed in section 2.2.3 for the cooling function.

We use RADEX in slab mode, and use density weighted averages of the required inputs over appropriate slab definitions of the computed shocks. For slow shocks, we define multiple slabs in order to account for the complex temperature and density

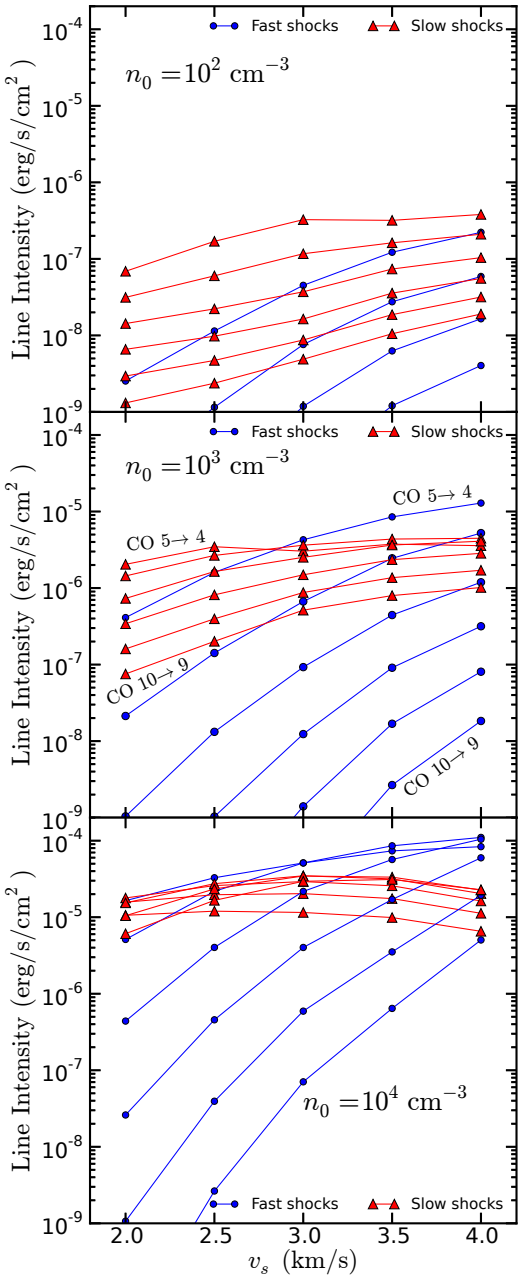

Figure 2.9: Integrated line intensities of CO rotational lines for fast (blue circles) and slow (red triangles) shocks with preshock densities $n_0 = 10^2\,\mathrm{cm}^{-3}$ (top), $n_0 = 10^3\,\mathrm{cm}^{-3}$ (middle) and $n_0 = 10^4\,\mathrm{cm}^{-3}$ (bottom), and shock velocities $v_s = 2 - 4$ km s^{-1}. The solid lines connect rotational lines of the same transition from $J = 5 \rightarrow 4$ to $J = 10 \rightarrow 9$.

structure. While RADEX accounts for optical depth effects within each slab and outputs the optical depth for each rotational transition, the emission from a slab may be reabsorbed by the other slabs it has to pass to reach the observer. Hence estimates of line strengths from lines of high optical depth—such as the CO lines below $J = 5 \rightarrow 4$—may not be reliable. Differences in the optical depth of particular lines in fast and slow shocks may have an observational effect. For example, Burkhart et al. (2013) show that the slope of the spatial power spectrum derived from synthetic observations of ^{13}CO $J = 2 \rightarrow 1$ in simulations of MHD turbulence is sensitive to the optical depth of this line. Furthermore, this slope could distinguish between sub- and super-Alfvènic turbulence. However, to relate the optical depth of a line emitting from dense postshock regions to that over a line of sight through a cloud requires knowledge of the spatial distribution of shock waves in the cloud, which is beyond the scope of this work. Finally, we normalise the line strengths so that emission from each molecule from all its lines is equal to the fluxes given in Fig. 2.7.

In Fig. 2.8 we plot the line strengths as computed by RADEX for the fast and slow shocks shown in Figs. 2.5 and 2.6. As expected, the higher temperature of the slow shock results in strong excitation of the high-J CO transitions of both isotopes. There are also excited H_2O lines in the slow shock that are negligible in the fast shock.

Any line of sight through a cloud will intersect multiple shocks propagating at different velocities, so we look for features in the spectra that hold across the velocity range. In Fig. 2.9 we plot the line integrated fluxes for selected high-J lines of CO across the velocity and density ranges for fast and slow shocks. In all slow shocks, the dynamic range of these high-J lines of CO is much lower than in fast shocks. For example, the line ratio CO $J = 5 \rightarrow 4/10 \rightarrow 9$ for a fast shock is always greater than 30 times the ratio from the slow shock of the same velocity and density.

As line ratios don't change if the line strengths are reduced by a constant factor, these distinguishing features will remain even though the shocks propagate in various directions with respect to the line of sight. Furthermore, any line of sight through a turbulent cloud will cross multiple shock fronts. Emission from optically thin lines will be a simple addition of emission from each shock, retaining line ratio characteristics which therefore could be strong indicators of shock type.

The high temperatures reached within slow shocks allow H_2 cooling to become comparable to cooling by CO, as can be seen in Fig. 2.7. The H_2 molecule has no dipole moment, and so this cooling is due to weak quadrupole emission. We can estimate the low lying pure rotational lines ($\nu = 0 \rightarrow 0$) of this emission using Figure 1 of Burton et al. (1992), which assumes the column of radiating H_2 is in LTE. For pure rotational lines S(0)-S(3), the line integrated fluxes emitted normal to the plane of the slow shock in Fig. 2.6 are in the range $\sim 10^{-7}$-10^{-6} erg/cm^2/s. These lines are strongly suppressed in gas below 100 K, and so the fast shock in

Fig. 2.5 produces negligible S(0)-S(3) line emission. This estimate shows that the pure rotational lines of H_2 could be an important diagnostic of shock type. However, the assumption of LTE doesn't always hold and so to produce a more accurate prediction for H_2 rovibrational line emission the level populations would have to be computed in parallel with the shock flow variables and reaction rate equations, as is done for instance in the fast shock model of Gusdorf et al. (2008).

2.5 Discussion

We have integrated the two-fluid MHD equations to obtain one dimensional time-independent fast and slow shock wave solutions. While two-fluid fast MHD shocks have been well studied (e.g. Draine, 1986; Flower and Pineau Des Forêts, 1998), two-fluid slow shocks have not been considered in molecular cloud conditions. Thus we use a simplified model in order to highlight the qualitative differences between the two kinds of shocks. Simplifications include restricting the chemical network to a small subset of reactions that influence the abundance of H_2O, as this is an important coolant in molecular gas. Gas-phase oxygen chemistry is adequately captured by the restricted network used here (Iglesias and Silk, 1978) and so a richer network—such as that used in Glover et al. (2010)—would not strongly affect H_2O production. We have not modeled how a variety of different initial abundances—which varies throughout a turbulent molecular cloud (Glover et al., 2010)—could affect the shock chemistry or cooling profiles. We have also not considered any grain surface chemistry. The formation of H_2 on the surface of dust grains dominates over gas phase reactions (Gould and Salpeter, 1963). In addition, collisions with shock-heated gas can lead to desorption of coolants into the gas-phase, altering the radiative structure of the shocks modeled here. In chapter 4, we extend the chemical model to account for these effects. However, improved chemistry will not change the differences in the magnetohydrodynamic structure between fast and slow shocks which is determined by whether the shock is driven by magnetic or gas pressure, respectively. Rotational line emission from H_2 could provide more observational diagnostics and has been computed in fast shock models by Lesaffre et al. (2013). In order to predict this emission accurately the level populations of the rovibrational states of H_2 have to be computed in parallel with the shock flow variables and reaction rate equations.

This work shows that fast and slow MHD shocks are structurally and observationally distinct. In section 2.2.1 we noted that fast shocks increase the angle between the magnetic field and direction of propagation whereas slow shocks decrease this angle. In principle this effect could be observed in studies of the polarized thermal emission revealing the geometry of magnetic fields in molecular clouds. The study by Planck Collaboration et al. (2016b) has shown that in high column density fila-

ments the magnetic field tends to be perpendicular to the filament. Padoan et al. (2001) explain these filaments as dense postshock regions resulting from the collision of supersonic turbulent flows. This result precludes the possibility that the filaments contain the fast shocks most commonly modeled (e.g. Flower and Pineau Des Forêts, 2010; Pon et al., 2012) in which the magnetic field is parallel to the shock front. Higher spatial resolution work of this kind could either detect the magnetic field bending across shock fronts or rule out the shock formation scenario of filaments. In section 2.4 we showed that observations of high-J CO lines—above $J = 6 \rightarrow 5$—could distinguish between fast and slow MHD shocks. Multiple transitions should simultaneously be observed to disentangle the possible shock models through the use of line ratios. In addition, velocity information from linewidths could be used to constrain the shock velocity of the model. Hence, useful observations would require spectral resolutions better than 1 km/s at the high-J CO lines (CO $J = 6 \rightarrow 5$ to $J = 10 \rightarrow 9$ lines lie in the frequency range 691.47–1151.99 GHz). In addition, the spatial resolution must be sufficient to avoid gas warmed by protostellar outflows or stellar winds. These criteria can be satisfied by the HIFI spectrometer (de Graauw et al., 2010) on the *Herschel Space Observatory* (Pilbratt et al., 2010), the *Attacama Large Millimetre Array* (ALMA) and the *GREAT* spectrometer (Heyminck et al., 2012) on the *Stratospheric Observatory for Infrared Astronomy* (Becklin and Gehrz, 2009). However, the frequency range for ALMA can only sample the mid-J CO transitions up to $J = 7 \rightarrow 6$ (ALMA Band 10) and so may not strongly distinguish fast and slow shock signatures. Additionaly, the frequency range of GREAT samples higher J transitions (CO $J = 11 \rightarrow 10$ to $J = 13 \rightarrow 12$), at which the emission may be too weak. By way of example, we consider a recent *Herschel* observation that satisfies these criteria and show that slow shock signatures may be present.

Pon et al. (2015) (hereafter P15) present observations of CO $J = 8 \rightarrow 7$, $9 \rightarrow 8$ and $10 \rightarrow 9$ taken with the *Herschel* Space Observatory, towards four starless clumps within Galactic infrared dark clouds (IRDCs). These clumps were chosen because they lacked massive embedded protostars, avoiding confusion from outflows which could also create a warm gas component. The authors detect CO $J = 8 \rightarrow 7$ and $9 \rightarrow 8$ towards three of their clumps—named C1, F1 and F2—and give an upper limit for the $10 \rightarrow 9$ line. They compare these observations to PDR models at densities of 10^4 and $10^5\,\mathrm{cm}^{-3}$, typical of IRDCs, and interstellar radiation fields of 1 and ~ 3 Habing. All of the PDR models underpredict the CO $J = 9 \rightarrow 8$ line, so the authors suggest that the dissipation of turbulence in low velocity shocks could account for these lines. Here we consider how fast and slow shocks similar to those modeled in this chapter could account for these observations.

To convert the integrated line intensity ($\int T dv$) of P15 to flux we use the formula

$$F = \frac{2k\Omega\nu^3}{c^3} \int T dv, \tag{2.5.1}$$

Table 2.4: CO high-J line luminosities for IRDCs (Pon et al., 2015) and selected shock models

Source	CO $J = 8 \rightarrow 7$ $\left(10^{-14}\,\mathrm{erg/s/cm^2}\right)$	$\frac{\mathrm{CO}J=9\rightarrow8}{\mathrm{CO}J=8\rightarrow7}$	$\frac{\mathrm{CO}J=10\rightarrow9}{\mathrm{CO}J=8\rightarrow7}$
C1	1.26 ± 0.06	0.65 ± 0.07	$< 2.10 \pm 0.24$
F1	1.48 ± 0.09	0.94 ± 0.10	$< 2.20 \pm 0.29$
F2	1.19 ± 0.09	0.77 ± 0.10	$< 2.69 \pm 0.36$
Slow Shock Models			
(A)	1.66	0.51	0.27
(B)	1.75	0.80	0.58
Fast Shock Models			
(A)	1.19	0.16	0.03
(B)	4.10	0.25	0.06

Notes. The values used for the $J = 10 \rightarrow 9$ line from IRDCs are the suggested upper limits. Slow shocks A and B have shock velocities $v_s = 2$ km s^{-1} and 3.5 km s^{-1} respectively. Fast shocks A and B have shock velocities $v_s = 3.5$ km s^{-1} and 4.0 km s^{-1} respectively. All four shock models have preshock density $n_0 = 10^4\,\mathrm{cm^{-3}}$.

where k is the Boltzmann constant, Ω is the beam area, ν is the frequency of the transition under consideration and c is the speed of light. The CO $J = 8 \rightarrow 7$, $9 \rightarrow 8$ and $10 \rightarrow 9$ transitions have rest frequencies of 921.80, 1036.91 and 1151.99 GHz and half power beam widths (HPBWs) of 23, 20 and 19 arcseconds respectively. We use

$$\Omega = \frac{\pi}{4 \ln 2} \left(\mathrm{HPBW}\right)^2 \tag{2.5.2}$$

to compute the beam area. Finally, we use the average of the detected line intensities for comparison (Column 8 of Table 3 in Pon15). For this set of values the line fluxes are shown in Table 2.4. The second column shows the CO $J = 8 \rightarrow 7$ line flux, while the third and fourth columns show the CO $J = 9 \rightarrow 8/8 \rightarrow 7$ and CO $J = 10 \rightarrow 9/8 \rightarrow 7$ line ratios respectively. The CO $J = 10 \rightarrow 9$ line was not detected in any of the clumps so we use the upper limits adopted in Pon15. This means that the CO $J = 10 \rightarrow 9/8 \rightarrow 7$ line ratio is an upper limit.

We also list in Table 2.4 the predicted values from selected slow and fast shocks by multiplying the RADEX intensities (Fig. 2.9) by $\Omega/4\pi$ for the appropriate beam areas. The predicted value of the CO $J = 8 \rightarrow 7$ integrated intensity assumes the shock front faces the observer and fills the beam. We chose the models that give the closest CO $J = 8 \rightarrow 7$ line fluxes (Slow and Fast shock A in Table 2.4) as well as the shocks that give the closest CO $J = 9 \rightarrow 8/8 \rightarrow 7$ line ratios (Slow and Fast shock B in Table 2.4).

Slow shocks A and B have shock velocities $v_s = 2$ km s^{-1} and 3.5 km s^{-1} respectively. Fast shocks A and B have shock velocities $v_s = 3.5$ km s^{-1} and 4.0 km s^{-1} respectively. All four shock models have preshock density $n_0 = 10^4\,\mathrm{cm}^{-3}$ which agrees well with typical densities of IRDCs. Fast shock A is the only shock that doesn't overpredict the observed integrated intensities, but the predicted integrated intensities of the other three models could be reduced to match the observations if the shock doesn't fill the beam. Hence the observed line flux of CO $J = 8 \rightarrow 7$ from these IRDCs can be explained by either fast or slow shocks.

The slow shocks generally fit the CO $J = 9 \rightarrow 8/8 \rightarrow 7$ line ratios better than the fast shocks, with the line ratio from slow shock B (0.80) very close to the average of the ratio for all three clumps (~ 0.78). The predicted line ratio from fast shock B (0.25) is the largest predicted from all the fast shocks modeled, which still underpredicts the observed values by $\sim 3 - 4$ times. Hence the high temperatures produced in slow shocks are necessary to explain both the CO $J = 8 \rightarrow 7$ and $9 \rightarrow 8$ emission from these clumps. Combined with the inability of PDR models to explain these observations, we therefore suggest that a slow shock interpretation is favoured by the models in this chapter.

2.6 Conclusions

The one dimensional time independent two-fluid MHD equations were numerically integrated to compare the structure of low-velocity fast and slow shocks in molecular clouds. Our simplified model includes the effects of the major coolants found in molecular clouds and follows the abundances of chemicals affecting the production of H_2O in a simple chemical network. The solutions highlight important differences between fast and slow MHD shocks in molecular clouds. These shocks show strong differences in their velocity and density structure because of the different driving pressures behind the shock fronts. Fast shocks are driven by magnetic pressure while slow shocks are driven by gas pressure. This means that the thickness of fast shocks is set by the long ion-neutral collision timescale, wheareas the thickness of slow shocks is set by the short neutral-ion collision timescale. The cooling timescale of the gas lies between these two and so peak temperatures in slow shocks are far higher than fast shocks of the same shock speed.

We showed that fast and slow shocks are observationally distinct and provided some example diagnostics. For instance, low lying pure rotational lines of H_2 contribute negligibly to the cooling in fast shocks, whereas they produce significant radiation from the warm gas in slow shocks. The non-LTE radiative transfer code RADEX was used to estimate line strengths of rotational transitions of ^{12}CO, ^{13}CO, ortho-H_2O and para-H_2O. The higher temperatures of slow shocks excite the high-J transitions of ^{12}CO more than in fast shocks. Line ratios near these transitions

show strong differences between fast and slow shocks across the velocity range and therefore may be strong indicators of shock type. Anomalously strong high-J CO lines have been observed in nearby infrared dark clouds (Pon et al., 2015). The line ratios from these observations closely match slow shock predictions and are poorly fit by any of the fast shocks modeled here.

This suggests that simulations of MHD turbulence could gain observational predictions if the statistics of shock types were recorded. If the mixture of shock families is found to be sensitive to turbulence parameters—such as the driving mode, the kind of feedback included, Mach number variations and self-gravity—then shock signatures become observational probes of the turbulence. Combined with tracers of star formation like young stellar objects, shock signatures could then shed light on the influence of supersonic MHD turbulence on star formation.

Chapter 3

Shocks in magnetohydrodynamic simulations

Abstract

The formation of stars occurs in the dense molecular cloud phase of the interstellar medium. State of the art simulations of this phase have shown that the character of star formation depends on the details of the supersonic magnetohydrodynamic (MHD) turbulent dynamics of these clouds. Simulations have also shown that a large fraction of the turbulent energy dissipates in shock waves. The three families of MHD shocks — fast, intermediate and slow — distinctly compress and heat up the molecular gas, and so provide an important probe of the physical conditions within a turbulent cloud. We describe a publicly available algorithm, SHOCKFIND, to extract and characterise the mixture of shock families in simulations of MHD turbulence. The algorithm is applied to a 3-dimensional simulation of a magnetised turbulent molecular cloud, and we find that both fast and slow MHD shocks are present in the simulation. We give the first prediction of the mixture of turbulence-driven MHD shock families in a molecular cloud, and present their distinct distributions of sonic and Alfvénic Mach numbers. Using subgrid one-dimensional models of MHD shocks we estimate that ~ 0.03 % of the volume of a typical molecular cloud in the Milky Way will be shock heated above 50 K, at any time during the lifetime of the cloud. We discuss the impact of this shock heating on the dynamical evolution of molecular clouds.

3.1 Introduction

The formation of stars is sensitive to the underlying physics of the supersonic magnetohydrodynamic (MHD) turbulence in molecular clouds (Mac Low and Klessen, 2004; Elmegreen and Scalo, 2004; Krumholz and McKee, 2005; McKee and Ostriker, 2007; Hennebelle and Chabrier, 2008; Padoan and Nordlund, 2011; Hennebelle and Falgarone, 2012). High resolution three-dimensional simulations of molecular clouds have shown that the star formation rate and efficiency depend on whether the turbulence is solenoidally or compressively driven (Federrath and Klessen, 2012, 2013), and that the stellar initial mass function is sensitive both to non-ideal MHD effects such as ambipolar diffusion (McKee et al., 2010) and to the driving and Mach number of the turbulence (Hennebelle and Chabrier, 2009, 2013; Hopkins, 2013). The importance of stellar feedback (Krumholz et al., 2007; Cunningham et al., 2011; Myers et al., 2014; Nakamura and Li, 2007; Wang et al., 2010; Price and Bate, 2008, 2009; Offner and Arce, 2014; Federrath et al., 2014; Federrath, 2015; Padoan et al., 2016), whether gravity drives turbulent motions (Elmegreen and Burkert, 2010; Klessen and Hennebelle, 2010; Vázquez-Semadeni et al., 2010; Federrath et al., 2011; Robertson and Goldreich, 2012) and the role that turbulence plays in producing the ubiquitously observed filaments (Arzoumanian et al., 2011; André et al., 2014; Smith et al., 2014, 2016; Federrath, 2016; Kainulainen et al., 2016; Hacar et al., 2016) are big questions that continue to be studied. Rigorous observational effects distinctly revealing the presence or dominance of the various physical processes are strongly sought after.

Observed non-thermal linewidths of molecular lines reveal turbulence in molecular clouds is highly supersonic, with Mach numbers typically in the range of 3 to 30 (Larson, 1981; Solomon et al., 1987; Ossenkopf and Mac Low, 2002; Heyer and Brunt, 2004; Roman-Duval et al., 2011; Schneider et al., 2013; Henshaw et al., 2016). The supersonic flows in these clouds will inevitably form shock waves. MHD simulations by Stone et al. (1998) found that $\sim 50\%$ of the turbulent energy is dissipated by shocks. When turbulence is allowed to decay, a large range of weak shocks is responsible for the majority of the dissipation (Smith et al., 2000b), whereas a small range of stronger shocks dissipates the turbulence while it is continuously driven (Smith et al., 2000a). If other turbulence parameters — such as magnetic field strength, driving mechanism, Mach number, inclusion of other physical effects like self-gravity, stellar feedback, cosmic rays and others — could be linked to distributions of shock waves, then the radiative signatures of shocks become observational diagnostics for these parameters in molecular clouds. The goal of this work is to determine this link, from turbulence parameters to distributions of shock waves, in *simulations* of turbulent clouds in order to provide observational tests of the various physical processes.

MHD fluids can support three families of shocks: fast, intermediate and slow (de Hoffmann and Teller, 1950; Kennel et al., 1989). Note that these names refer to the associated MHD linear wave modes, and not to the speed of a given shock. In section 3.2 we use the MHD jump conditions to detail the fundamental differences between the shock families. Pon et al. (2012) argue that, for molecular clouds, the turbulent cascade leads to low-velocity shocks (a few km/s) doing the majority of the dissipation. They show that even at low velocities, fast MHD shocks will radiate more strongly than photodissociation regions in mid-J rotational transitions of CO. Chapter 2 uses two-fluid MHD models of shocks in molecular cloud conditions to show that low-velocity fast and slow MHD shocks distinctly compress and heat the molecular gas. At velocities less than 4 km/s slow shocks can reach compression ratios of up to 500 whereas fast shocks compress the gas less than 10 times the preshock values. In addition, slow shocks can reach peak temperatures up to ~ 800 K whereas fast shocks reach up to ~ 150 K. This is because in a weakly ionized gas — such as in molecular clouds — the ion-neutral collision timescale, which determines the heating timescale in fast shocks, is slower than the cooling timescale, which in turn is slower than the neutral-ion collision timescale that controls the heating in slow shocks. These higher peak temperatures in slow shocks result in stronger CO rotational lines (above $J = 6-5$) and low-lying pure rotational lines of H_2 ($\nu = 0-0$) than in fast shocks of the same velocity.

Molecular clouds are usually assumed to be in chemical equilibrium for the average conditions of the cloud. However, the inhomogeneous structure introduced by turbulence allows for local reaction rates to significantly differ from global average conditions (Hollenbach et al., 1971; Wolfire et al., 1995; Glover et al., 2010). Shocks are an important local mechanism for driving chemical reactions. Kumar and Fisher (2013) followed the chemical evolution of a parcel of gas through a turbulence simulation and found the abundances of molecules, like CH_2 and HCO, to be highly sensitive to shocked regions. Their work considers only hydrodynamic shocks and so cannot capture the qualitatively distinct behaviours of differing MHD shock families. For example, the higher temperatures of low-velocity slow shocks produce vastly different chemical abundances than fast shocks of the same velocities (Chapter 2). Using a simple oxygen chemical network Chapter 2 shows that while fast shocks leave preshock abundances mostly untouched, slow shocks can increase the abundances of molecules like OH, O_2 and H_2O by several orders of magnitude within the hot shock front. To understand the chemical makeup of turbulent molecular clouds it is therefore important to understand which families of MHD shocks are present and how much volume they affect.

While there is some observational evidence for the dissipation of molecular cloud turbulence in fast MHD shocks (Lesaffre et al., 2013; Pon et al., 2014, 2016a; Larson et al., 2015) and in slow MHD shocks (Chapter 2), thus far no one has determined

which kinds of MHD shocks are present in simulations of magnetised turbulent molecular clouds. In section 3.3 we present an algorithm, SHOCKFIND, to detect and characterise the mixture of MHD shock types in such simulations. We apply our new algorithm to an MHD simulation of molecular cloud turbulence in section 3.4. Finally, we discuss these results and conclude our study in sections 3.5 and 3.6 respectively. The SHOCKFIND algorithm, written in PYTHON, is publicly available and can be found on BitBucket (https://bitbucket.org/shockfind/shockfind) and the PYTHON Package Index (https://pypi.python.org/pypi/shockfind). It is released under the Apache license version 2.0, and comes with documentation including a user's guide.

3.2 Magnetohydrodynamic Shocks

Section 2.2.1 contains a detailed discussion of some of the fundamental differences between the shock families in the ideal limit of MHD. Here we summarise the relevant theoretical implications of the MHD jump conditions, and illustrate how the various families of MHD shocks characteristically affect the ambient magnetic field. We modify the discussion in Section 2.2.1 to emphasise the shock properties that our algorithm exploits.

In the frame of reference comoving with a shock wave — the shock frame — the pre-shock fluid has a speed, v_s, greater than a linear wave speed in the fluid. The fluid then transitions inside a discontinuity to a fluid velocity less than a wave speed in the post shock fluid. In ideal MHD, the three linear waves supported, the fast, intermediate and slow waves have phase velocities

$$f = \left(\frac{v_\mathrm{A}^2 + c_\mathrm{s}^2}{2} + \frac{1}{2}\sqrt{\left(v_\mathrm{A}^2 + c_\mathrm{s}^2\right)^2 - 4 v_\mathrm{A}^2 c_\mathrm{s}^2 \cos^2\theta} \right)^{1/2}, \tag{3.2.1}$$

$$i = v_\mathrm{A} \cos\theta, \tag{3.2.2}$$

$$s = \left(\frac{v_\mathrm{A}^2 + c_\mathrm{s}^2}{2} - \frac{1}{2}\sqrt{\left(v_\mathrm{A}^2 + c_\mathrm{s}^2\right)^2 - 4 v_\mathrm{A}^2 c_\mathrm{s}^2 \cos^2\theta} \right)^{1/2}, \tag{3.2.3}$$

where $v_\mathrm{A} = B/\sqrt{4\pi\rho}$ is the Alfvén velocity, $c_s = \sqrt{k_\mathrm{B} T/\mu_\mathrm{m}}$ is the isothermal sound speed with Boltzmann constant k_B and mean mass per particle μ_m, and θ is the angle between the magnetic field and the direction of propagation of the wave. These speeds are plotted as functions of θ in Fig. 2.1 for $v_\mathrm{A} > c_\mathrm{s}$, as is usually the case in molecular clouds.

The three wave speeds demarcate four regions of fluid velocities marked 1 to 4 in Fig. 2.1. There are six ways to transition across at least one wave speed within the shock front, resulting in three families of MHD shocks: fast, intermediate and slow shocks. Fast shocks cross the fast wave speed only (1–2), intermediate shocks

cross the intermediate wave speed (1–3, 1–4, 2–3, and 2–4), and slow shocks cross the slow wave speed only (3–4). This means that for a fast shock the Alfvénic Mach number — defined by $\mathcal{M}_{\rm A} \equiv v_{\rm s}/v_{\rm A}$ — is necessarily greater than unity, whereas for a slow shock the shock speed is sub-Alfvénic, i.e., $M_A < 1$. We will use this criterion to distinguish fast from slow shocks in the next section.

For a time-independent, plane-parallel shock wave, the pre- and post-shock mass density, velocity, gas pressure and magnetic field are related by the Rankine-Hugoniot jump conditions (Kennel et al., 1989). A consequence of these jump conditions are changes in magnetic field geometry across a shock front characteristic of each shock family. In fast shocks, the component of the magnetic field perpendicular to the direction of propagation, $B_\perp$, must increase from the pre-shock to the post-shock value. In intermediate shocks, $B_\perp$ must switch sign. This switch is due to a rotation of the magnetic field within the shock front. Finally, in slow shocks $B_\perp$ must decrease. For all shocks, the planar symmetry implies that the magnetic field parallel to the direction of propagation is conserved across the shock front. These three characteristic changes of the magnetic field direction are shown schematically in Fig. 2.2.

The magnetic field strength is proportional to the separation of field lines, so one can see from Fig. 2.2 that the field strength increases across fast shocks and decreases across slow shocks. We will use this fact as a signature of these two classes of shocks in section 3.3. This also means that some of the kinetic energy of a fast shock is converted into magnetic field energy. Hence, for slow shocks at the same velocity as fast shocks, a greater portion of the energy budget is available to heat the gas. Finally, the magnetic field strength in intermediate shocks can either increase or decrease across the shock front depending on the initial conditions of a particular shock. Hence there is no simple signature of intermediate shocks in the magnetic field strength. In addition, there has been debate over whether intermediate shocks are physically admissable (e.g., Wu, 1987; Falle and Komissarov, 2001), and so this class of MHD shocks is ignored from this point on.

The structure of the magnetic field across the different shock waves only depends on the ideal MHD jump conditions. The heating inside the shock front, however, can depend on non-ideal effects. For example, in molecular clouds the gas is weakly ionized and so ion and neutral species can be decoupled. In this case, a multi-fluid approach is necessary to model the structure of the shock front. In fast shocks, the strong magnetic pressure behind the shock front drives ion species ahead of the neutrals in a magnetic precursor (Mullan, 1971; Draine, 1980). Collisional heating in fast shocks is thus controlled by the ion-neutral collision timescale, which is generally larger than the cooling timescale for low-velocity shocks (a few km/s) in molecular clouds. If the cooling keeps the temperature low within the shock, the neutral velocity may remain supersonic throughout and the fluid variables will smoothly

transition from pre-shock to post-shock values in what is called a C-type shock. In fast shocks with shock velocity exceeding the magnetosonic speed of the charged fluid, defined by

$$v_m = \sqrt{c_{\rm s}^2 + v_{A,c}^2}, \tag{3.2.4}$$

where $v_{A,c}$ is the Alfvén velocity in the charged fluid, a thin jump will form in which the heating is determined by molecular viscosity. Such a fast shock is called J-type. We see then, that we need to determine the local pre-shock conditions in turbulent molecular clouds in order to predict the shock heating from fast MHD shocks.

In the two-fluid models of Chapter 2 slow shocks produce a temperature structure distinct from fast shocks. Shocks of this family are driven by the gas pressure of the neutrals, and so heating is determined by the neutral-ion collision timescale. This timescale is shorter than the cooling timecale and so high peak temperatures are reached in a thin shock front resembling an ordinary hydrodynamic shock. The jump in temperature across this shock front is determined by the sonic Mach number $\mathcal{M} \equiv v_{\rm s}/c_{\rm s}$:

$$\frac{T_2}{T_1} = \left(1 + \frac{2\gamma}{\gamma+1}\left(\mathcal{M}^2 - 1\right)\right)\frac{\mathcal{M}^2\left(\gamma-1\right)+2}{\mathcal{M}^2\left(\gamma+1\right)}, \tag{3.2.5}$$

which reaches 200 K at low shock velocities ($v_{\rm s}$ $\sim$2 km/s for $c_{\rm s}$ = 0.2 km/s) and adiabatic index $\gamma = 5/3$. This is hot enough to produce chemical abundances and molecular cooling significantly different to ambient molecular cloud conditions.

Fast and slow shocks therefore present distinct temperature structures within molecular clouds. To fully understand the heating and chemistry driven by turbulent dissipation in shock waves it is therefore critical to determine the relative fraction of shock families. We will do this in the following by using numerical MHD simulations of turbulent molecular clouds.

3.3 Shock Detection Algorithm

In this section, we present a new algorithm, SHOCKFIND, to detect and characterise the shocks in MHD simulations of molecular clouds. We then test this algorithm by considering a case study simulation of colliding MHD shocks, which should be a common occurence in supersonic MHD turbulence.

3.3.1 Algorithm Summary

Here we summarise the seven-step algorithm, SHOCKFIND, for detecting fast or slow shocks in an MHD simulation. For a simulation with mass density ρ, three velocity

components u_x, u_y, and u_z, and three magnetic field components B_x, B_y, and B_z, the algorithm will:

1. Identify shock candidates as computational cells with large convergence:

$$-\nabla \cdot \mathbf{u} = -\left(\partial_x u_x + \partial_y u_y + \partial_z u_z\right), \tag{3.3.1}$$

   or large magnitude of the density gradient:

$$|\nabla \rho| = \sqrt{\left(\partial_x \rho\right)^2 + \left(\partial_y \rho\right)^2 + \left(\partial_z \rho\right)^2}, \tag{3.3.2}$$

   where large is above a user-defined threshold appropriate to the particular simulation. In section 3.4.1 we normalise these quantities for a turbulent cloud simulation using particular combinations of the velocity dispersion, average density and computational cell size. The normalised convergence and gradient are then related to shock properties, so that the search thresholds can be thought of as determining a minimum shock velocity or compression ratio;

2. Compute the shock direction at the location of each candidate cell, $\mathbf{n}_\mathrm{s}$, using the gradient of the density:

$$\mathbf{n}_\mathrm{s} = \nabla\rho / \left|\nabla\rho\right| = \left(\partial_x\rho,\, \partial_y\rho,\, \partial_z\rho\right) / \left|\nabla\rho\right|; \tag{3.3.3}$$

3. Extract averaged fluid variables along a cylinder perpendicular to the shock front. The cells, at coordinates $\mathbf{r}$, on the central axis of the cylinder are defined by

$$\mathbf{r} = \mathbf{r}_\mathrm{s} + \lambda \mathbf{n}_\mathrm{s}, \tag{3.3.4}$$

   where $\mathbf{r}_\mathrm{s}$ is the location of the candidate cell and λ parametrises the line and ranges from $\pm$ a few shock thicknesses, N, that the simulation spreads the shock over. The effect of varying the radius of this cylinder is shown in appendix A.1;

4. The cell-averaged variables for $\lambda > N/2$ are the pre-shock values, while the cell-averaged variables for $\lambda < -N/2$ represent the post-shock values;

5. Compute the shock speed using the pre- and post-shock parallel velocities and densities obtained in step (iv):

$$v_\mathrm{s} = \left(u_{\parallel,\mathrm{pre}} - u_{\parallel,\mathrm{post}}\right) / \left(1 - \rho_\mathrm{pre}/\rho_\mathrm{post}\right), \tag{3.3.5}$$

   where $u_\parallel = \mathbf{u} \cdot \mathbf{n}_\mathrm{s}$;

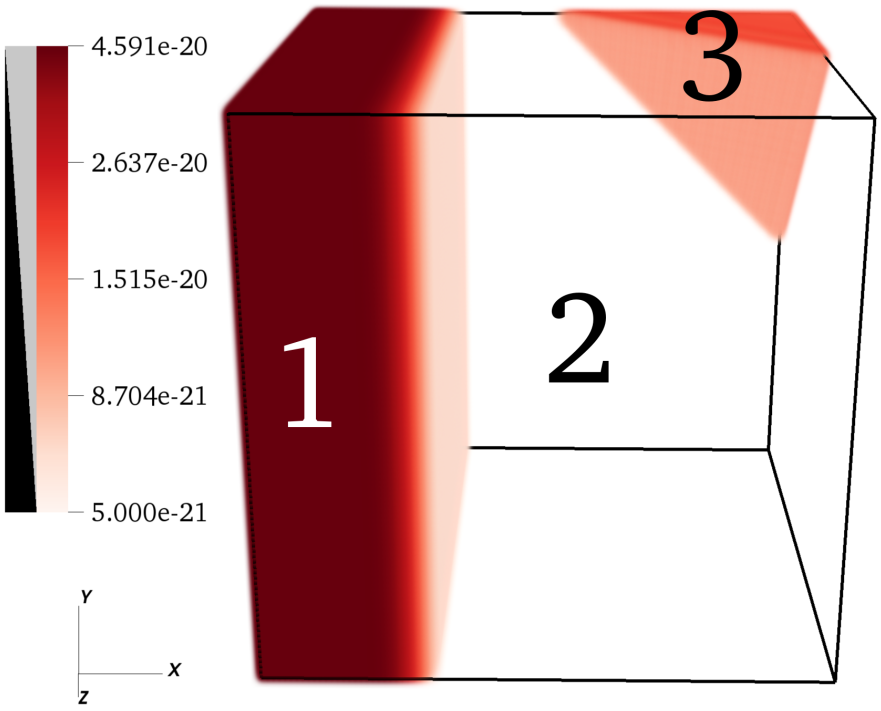

Figure 3.1: Initial density configuration of the colliding shock simulation. The regions labeled are (1) the slow post-shock region, (2) the common pre-shock region and (3) the fast post-shock region.

6. Compare the shock speed v_s to the pre-shock Alfvén velocity to form the Alfvénic Mach number $\mathcal{M}_A$. Fast shocks must have $\mathcal{M}_A > 1$ and slow shocks must have $\mathcal{M}_A < 1$. In addition, we compare the pre- and post-shock magnetic field strengths. Fast shocks must have $B_{post}/B_{pre} > 1$ and slow shocks must have $B_{post}/B_{pre} < 1$. If a shock candidate consistently satisfies both of these inequalities then we have detected a fast or slow MHD shock, otherwise it is only a candidate and is not included in the further analysis;

7. Finally, we filter the detected shock cells by ignoring those detections that do not occur at local maxima in the convergence along the extracted line of step (iii). This step avoids extracting multiple cells as individual shocks that actually belong to the same shock. This process is illustrated in appendix A.2.

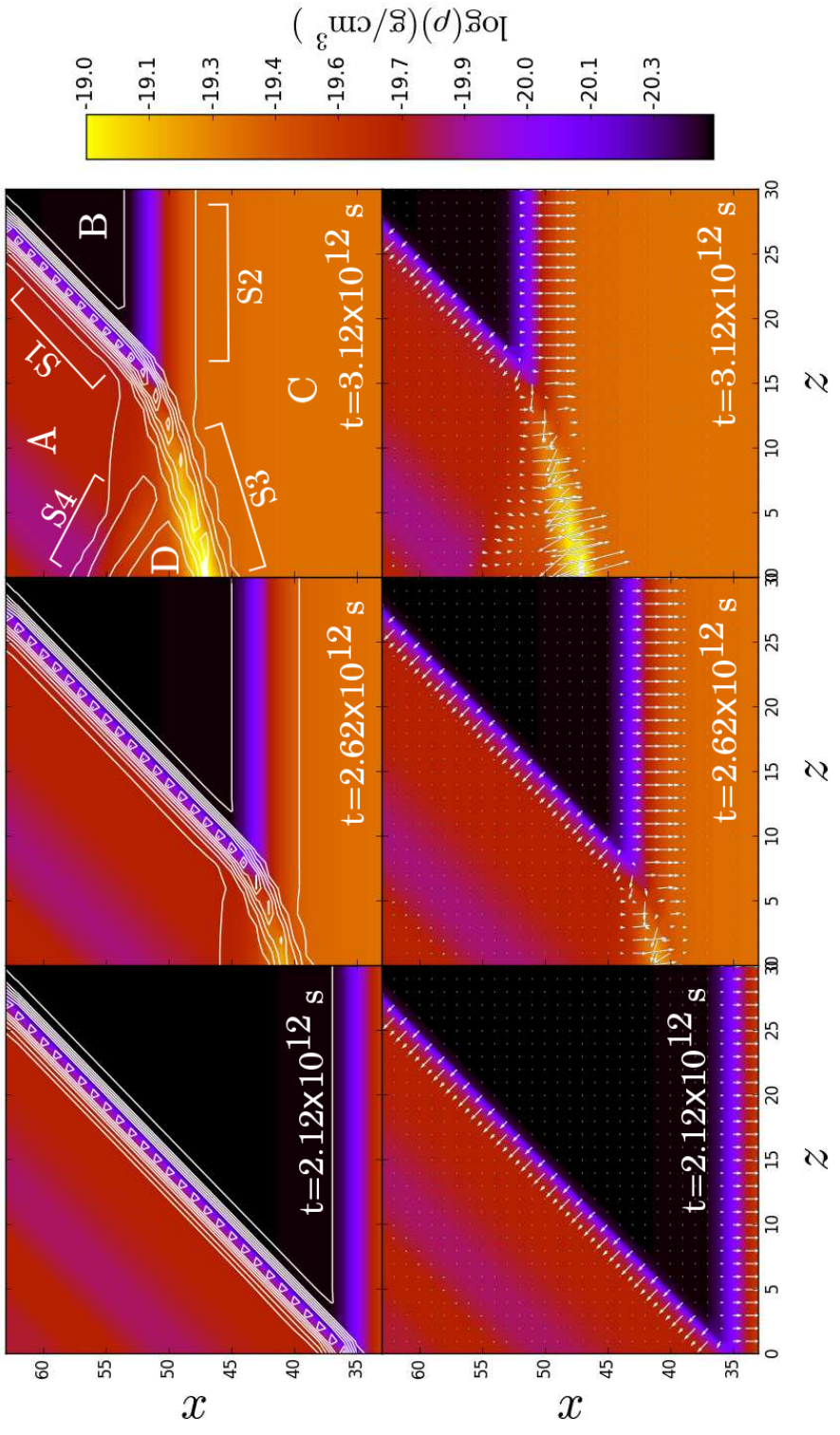

Figure 3.2: Three snapshots (left to right) of mass density slices (constant y) from the colliding MHD shocks simulation at times $t = 2.12 \times 10^{12}$, 2.62×10^{12} and 3.12×10^{12} s. The colours show mass density. In the upper row, the white contours are convergence ($-\nabla \cdot \mathbf{v}$) in this plane. In the lower row, vectors are projected gradient of density ($\nabla\rho$). The labels A–D denote different density regions and S1–S4 are shock candidates detailed in the text.

Table 3.1: Initial setup of colliding MHD shock simulation

Variable	Slow Post-shock (1)	Common Pre-shock (2)	Fast Post-shock (3)
$\rho\,(10^{-20}\,\mathrm{g/cm^3})$	4.591	0.385	1.800
$p\,(10^{-11}\,\mathrm{g\,cm/s^2})$	5.995	0.154	11.48
$u_x\,(\mathrm{km/s})$	3.803	2.887	1.141
$u_y\,(\mathrm{km/s})$	3.868	2.887	1.141
$u_z\,(\mathrm{km/s})$	−2.887	−2.887	0.430
$B_x\,(\mu\mathrm{G})$	24.75	24.75	69.07
$B_y\,(\mu\mathrm{G})$	5.569	24.75	69.07
$B_z\,(\mu\mathrm{G})$	0	0	88.64

3.3.2 Test simulation of colliding MHD shocks

In this section we illustrate the steps of our shock detection algorithm outlined in section 3.3.1, by applying it to a simulation of colliding shock waves. We use the code FLASH (Fryxell et al., 2000; Dubey et al., 2008) in version 4 to integrate the ideal, three-dimensional MHD equations. The equations are solved on a grid with a total of 128^3 grid cells using the HLL3R positive-definite Riemann solver (Waagan et al., 2011). The equations are closed with an ideal gas equation of state with adiabatic index $\gamma = 1.1$.

In this simulation we initialise a box with a slow MHD shock with shock speed $v_\mathrm{s} = 1$ km/s travelling in the direction $n_\mathrm{s} = (1, 0, 0)$, and a fast MHD shock with shock speed $v_\mathrm{s} = 5$ km/s travelling in the direction $n_\mathrm{f} = (-1, -1, 1)$. We choose pre-shock variables (common to both shocks) of density $\rho = 3.85 \times 10^{-21}\,\mathrm{g/cm^3}$, pressure $p = 1.54 \times 10^{-12}\,\mathrm{g\,cm/s^2}$, and a magnetic field strength of 35 μG oriented at 45° to the slow shock front. These pre-shock values are used to compute post-shock values using the MHD jump conditions (Kennel et al., 1989), and we choose a frame of reference such that the fast shock is stationary. Fig. 3.1 shows the initial density configuration of the three regions — slow post-shock, common pre-shock, and fast post-shock — and the fluid variables are listed in Table 3.1.

Convergence and density gradient

In Fig. 3.2 we plot slices of mass density of the colliding shock simulation at three different times ($t = 2.12 \times 10^{12}$, 2.62×10^{12} and 3.12×10^{12} s) in the simulation. The rightmost column shows a slice after the two shocks have collided and a significant interaction region has developed. The coloured contours show the density with 4 regions marked A–D. Region A is the post-shock region of the initial 5 km/s fast shock, region B is the common pre-shock region, region C is the post-shock region of the initial 1 km/s slow shock, and finally region D is the post-interaction region.

Overplotting the density contours in the upper row of Fig. 3.2 are white line contours of strong convergence, defined by equation (3.3.1). This quantity distinctly picks out candidate shock fronts labelled S1-S4. S1 and S2 are the initial fast and slow shocks we set up to collide. S3 and S4 are the results of the collision, which have geometries suggestive of a refractive (S3) and reflective (S4) process.

In the lower row of Fig. 3.2 we plot projected vectors of the gradient of the density over the contours of density. This vector points in the direction of increasing density and so it always points towards the plane of a shock front. This allows us to define a line through a shock at which we extract the fluid variables. It also allows us to compute the fluid velocity in the direction of shock propagation, $u_{\parallel}$, by projecting onto the direction given by the gradient.

Shock family criteria

Using the convergence and gradient as described above, we plot in Fig. 3.3 extracted fluid variables through the shock candidates S1-S4 from Fig. 3.2. The x-axis is zeroed at the convergence peak, with the post-shock region at negative values of x and pre-shock region at positive values of x. The convergence and gradient are normalised to their peak values. To compare pre- and post-shock fluid variables we take the average of the variable over a few cells either side of the convergence peak.

The S1 and S2 shocks (which were the initial fast and slow shocks, respectively) show strong density contrasts though the simulation has spread out the S2 shock (red lines in Fig. 3.3) over a wider range than the S1 shock. This is also reflected in a much lower and wider convergence peak in the slow shock. As discussed in section 3.2 the magnetic field, the lower panel of Fig. 3.3, in the S1 shock is stronger in its post-shock region compared to its pre-shock region because it is a fast MHD shock. Conversely, in the S2 shock B is stronger in the pre-shock region because it is a slow MHD shock.

Once we have computed pre- and post-shock densities, ρ_1 and ρ_2, respectively, and the pre- and post-shock parallel velocities, u_1 and u_2, respectively, we can determine the shock velocity $v_{\rm s}$ using equation (3.3.5). By comparing the shock speed to the Alfvén velocity we form the Alfvénic Mach number $\mathcal{M}_{\rm A}$. As discussed in section 3.2, for fast shocks $\mathcal{M}_{\rm A} > 1$ and for slow shocks $\mathcal{M}_{\rm A} < 1$. For the S1 and S2 candidates, we find that $\mathcal{M}_{\rm A} \sim 3.1$ and ~ 0.6 respectively, confirming their status as fast and slow MHD shocks.

The S3 and S4 shock candidates both have magnetic field stronger in the post-shock region than in the pre-shock region, indicating that they are fast MHD shocks. Indeed, for S3 the Alfvénic Mach number $\mathcal{M}_{\rm A} \sim 16.5$ and so it satisfies both criteria. However, for the S4 candidate $\mathcal{M}_{\rm A} \sim 0.8$, ruling it out as a fast shock. As it is a planar converging structure it could be a fast linear wave or even an intermediate shock, but our simple criteria cannot distinguish these cases. We will call converging

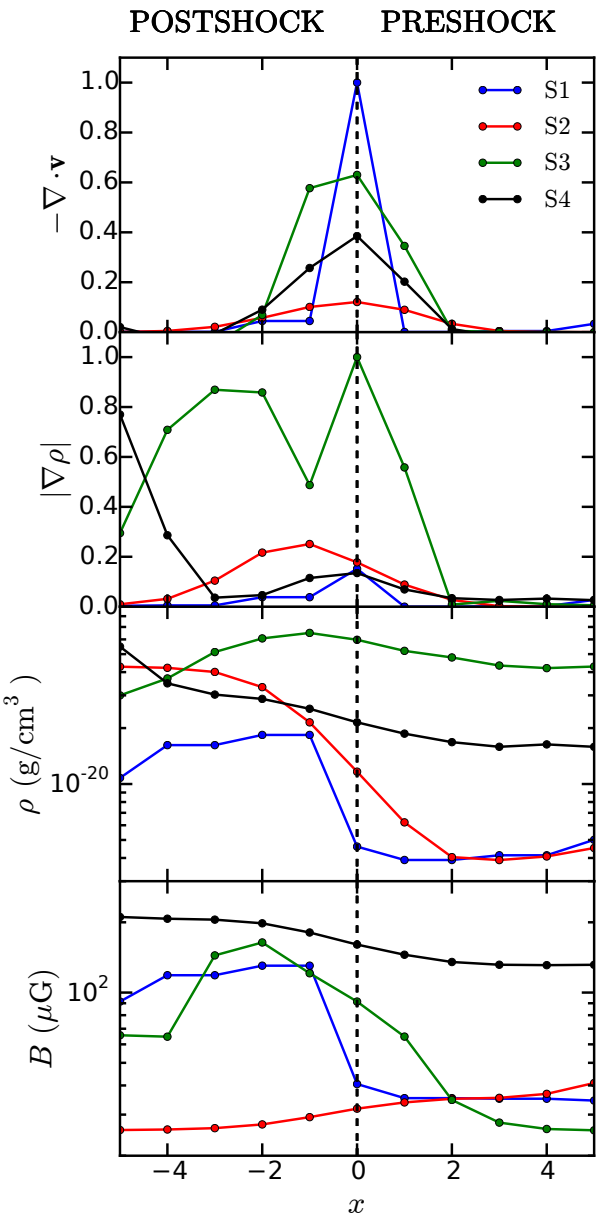

Figure 3.3: Line profiles through the shock candidates S1–S4 from Fig. 3.2. The profiles are of convergence ($-\nabla \cdot \mathbf{v}$), magnitude of the gradient of the mass density, mass density, and magnetic field strength. The convergence and gradient are normalised to their peak values. The x axis is in units of grid cell lengths.

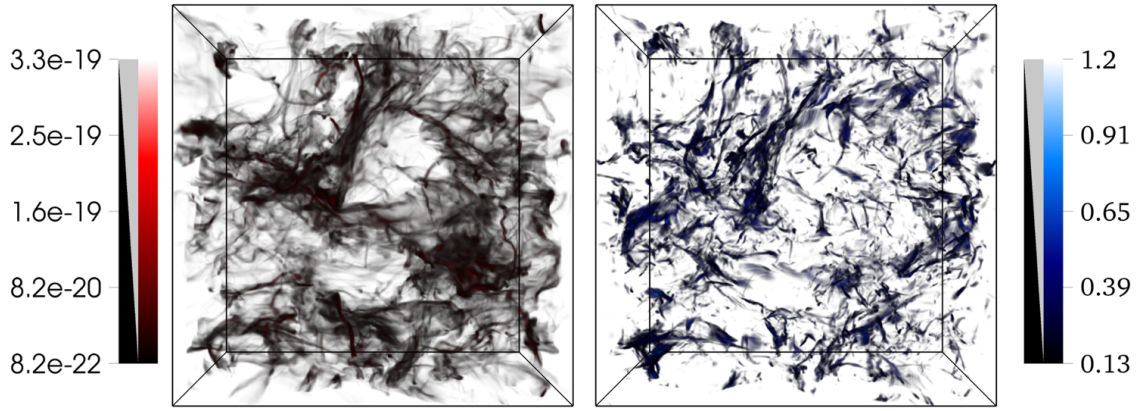

Figure 3.4: 3D renderings of the MHD simulation of turbulence. (Left) mass density above the average mass density $\langle\rho\rangle = 8.2 \times 10^{-22}$ g/cm^3. (Right) Convergence $(-\nabla \cdot \mathbf{v})$ normalised by the ratio of the velocity dispersion to the cell size.

structures that show magnetic field ratios inconsistent with Alfvénic Mach number criteria *fast-like* and *slow-like* disturbances and exclude them from further analyses.

3.4 Molecular Cloud Turbulence

Here we present an application of our shock-detection algorithm to a 3D simulation of molecular cloud turbulence. The ultimate goal is to determine the fraction of slow and fast shocks and their respective effects for the heating and evolution of molecular clouds.

We use the turbulent initial conditions of molecular cloud simulation model 21 (GT256mM10B10) from Federrath and Klessen (2012). It is a 3D simulation of an isothermal, ideal MHD, turbulent molecular cloud with mixed compressive and solenoidal driving. The turbulence is driven to maintain a velocity dispersion $\sigma \sim 1.8$ km/s. As the sound speed $c_s = 0.2$, the turbulence contains a large fraction of supersonic gas and is therefore expected to drive shocks with Mach numbers $\mathcal{M} \sim 9$. The magnetic field was initially uniform with strength 10 μG, and the time step that we analyse here occurs after two turbulent crossing times, when the turbulence has been fully developed and the dynamo is mostly saturated but before self-gravity has been turned on to study star formation. The details of the integration scheme can be found in that paper.

Fig. 3.4 shows three-dimensional renderings of the mass density (ρ, left panel) and convergence ($-\nabla \cdot \mathbf{v}$, right panel) of the simulation cube. The mass density is

cut off at the average value $\langle\rho\rangle = 8.2 \times 10^{-22}$ g/cm^3, so that we plot only the high density regions. These regions are highly filamentary and fill only a small volume of the cloud. The convergence has been normalised by $\sigma/\Delta x$ where σ is the 3D velocity dispersion of the cloud and Δx is the cell size. There is a rough correlation between regions of strong convergence and regions of high density. This would be expected if the highest densities in turbulent clouds are post-shock layers.

3.4.1 Search Thresholds

While SHOCKFIND could check for shocks at every cell in the simulation, it would be computationally expensive to check all 512^3 cells of this simulation. Considering that non-converging cells can be ruled out as shock candidates without further analysis, we develop search criteria to speed up the process.

Fig. 3.5 shows the probability distribution functions (PDFs) of the convergence (upper) and the magnitude of the gradient of density (lower). The magnitude of the gradient of density has been normalised by $\langle\rho\rangle/\Delta x$ where $\langle\rho\rangle$ is the average mass density. We can estimate the convergence and gradient across a shock wave with shock velocity v_s propagating into a gas with pre-shock mass density ρ_0 as

$$\left(-\nabla\cdot\mathbf{v}\right)_\mathrm{s} \sim -\frac{v_2 - v_\mathrm{s}}{N\Delta x}, \tag{3.4.1}$$

$$\left(\nabla\rho\right)_\mathrm{s} \sim \frac{\rho_2 - \rho_0}{N\Delta x}, \tag{3.4.2}$$

where v_2 is the post-shock velocity, ρ_2 is the post-shock mass density and N is the number of cells the simulation typically spreads a discontinuity over. We use N=3 in this work. Using the relation $\rho_2 v_2 = \rho_0 v_\mathrm{s}$ and normalising as above, these estimates become

$$\frac{\left(-\nabla\cdot\mathbf{v}\right)_\mathrm{s}}{\sigma/\Delta x} \sim \frac{v_\mathrm{s}}{\sigma}\frac{r-1}{rN}, \tag{3.4.3}$$

$$\frac{\left(\nabla\rho\right)_\mathrm{s}}{\langle\rho\rangle/\Delta x} \sim \frac{\rho_0}{\langle\rho\rangle}\frac{r-1}{N}, \tag{3.4.4}$$

where $r = \rho_2/\rho_0$ is the compression ratio. We use the compression ratio r to control the search thresholds of step (i) of the algorithm (section 3.3.1). In Fig. 3.5 the dashed vertical lines show the thresholds for shock velocity $v_s = 1$ km/s, compression ratio $r = 4$, and pre-shock density $\rho_0 = 10\,\langle\rho\rangle$. As these thresholds are treated independently (Step (i) of section 3.3.1), cells that do not satisfy one threshold may still be identified as a shock candidate if they satisfy the other threhold. This conservative approach means we look at more cells than if we applied both thresholds simultaneously. At a velocity of 1 km/s, a slow shock will reach a peak temperature

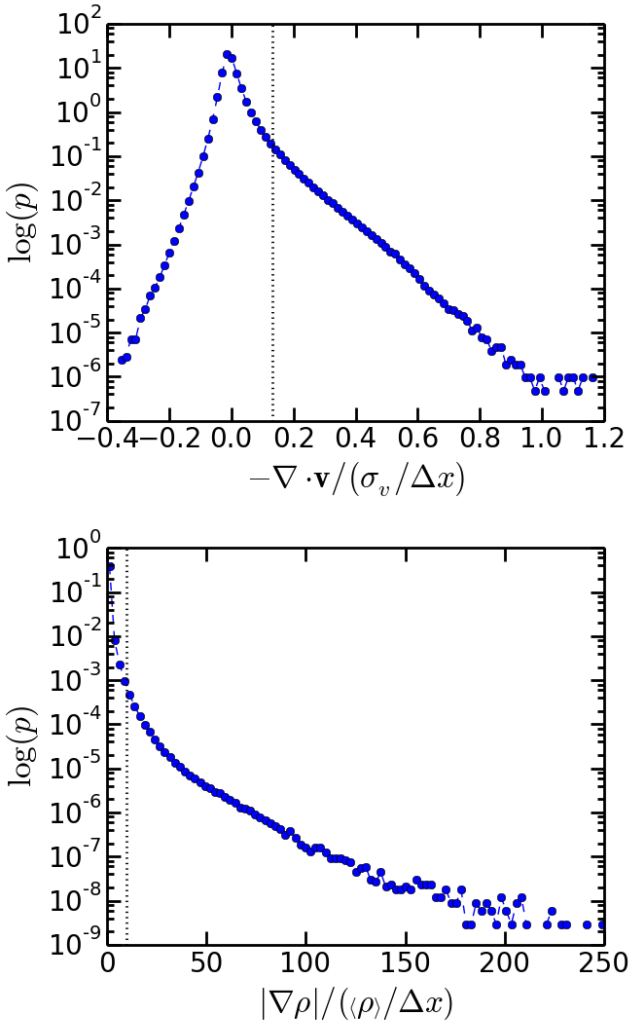

Figure 3.5: Distribution of (upper) normalised convergence and (lower) normalised magnitude of gradient. The dashed vertical lines are the search thresholds, which estimates the convergence and density gradient of a shock with velocity $v_s = 1$ km/s, pre-shock density $\rho_0 = 10\,\langle\rho\rangle$ and compression ratio $r = 4$ spread over 3 cells (see text for details of estimate).

of 55 K (equation (3.2.5)). Molecular cooling is more efficient at high temperatures and high densities, and so running the algorithm at cells above these thresholds ensures we extract the most observationally relevant shocks.

3.4.2 Shock family statistics

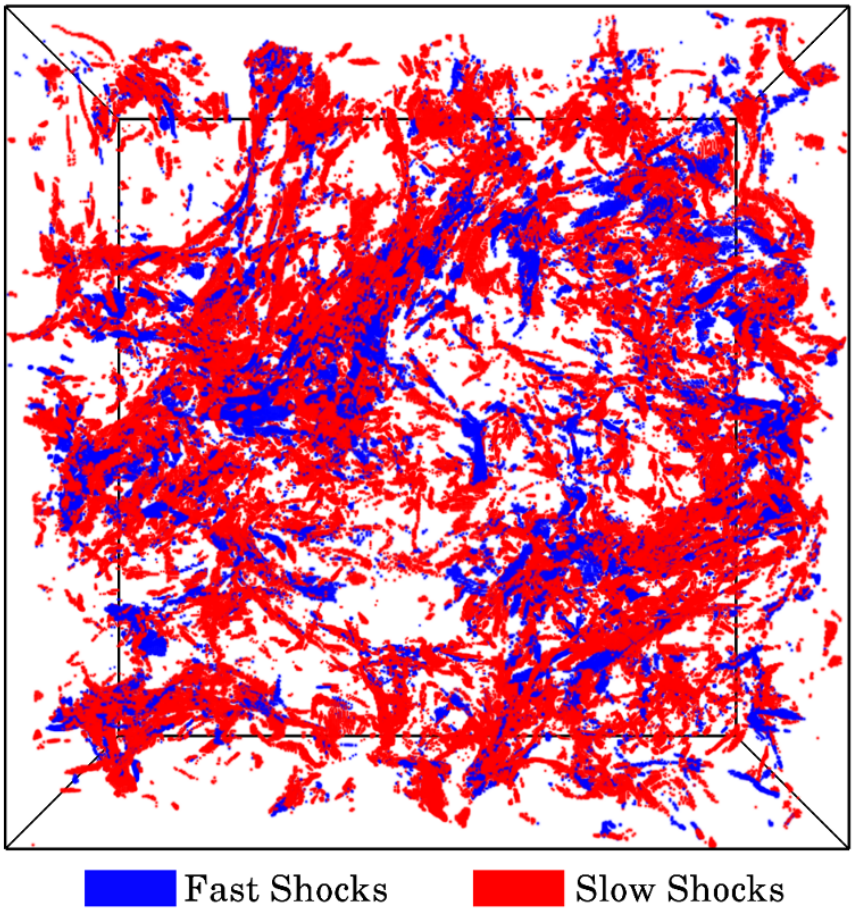

Figure 3.6: Spatial distribution of the shocks that we detected with our new shock-detection algorithm SHOCKFIND.

Using the thresholds defined in the previous section, the spatial distribution of fast and slow shocked cells is shown in Fig. 3.6. Red points refer to slow shocks and blue points refer to fast shocks. Many of the detected cells form connected shock front sheets and others form long filamentary structures. Around 40% of searched cells fail to consistently satisfy the Alfvénic Mach number and magnetic field ratio criteria (Step (vi) of section 3.3.1). A further half of the detected shocked cells are

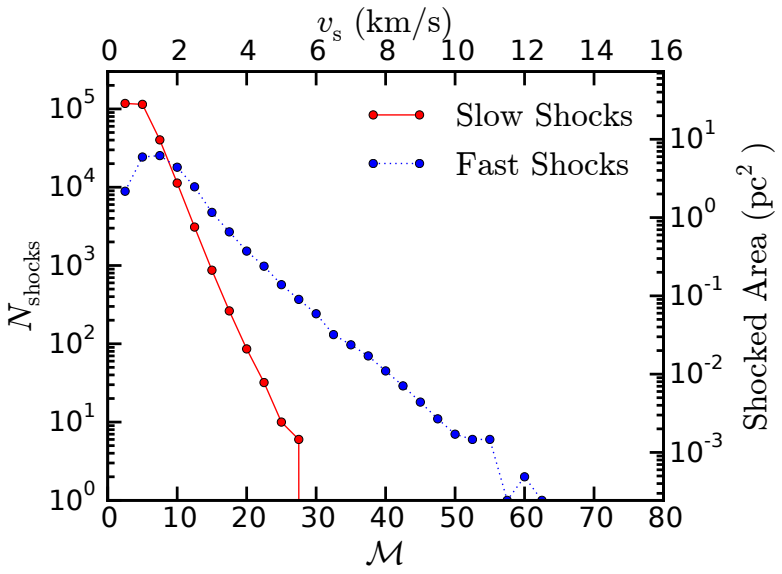

Figure 3.7: Distribution of sonic Mach numbers in bins centred on every $v_s = 0.5$ km/s with size 0.5 km/s. The blue (dotted) line refers to fast shocks and red (solid) line refers to slow shocks. The right axis shows the area that the shock fronts occupy.

filtered out because they do not lie on local maxima in convergence (Step (vii) of section 3.3.1). We analyse the results of this search in the following sections.

Fig. 3.7 shows the distributions of sonic Mach numbers for fast shocks (blue) and slow shocks (red). The slow shock distribution steeply and monotonically decreases, with a larger number of slow shocks than fast below $\mathcal{M} \sim 8$ ($v_s \sim 1.5$ km/s). The fast shock distribution peaks around $\mathcal{M} \sim 10$ before slowly decreasing. We estimate the area occupied by the shock fronts by treating each detected shocked cell as having an area of one of its faces: $(\Delta x)^2 \sim 2.4{\times}10^{-4}$ pc^2. We perform a convergence test shown in Appendix A.3. While there are more very low velocity shocks ($\mathcal{M} < 5$) to be found below our thresholds defined in section 3.4.1, the Mach number distributions are well converged for the most observationally relevant shocks. Fig. 3.8 shows the distributions of Alfvénic Mach numbers for fast shocks (blue) and slow shocks (red). By definition slow shocks are sub-Alfvénic and fast shocks are super-Alfvénic and so the distributions distinctly lie on either side of unity. In the two-fluid MHD shocks of Chapter 2 the peak temperature of slow shocks is determined by the sonic Mach number, whereas for fast shocks it is determined by the competition of molecular cooling and ion-neutral collisional heating. In section 3.5.2 we use these two distributions (Figs. 3.7 and 3.8) to make an estimate of turbulence-driven shock heating.

In Fig. 3.9 we plot the distributions of pre-shock magnetic field strengths and

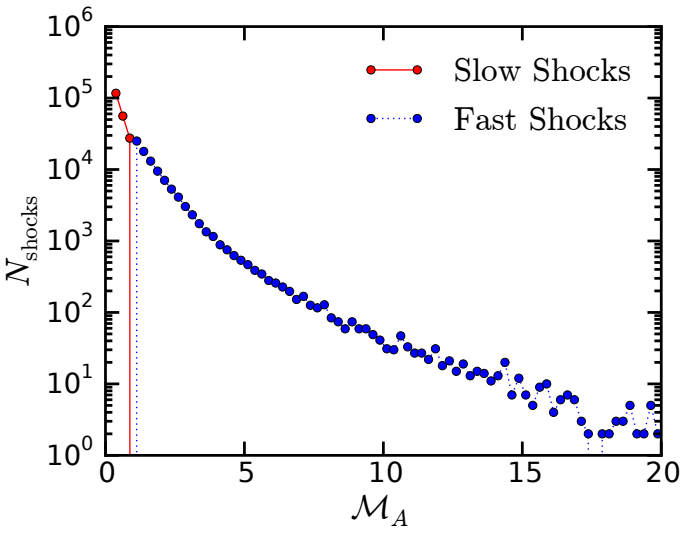

Figure 3.8: Distribution of Alfvénic Mach numbers, with bin boundaries every 0.25. The blue (dotted) line refers to fast shocks and red (solid) line refers to slow shocks.

mass densities for the search described above. These distributions give us the typical pre-shock variables that should be used to model shocks relevant to molecular cloud turbulence. They show that the typical pre-shock conditions are different for fast and slow shocks. For example, for fast shocks the average pre-shock mass density $\langle\rho_0\rangle_{\rm f} \sim 2\times10^{-21}$ g/cm^3 whereas for slow shocks $\langle\rho_0\rangle_{\rm s} \sim 9\times10^{-22}$ g/cm^3. This corresponds to total hydrogen densities, $n_{\rm H} = n({\rm HI}) + 2n({\rm H_2})$, of 8×10^2 cm^{-3} and 4×10^2 cm^{-3}, respectively (using $\rho = 1.4 m_{\rm H} n_{\rm H}$). In addition, for fast shocks the average pre-shock magnetic field strength $\langle B_0\rangle \sim 10\,\mu$G, whereas for slow shocks $\langle B_0\rangle \sim 17\,\mu$G. The average pre-shock density and magnetic field strength for fast shocks are within the ranges used by Pon et al. (2012) to model two-fluid C-type fast shocks. While the average density jump is much higher in slow shocks, $r \sim 15$, than in fast shocks, $r \sim 4$, the average post-shock densities are remarkably similiar: $\langle\rho_2\rangle_{\rm f,s} \sim 6\times10^{-21}$ g/cm^3. This implies that both kinds of shocks are equally important with respect to star formation because it is the post-shock gas that sets the initial conditions for dense-core and star formation (Padoan and Nordlund, 2011; Federrath and Klessen, 2012; Padoan et al., 2014).

These distributions suggest that to understand the impact that MHD shocks have on molecular clouds we need to understand both fast and slow MHD shocks. In a future work we will apply this algorithm to other MHD simulations of molecular cloud turbulence (e.g., Federrath and Klessen, 2012; Federrath, 2015). We will investigate how the mixture of shock families may depend on the parameters of

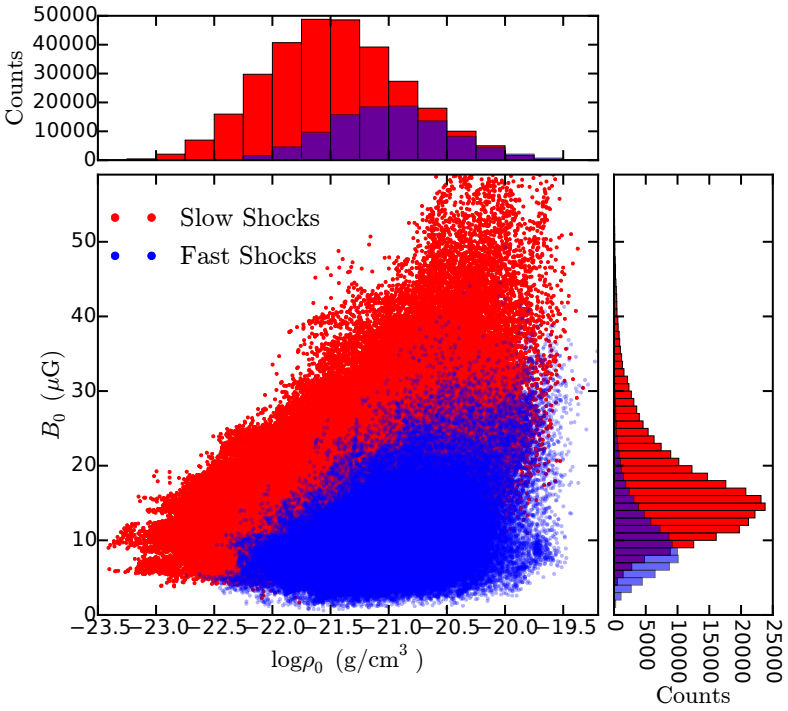

Figure 3.9: Distribution of pre-shock magnetic field strengths and mass densities.

turbulence, e.g. the initial magnetic field strength, inclusion of extra physics such as self-gravity or protostellar jet feedback. If the mixture of shock types proves to be sensitive to these parameters, then differences in observational signatures between the shock types become signatures of these parameters. In section 3.5.2 we discuss how one can use the shock mixture to compute the filling factor of hot, dense shocked gas.

3.4.3 Energetics

We may also consider the energetics of the shocks by comparing the kinetic energy dissipated in the shocks to the energy available in the turbulent motions. The kinetic flux through a unit area of shockfront is

$$K = \frac{1}{2}\rho_0 v_{\rm s}^3 \tag{3.4.5}$$

and the turbulent energy density is

$$\Gamma = \frac{1}{2}\langle\rho\rangle\,\sigma^2, \tag{3.4.6}$$

where σ is the velocity dispersion. Thus the timescale for dissipation in turbulence-driven shocks is

$$\tau_D = \Gamma V / \sum_K \left(K \left(\Delta x \right)^2 \right), \tag{3.4.7}$$

where V is the volume of the simulation (8^3 pc^3) and the summation is over the detected shocked cells.

For the shocks shown in Fig. 3.6, fast shocks dissipate ~ 8 times more energy than slow shocks due to the high velocity tail seen in Fig. 3.7. Note that not all of the kinetic energy from fast shocks dissipates by cooling, however, as some fraction goes into strengthening the magnetic field (as discussed in section 3.2). Applying the MHD jump conditions for fast shocks with velocities ranging from 1–2 km/s, propagating into gas with the average fast pre-shock density $\langle \rho_0 \rangle_{\rm f} \sim 2 \times 10^{-21}$ g/cm^3 and average pre-shock magnetic field strength $\langle B_0 \rangle \sim 10\,\mu$G, we find that 35–70% of the kinetic flux is lost to the magnetic field, depending on the orientation of the shock direction with respect to the magnetic field. As energy stored in the magnetic field is free to further dynamically impact the turbulence, we reduce the energy dissipated by fast shocks by a factor of 2 in order to capture the energy being dissipated as heat.

Considering all shocks together, the shock dissipation rate is $\sim 0.2\,{\rm L}_\odot$. Compared to the turbulent kinetic energy, this gives a dissipation timescale of $\tau_D \sim 8$ Myrs. This is ~ 1.3 times the eddy turnover time $\tau_l = \left(\sqrt{3} L/2 \right) / \sigma_{\rm 1D}$ where $\sqrt{3}L$ is the size of the diagonal of the simulation and $\sigma_{\rm 1D} = \sigma/\sqrt{3}$ is the one-dimensional velocity dispersion. From observations of turbulent dissipation regions, Pon et al. (2014) estimated this ratio to be 1/3 in the Perseus molecular cloud and Larson et al. (2015) made estimates of 0.94 and 0.65 for two shock models in the Taurus molecular cloud. Previous simulations have suggested that shocks dissipate around 50% of the turbulent kinetic energy (Stone et al., 1998). If we take this into account, our predicted ratio τ_D/τ_l would be reduced by a factor of 2, placing it in the middle of these obversational results.

3.5 Discussion

We have presented an algorithm to detect and characterise fast and slow MHD shock waves in simulations of turbulent molecular clouds. While there is some observational evidence for the presence of fast (Lesaffre et al., 2013; Pon et al., 2014; Larson et al., 2015) and slow (chapter 2) MHD shocks in molecular clouds, we present in this work the first prediction of the relative fraction of fast and slow shocks in molecular clouds. We characterised the shocks and provide the typical pre-shock conditions that should be used in future shock models that wish to model

turbulence-driven MHD shocks. In the following we compare our work with other shock-finding algorithms, and then discuss how the results of the algorithm can be used to obtain an estimate of the volume of shock heated gas.

3.5.1 Comparison to previous work

Smith et al. (2000b) and Smith et al. (2000a) developed a method for counting shocks in MHD simulations of decaying and driven turbulence, respectively. Their method computes the velocity jump across converging regions. They found that the number distribution of these jumps did not substantially differ with the addition of a magnetic field. Our results are qualitatively similar, with weaker shocks dominating the number distribution, though they find much lower Mach numbers in general. This could be because they do not consider the shock reference frame, which introduces a correction to the velocity jump (see step (v) of section 3.3.1). Their method does not explicitly disentangle the MHD shock types, and so cannot quantify the relative importance of fast or slow shocks.

The importance of shock heating on the chemical evolution of turbulent molecular clouds is highlighted by Kumar and Fisher (2013). Like our work they capture the effects of shock heating on subgrid scales. They do this by post-processing Lagrangian tracer particles in a simulation of hydrodynamic turbulence. Their subgrid model is a one-dimensional integration of the fluid equations including a vast chemical network and molecular cooling. They were able to distinguish between chemicals that trace the mean physical state of cloud, and those that trace the non-equilibrium shock-heated gas. Their method also accounts for solenoidal heating and so they can measure the relative importance of these two heating mechanisms. However, as they only consider hydrodynamic turbulence, their results are not sensitive to the distinct effects of MHD shock types. Extending their work to the MHD case is in principle simple. The subgrid model would need to include MHD effects like the shock models of Flower and Pineau Des Forêts (2010), Pon et al. (2012) or Chapter 2 of this thesis. Some difficulty lies in obtaining the pre-shock state, which requires knowledge of the magnetic field direction with respect to the shock propagation direction. In addition, the pre-shock state does not uniquely determine the MHD shock type (cf Kennel et al., 1989). We have addressed this problem by using both pre- and post-shock information in order to ascertain two of the three possible shock types.

The shock finding algorithm most similar to SHOCKFIND is that outlined in Schaal and Springel (2015). They look for shocks in cosmological hydrodynamic simulations. Their method flags cells of converging flow, and defines the shock direction using the gradient of the temperature. They then use a series of criteria to filter spurious shock detections. While their work does not include magnetic fields, and thus does not consider different shock families, it would be simple to extend

their algorithm to do so. It would only take the addition of further filtering criteria such as we presented in step (vi) of section 3.3.1. This extension would allow for a comparison of our work to MHD simulations using moving-mesh codes such as AREPO (Springel, 2010; Pakmor et al., 2011).

3.5.2 Shock heating

Chapter 2 showed that C-type fast MHD shocks and J-type slow MHD shocks distinctly heat the gas they propagate through. The fast shocks modeled in Chapter 2 reach peak temperatures of $\sim$ 150 K, whereas slow shocks could reach temperatures of $\sim$ 800 K. This is because in the weakly ionized gas that makes up molecular clouds, the heating timescale in fast shocks is determined by the ion-neutral collision timescale, which is slower than the cooling timescale. In contrast, in slow shocks, the neutral-ion collision timescale is shorter than the cooling timescale, such that heating in slow shocks is more significant. Even though these high temperatures only occupy a thin shock layer, the heating is important because of the rich chemistry it activates. The chemical signatures of shocks may persist in regions of unshocked gas. In this section we use the pre-shock conditions (Fig. 3.9) and shock front area (Fig. 3.7) obtained by SHOCKFIND, combined with representative sub-grid two-fluid shock models from Chapter 2 to estimate the volume of shocked gas in a turbulent cloud.

Sub-grid two-fluid shock models

Ion-neutral collisions determine shock thickness in two-fluid shocks, and so the ionization fraction is a key variable in determining the volume filling fraction of shocks. Ionization sources, such as cosmic-rays and ultraviolet photons, are density dependent and so the ionization fraction spatially varies in a turbulent cloud. For simplicity we adopt the ionization fraction of Bergin and Tafalla (2007): $x_e = 1.3 \times 10^{-5} n(\mathrm{H_2})^{-1/2}$ where we use the density in the pre-shock gas. This leads to pre-shock ionization fractions ranging between 2×10^{-7} and 9×10^{-6}.

For slow MHD shocks, the shock thickness is independent of the pre-shock magnetic field strength. So, for a given pre-shock density, we choose the magnetic field such that the Alfvén velocity $v_\mathrm{A} = 3$ km/s. This allows us to compute slow shocks with speeds up to $v_\mathrm{A} \cos\theta$, where θ is the angle between the direction of propagation and pre-shock magnetic field. We model slow MHD shocks for $\theta = 30^\circ$ allowing shock velocities up to 2.5 km/s. The number of slow shocks above this velocity in the simulation is only $\sim$ 0.7% of all slow shocks (see Fig. 3.7), so our results are only negligibly affected by this limit. Fig. 3.10 shows the thicknesses of slow MHD shocks heated above 50 K and 100 K, for pre-shock total hydrogen densities ranging between 10 and 10^3 cm^{-3}. The hot shock front is largest for models with the lowest

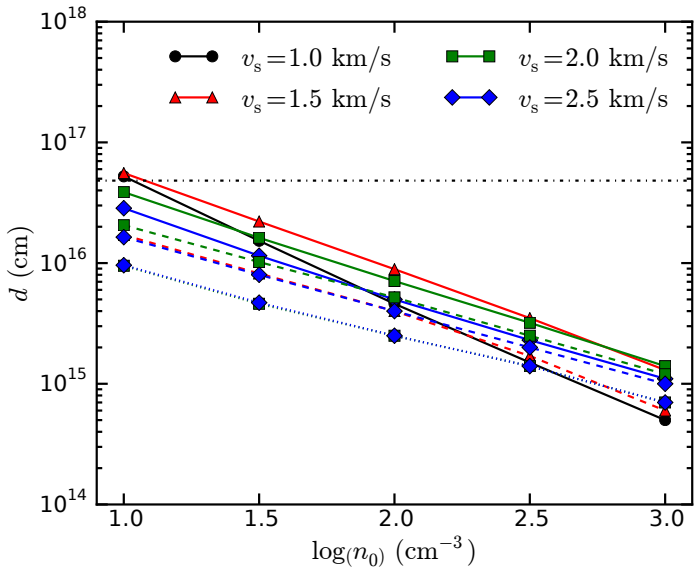

Figure 3.10: Thickness of slow MHD shocks versus preshock total hydrogen density. The solid, dashed and dotted lines show shock thicknesses above 50, 100 and 150 K, respectively. Each line of the same colour (or marker) represents models with the same shock velocity. The horizontal dash-dotted line shows the size of a cell in the turbulent cloud simulation.

pre-shock density and lowest velocity, peaking at $\sim 6\times10^{16}$ cm which is of the order of the size of a cell Δx. This is important because it means that the substructure within the shock front would not dynamically affect the scales that the simulation captures.

For fast MHD shocks with a given pre-shock density, we choose the magnetic field such that the Alfvén velocity $v_{\rm A} = 1$ km/s. The shock thickness, d, of two-fluid fast C-type shocks is estimated as

$$d \sim \frac{v_{\rm s}}{n_i \alpha}, \tag{3.5.1}$$

where $n_i = x_{\rm e} n_{\rm H}$ is the number density of ions and $\alpha = 1.6 \times 10^{-9}$ cm^3/s is the rate coefficient for ion-neutral scattering. This shock thickness estimate can exceed the simulation box size at low densities and large shock velocities, which means, of course, that some fast shock models are innapropriate as sub-grid models in this ideal MHD simulation. Thus we consider models with thickness $d \leq 10\Delta x$ as small enough to not significantly affect the simulation results. Note that this estimate gives the thickness of steady-state fast shocks. Factoring in the structure of non-steady shocks is beyond the scope of this work. Finally, we find that models of fast

shocks for these Mach numbers and densities in the range $n_{\rm H} = 10$–10^3 cm^{-3} are all C-type shocks.

We bin the detected shocks into pre-shock total hydrogen densities centred on 10^1, $10^{1.5}$, $10^{2.0}$, $10^{2.5}$ and $10^{3.0}$ cm^{-3}. These values of density almost cover the entire range of detected shocks, with $\lesssim 5\%$ of slow shocks and $\lesssim 2\%$ of fast shocks falling outside. With this binning, we can use the shock thicknesses from Fig. 3.10 to estimate the volume of warm shocked gas. Using the area computed for Fig. 3.7 multiplied by the shock thicknesses we find that $f_{\rm T>50\,K} \sim 0.03\%$ of the volume is filled with shocked gas greater than 50 K. This is of the order of the shocked volume filling factor measurement of Pon et al. (2014) from turbulent dissipation regions in the Perseus molecular cloud. In addition, $f_{\rm T>100\,K} \sim 5 \times 10^{-3}\%$ and $f_{\rm T>150\,K} \sim 9 \times 10^{-4}\%$ of the volume is filled with shocked gas greater than 100 K and 150 K, respectively. This warm gas occurs entirely in slow shocks, because the fast shocks at these conditions do not reach peak temperatures above 50 K. Hence, if no distinction of MHD shock families is made and all shocks in an MHD simulation were assumed to be fast C-type shocks, there would be no warm component of gas with temperature $T > 50$ K at all.

Rotational line emission

While this predicted filling factor of gas hotter than 50 K, $\sim 0.03\%$, is very small, only $\sim 2.5\%$ of the volume is filled with gas at densities higher than the average post-shock density $\langle \rho_2 \rangle \sim 6 \times 10^{-21}$ g/cm^3. As an example observational impact of this warm gas, we estimate the intensity of a CO rotational line using the non local thermodynamic equilibrium (LTE) radiative transfer code RADEX (van der Tak et al., 2007).

For a given radiating molecule, RADEX requires as input the density of H_2 as the collisional partner, the column density of the radiating molecule, the temperature and the linewidth. In order to avoid geometrical effects, we consider only optically thin lines. By doing this, we can use RADEX in slab mode and treat each column through the simulation as consisting of a simple addition of slabs. We use the shock thicknesses computed above to define at each cell (on one face) the column density excited by gas at 75, 125 and 175 K. We use a CO abundance of $x({\rm CO}) = n({\rm CO})/n_{\rm H} = 1.2 \times 10^{-4}$ to derive the CO column density. We then take the density of H_2 to be equal to the average post-shock density, obtained as in step 4 in section 3.3.1. We assume that the rest of the gas makes up a column of CO excited by 10 K gas at an H_2 density equal to the average density in the simulation. Finally, we use the velocity dispersion of the cloud as the input linewidth.

Fig. 3.11 shows the synthetic map of RADEX estimated CO J=9-8 intensities with contours of total hydrogen column density overlaid. We chose the J=9-8 line because it was the lowest J CO line that was optically thin at the column densities reached

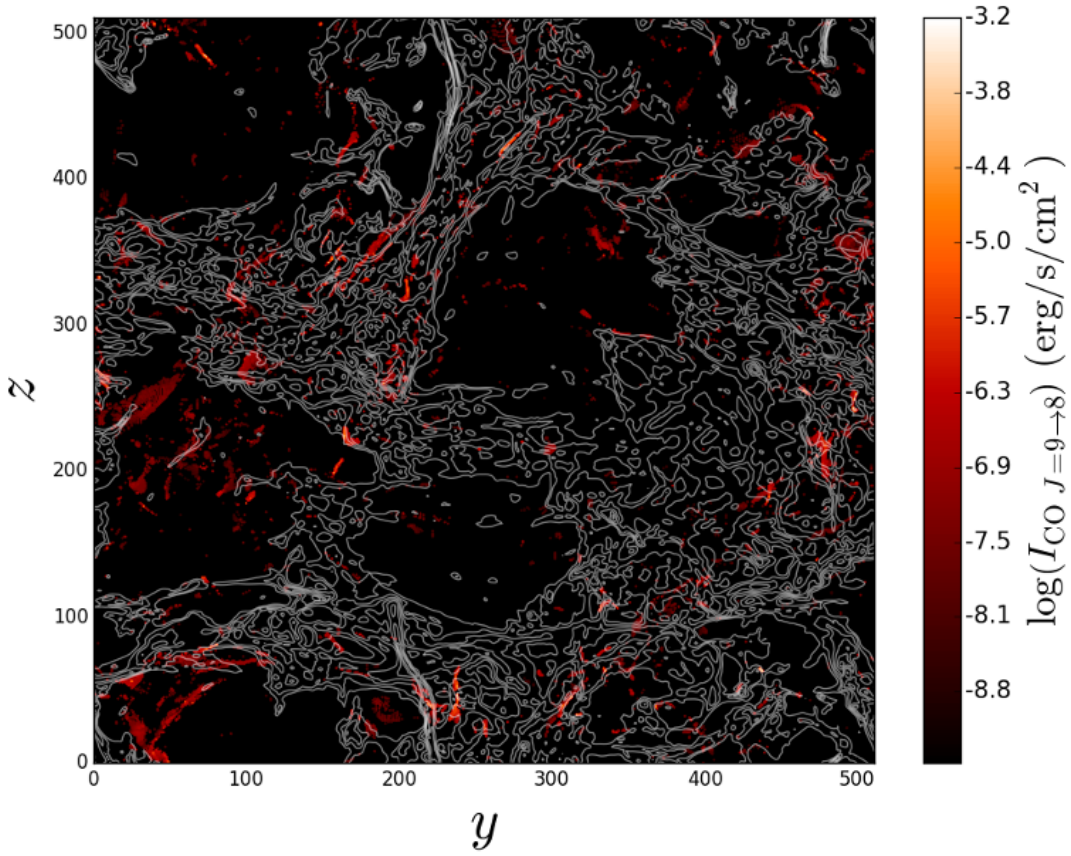

Figure 3.11: Predicted synthetic radio emission map of the simulation in the CO J=9–8 rotational transition, computed with RADEX. The white line contours are of the total hydrogen column density, equally spaced from the average column over the whole face ($\langle N_{\rm H} \rangle \sim 10^{24.5}$ cm^{-2}) up to the maximum column ($N_{\rm H,max} \sim 10^{25.5}$ cm^{-2}).

here and because another source of high-J CO lines, photodissociation regions, may have difficulties producing significant emission at this line and above (Pon et al., 2012). The emission in Fig. 3.11 is entirely due to shocks—as the background 10 K gas negligibly emits in this line—and is strongest in filamentary structures. This is because an edge-on shock, with respect to the line of sight, presents a larger column of heated gas than a face-on shock. These filamentary emission regions also tend to occur in regions with large hydrogen column densities, suggesting that the pre-shocked gas is already at a high density. The correlation between large hydrogen column density and emission is not perfect, however, as there is some significant CO emission at regions of below average hydrogen column density. If we add up the emission from over the whole face of the cloud, then the total cloud luminosity at this line is $\sim 4 \times 10^{-3}\,\mathrm{L}_{\odot}$. Notably, if we ignored the distinction of MHD shock families and assumed that all shocks were the well-studied C-type fast shocks, we would predict that the CO J=9-8 emission would be negligible.

Estimates of high-J CO lines like this could provide distinct observational predictions between different simulations of turbulent clouds. The accuracy of this estimate depends on the accuracy of the estimate of the volume of warm gas. This was estimated using the shock thicknesses derived from the two-fluid shock models of Chapter 2. It also only included the gas heated by slow shocks, because some two-fluid C-type fast shocks have thicknesses too large to be applicable to this simulation and the remaining fast shocks do not reach peak temperature of 50 K. This implies that a large proportion of the fast shocks detected here would not have the steady-state structure of two-fluid fast shocks. We have also ignored the possibility of intermediate MHD shocks, because they do not have the predictable impact on magnetic fields that this algorithm exploits. In addition, the shock models of Chapter 2 are highly simplified in order to highlight the differences between fast and slow shocks. Improvements in models of shocks, such as using an expanded chemical network and including the effects of dust grains, would improve the accuracy of the shock-heated volume estimate.

3.6 Conclusion

A publicly available algorithm, SHOCKFIND[1], was developed that extracts and characterises the shock waves in MHD simulations. This algorithm was applied to a high-resolution simulation of a magnetised, turbulent molecular cloud. We presented the first prediction of the relative fraction of fast and slow MHD shocks in a turbulent molecular cloud simulation. The sonic and Alfvénic Mach number distributions for these two families of shocks are distinct and confirm that low-velocities,

[1]Found on BitBucket (https://bitbucket.org/shockfind/shockfind) and the PYTHON Package Index (https://pypi.python.org/pypi/shockfind)

below $v_s = 3$ km/s, dominate the population of shocks. By considering the energetics of the detected shocks, we found that the ratio of the shock dissipation timescale to cloud crossing time is comparable to observed values from turbulent dissipation regions in molecular clouds. We have also used simple sub-grid models of two-fluid MHD shocks from Chapter 2 to estimate the heating that would occur within the thin shock front of these extracted shocks. Slow MHD shocks were found to produce a low volume filling factor, $\sim 0.03\%$, component of the cloud heated above 50 K with a small portion of this component reaching temperatures above 150 K. We used the non-LTE radiative transfer code RADEX to estimate the intensity of a high-J CO rotational transition and found that the shock-heated gas radiates far above the background cloud intensity. High-J CO line emission may therefore be an important observational diagnostic of shocks in molecular clouds.

Our shock-detection algorithm is general enough to be applied widely to MHD simulations of other astrophysical phenomena. It would be interesting to see the mixture of shock families that might be present in simulations of supernovae shocks, protostellar jets interacting with the interstellar medium, colliding flows, cloud-cloud collisions, etc. In a future work we plan to extract and characterise the MHD shocks in a variety of simulations of turbulent molecular clouds in order to search for correlations between the parameters of turbulence and possible observational effects of MHD shock waves.

Chapter 4

Shocks in Galactic Centre molecular clouds

Abstract

The molecular clouds near the centre of the Galaxy are ideal testbeds for star formation processes due to their atypical properties. Consistently high gas temperatures (>50 K) have been found throughout this region, demanding a global heating mechanism. Large linewidths suggest that strong turbulence is present, and its dissipation naturally explains the high temperatures. We search for chemical signatures of turbulent damping by modeling two-fluid magnetohydrodynamic shocks that are expected to dominate the dissipation. By comparing shock chemistry to equilibrium cloud chemistry, we identify signatures of shocked gas in enhancements of various species. In particular, the abundances of sulphur-bearing species SO, SO_2 and H_2S are sensitive to the hot shocked gas, even if the shock fronts only occupy 0.1% of the line-of-sight column density. We discuss how observations of particular species could constrain the physical parameters of Galactic Centre molecular clouds, such as the cosmic-ray ionization rate and gas volume density.

4.1 Introduction

The unusual molecular clouds in the central 250 pc of the Milky Way contain around 10 % of the dense gas ($n > 10^3$ cm^{-3}) in the Galaxy, yet account for less than 1 % of the star formation. Compared to clouds in the disk of the galaxy, the clouds of the Central Molecular Zone (CMZ) are hotter, more dense, and contain stronger magnetic fields and larger velocity dispersions (see review by Morris and Serabyn, 1996). The stark differences in the conditions in which stars form make these clouds important test beds for theories of star formation.

Global studies of the CMZ have consistently shown gas temperatures in excess of 50 K. Such high kinetic temperatures have been measured in moderate density gas (total hydrogen density $n_{\rm H} \sim 10^3$–10^4 cm^{-3}) using metastable inversion lines of ammonia (Mills and Morris, 2013; Ott et al., 2014), and in high density gas ($n_{\rm H} \sim 10^4$–10^5 cm^{-3}) using emission from para-formaldehyde (Ao et al., 2013; Ginsburg et al., 2016; Immer et al., 2016). In contrast, molecular clouds in the disk of the galaxy generally have temperatures around 10 K. These CMZ gas temperatures are found to be decoupled from cooler dust temperatures, $T_D \lesssim 20$ K (Molinari et al., 2011), ruling out UV irradiation as a dominant heating mechanism (Ao et al., 2013). Cosmic-ray ionization rates larger than the canonical rate ($\zeta = 10^{-17}$ s^{-1} H^{-1}) by 2–3 orders of magnitude (as inferred by Goto et al., 2008; Yusef-Zadeh et al., 2013b) can explain elevated gas temperatures. However, the large scatter in gas temperatures requires a spatially non-uniform ionization rate or a different heating mechanism. Heating by the dissipation of turbulence has therefore become a popular hypothesis (Ao et al., 2013; Ginsburg et al., 2016; Immer et al., 2016), naturally explaining both the high temperatures and their spatial inhomogeneity.

Clouds in the CMZ are highly supersonic, with typical linewidths of 20 km s^{-1} compared to Milky Way cloud linewidths $\lesssim 10$ km s^{-1} (Shetty et al., 2012). Supersonic flows will inevitably form shock waves, which dissipate the turbulent kinetic energy along with vortices (Pety and Falgarone, 2000). Simulations of have shown that shocks are ubiquitous in turbulent molecular clouds (Stone et al., 1998; Smith et al., 2000b,a). The heating in a thin shock front uniquely drives chemistry and radiative cooling, and so the observational signatures of supersonic turbulence are shaped by microphysical processes in shocks.

The main goal of this work is to provide direct chemical signatures of the turbulent dissipation in clouds in the CMZ by using magnetohydrodynamic (MHD) shock models. Models of low-velocity ($v_s \lesssim 4$ km s^{-1}) C-type fast MHD shocks (Pon et al., 2012) and J-type slow MHD shocks (chapter 2) have had some success interpreting observations of galactic infrared dark clouds (Pon et al., 2014, 2015, 2016a) and protostellar clumps (Larson et al., 2015). In C-type shocks, the dissipation takes place over a broad region of ion-neutral drift driven by magnetic pressure. In contrast,

Table 4.1: The 99 species included in our network

H	He	C	N	O	Mg	S	Fe	H_2
C_2	C_3	C_4	C_5	C_6	N_2	O_2	CH	CH_2
CH_3	CH_4	C_2H	C_2H_2	C_3H	C_3H_2	C_6H	NH	NH_2
NH_3	OH	H_2O	H_2S	CN	CO	CO_2	NO	CS
SO	SO_2	HCN	HNC	H_2CO	CH_3OH	OCS	H^+	He^+
C^+	O^+	S^+	Fe^+	H_2^+	H_3^+	C_2^+	C_3^+	N^+
N_2^+	O_2^+	CH^+	CH_2^+	CH_3^+	CH_4^+	CH_5^+	C_2H^+	$C_2H_2^+$
$C_2H_3^+$	C_3H^+	$C_3H_2^+$	$C_3H_3^+$	C_4H^+	C_6H^+	$C_6H_2^+$	NH^+	NH_2^+
NH_3^+	NH_4^+	N_2H^+	OH^+	H_2O^+	H_3O^+	H_2S^+	H_3S^+	CN^+
C_2N^+	CO^+	NO^+	CS^+	SO^+	HCN^+	H_2NC^+	HNO^+	HCO^+
HCO_2^+	HCS^+	HSO^+	HSO_2^+	$HOCS^+$				

slow shock dissipation occurs in a narrow region driven by gas pressure, reaching higher peak temperatures than fast shocks of the same velocity (chapter 2). We extend the models of chapter 2 by using an expanded chemical network, updated cooling functions and moderate shock velocities ($v_s \sim 8$ km s^{-1}). In section 4.2, we outline the equilibrium cloud models used for comparison. In section 4.3 we discuss the two-fluid shock models. In section 4.4 we present our results, and discuss their implications for the physical state of CMZ clouds.

4.2 Equilibrium Clouds

To identify unique tracers of turbulent dissipation, we model a non-turbulent cloud as one in chemical equilibrium. The equilibrium clouds also provide the initial chemical and thermal state for the shock models in section 4.3. In this section, we describe the chemical reactions and thermal processes included in the model as we simultaneously solve for the time-dependent densities of chemical species and the thermal balance.

4.2.1 Chemical Network and Rate Equations

To model equilibrium clouds, we solve a coupled ordinary differential equation for each species, M

$$\frac{dn_M}{dt} = S\left(M\right), \tag{4.2.1}$$

where $S(M)$ is the volume rate of creation or destruction of M. In general, $S(M)$ will be a function of temperature and densities of various species. We use the open

source PYTHON module *scikits.odes*[1], which solves initial value problems for ODEs using variable-order, variable-step, multistep methods.

We use the gas-phase chemical network of Le Gal et al. (2014), which updates and expands on the network of Flower et al. (2006). This network includes the usual carbon and oxygen chemistry of interstellar clouds, but also includes sulphur- and nitrogen-bearing species, important tracers of MHD shocks (e.g. Pineau des Forêts et al., 1990, 1993). The inclusion of nitrogen-bearing species is additionally motivated by observations of molecules such as HCN and HNC in the CMZ (Jones et al., 2012) and nuclear regions of external galaxies (Loenen et al., 2008) that have proven difficult to reproduce with standard models of photodissociation regions.

The reaction rates are taken from the RATE12 UMIST database for astrochemistry (McElroy et al., 2013). This database does not include reaction rates for all species in the Le Gal et al. (2014) network, for instance rates for OD^+ or separate rates for ortho, para or meta states of H_2, H_2^+, H_3^+, NH_2, NH_2^+, NH_3^+ or NH_4^+. For simplicity we assume these species are not split into separate states. We found for typical dark cloud parameters that the remaining network did not attain steady-state by 10^8 years and that C_6H^+ became the dominant ion. By adding C_6H, $C_6H_2^+$, C_4, C_5 and C_6, the destruction pathways of C_6H^+ become accessible and steady-state of the whole network is achieved in 10^7 years. The full list of species included in our chemical network is shown in Table 4.1. In total there are 99 species and 1452 reaction rates included from RATE12, as well as the formation of H_2 on dust grains and the destruction of H_2 by photodissociation.

The RATE12 database describes reaction rate coefficients in terms of the constants α, β and γ for the various classes of gas-phase reactions listed in Table 4.2. For neutral-neutral (NN), ion-neutral (IN), charge exchange (CE), dissociative recombination (DR), radiative recombination (RR), radiative association (RA) and associative dettachment (AD) reactions the source term uses the two-body, temperature (T) dependent reaction rate coefficient

$$k_{2B}(T) = \alpha \left(\frac{T}{300}\right)^{\beta} \exp\left(-\frac{\gamma}{T}\right) \text{ cm}^3\,\text{s}^{-1}. \tag{4.2.2}$$

For ion-neutral reactions, we use an effective temperature

$$T_{\text{eff}} = \frac{m_n T_i + m_i T_n}{m_n + m_i}, \tag{4.2.3}$$

where T_n and T_i are the temperatures of the neutral and ion fluids, respectively, and m_n and m_i are the masses of the neutral and ion species in the reaction, respectively. The source term for two body reactions is then

$$S_{2B}(M) = \sum(\pm) k_{2B}(T) n(A) n(B), \tag{4.2.4}$$

[1]https://github.com/bmcage/odes

Table 4.2: Classes of reactions included from RATE12

ID	Reaction Type	Example
NN	Neutral-neutral	$O + H_2 \rightarrow OH + H$
IN	Ion-neutral	$C + OH^+ \rightarrow O + CH^+$
CE	Charge exchange	$He^+ + C \rightarrow C^+ + He$
DR	Dissociative recombination	$H_3^+ + e^- \rightarrow H + H + H$
RR	Radiative recombination	$H^+ + e^- \rightarrow H + PHOTON$
RA	Radiative association	$O + H \rightarrow OH + PHOTON$
PH	Photodissociation	$CH_3 + PHOTON \rightarrow CH + H_2$
PH	Photoionization	$H_2O + PHOTON \rightarrow H_2O^+ + e^-$
CP	Cosmic-ray ionization	$C + CRP \rightarrow C^+ + e^-$
CP	Cosmic-ray dissociation	$H_2 + CRP \rightarrow H + H$
CR	Cosmic-ray induced photoionization	$CH_3 + CRPHOT \rightarrow CH_3^+ + e^-$
CR	Cosmic-ray induced photodissociation	$CH^+ + CRPHOT \rightarrow C^+ + H$
AD	Associative detachment	$CH + O \rightarrow HCO^+ + e^-$

where the summation is over all reactions that either create (from reactants A and B) or destroy M (in which case $A = M$ or $B = M$).

For photodissociation of H_2 we follow the formulation of Draine and Bertoldi (1996)

$$S_{\rm PH}\left(H_2\right) = k_{\rm PH,0} f_{\rm shield} e^{-\tau_d} n\left(H_2\right), \tag{4.2.5}$$

where $e^{-\tau_d}$ accounts for dust attenuation with the optical depth $\tau_d = 3.02 A_{\rm V}$, and $k_{\rm PH,0}$ is the unshielded photodissociation rate equal to $2.59 \times 10^{-11} \chi$ s^{-1}. χ is a dimensionless parameter characterising the ultraviolet interstellar radiation field relative to the Habing estimate Habing (1968). $f_{\rm shield}$ is the self-shielding factor

$$f_{\rm shield}\left(N(H_2)\right) = \frac{0.965}{\left(1 + x/b\right)^2} + \frac{0.035}{\left(1+x\right)^{1/2}} \exp\left[-8.5 \times 10^{-4}\left(1+x\right)^{1/2}\right], \tag{4.2.6}$$

where $x = N\left(H_2\right)/(5 \times 10^{14}$ cm$^{-2})$ and $b = {\rm FWHM}/\left(4 \ln 2\right)^{1/2}$ is the Doppler broadening parameter for linewidth FWHM measured in km s^{-1}. For photodissociation and photoionization of species other than H_2 the rate coefficient takes the form

$$k_{\rm PH} = \alpha \chi \exp\left(-\gamma A_V\right) \text{ s}^{-1}, \tag{4.2.7}$$

where A_V is the dust extinction at visible wavelengths.

Thus the source term for photoreactions (PH) is

$$S_{\rm PH}(M) = \sum (\pm) k_{\rm PH} n(A), \tag{4.2.8}$$

where the summation is over all reactions that create M (from A) or destroy M (in which case $A = M$).

For direct cosmic-ray dissociation or ionization, the rate coefficient takes the form

$$k_{\rm CP} = \alpha \frac{\zeta}{\zeta_0} \, {\rm s}^{-1}, \tag{4.2.9}$$

where ζ is the cosmic-ray ionization rate per H nucleus and $\zeta_0 = 1.36 \times 10^{-17}$ s^{-1}. The source term for direct cosmic-ray reactions (CP) is then

$$S_{\rm CP}(M) = \sum (\pm) k_{\rm CP} n(A), \tag{4.2.10}$$

where the summation is over all reactions that create M (from A) or destroy M (in which case $A = M$).

For cosmic-ray induced photodissociation or ionization, the rate coefficient takes the form

$$k_{\rm CR} = \alpha \left(\frac{T}{300} \right)^{\beta} \frac{\zeta}{\zeta_0} \frac{\gamma}{1-\omega} \, {\rm s}^{-1}, \tag{4.2.11}$$

where ω is the dust-grain albedo in the far ultraviolet (typically 0.4–0.6 at 150 nm). We use an albedo of 0.6 throughout the present work. The source term for indirect cosmic-ray reactions (CR) is then

$$S_{\rm CR}(M) = \sum (\pm) k_{\rm CR} n(A), \tag{4.2.12}$$

where the summation is over all reactions that create M (from A) or destroy M (in which case $A = M$).

Finally, we treat the formation of H_2 on dust grains with a simple expression from Hollenbach and McKee (1979) for the reaction rate coefficient

$$k_{\rm H_2} = 5.20 \times 10^{-17} \left(\frac{T}{300} \right)^{1/2} St\left(T_g, T_d\right) f\left(T_d\right) \, {\rm cm}^3 \, {\rm s}^{-1}, \tag{4.2.13}$$

with the sticking coefficient,

$$St(T_g, T_d) = \left(1 + 0.04 \left(T_g + T_d\right)^{1/2} + 0.002 T_g + 8 \times 10^{-6} T_g^2 \right)^{-1}, \tag{4.2.14}$$

measuring the fraction of gas-phase atomic H sticking to a grain as it collides, and the fraction of atomic H on dust grains that combine to form H_2 before evaporating given by

$$f\left(T_d\right) = \frac{1}{1 + 10^{-4} \exp\left(-600/T_d\right)}. \tag{4.2.15}$$

The volume rate of H_2 formation on dust grains is then

$$S_{\rm dust}\left(H_2\right) = k_{H_2} n_{\rm H} n\left(H\right). \tag{4.2.16}$$

Two example time-dependent solutions for the chemical abundances are shown in Fig. 4.1 for selected species. For these models, we use cosmic-ray ionization rate $\zeta = 1.3{\times}10^{-17}$ s^{-1} H^{-1}, UV field $\chi = 10$, extinction $A_V = 10$, total hydrogen number density $n_{\rm H} = 10^4$ cm^{-3}, total hydrogen column density $N_{\rm H} \sim 1.6 \times 10^{22}$ cm^{-2}, and temperature fixed at 10 K. We adopt the elemental abundances of Le Gal et al. (2014) (their table 2), choosing an initial O abundance $x({\rm O}) = 1.04{\times}10^{-4}$ in order to obtain a C/O abundance ratio of 0.8 and initial S abundance $x({\rm S}) = 8{\times}10^{-8}$ as in their best model. Most species reach equilibrium between 10^6 and 10^7 years, of the order of a typical molecular cloud lifetime. Using the chemical network described above, there are large discrepancies between the abundances shown in the left panel of Fig. 4.1 and those shown in Fig. 2 of Le Gal et al. (2014). For example, the equilibrium N_2 abundance is a factor of $\sim$4 larger than the N abundance, whereas they are roughly equal in Le Gal et al.. If we modify our chemical network by adopting the chemical rate equations in Appendix B.3 of Le Gal et al., we obtain more similar results (right panel of Fig. 4.1). With this network the equilibrium abundances of N_2 and N are roughly equal, and the NO abundance has now increased to comparable levels. Major discrepancies remain, however, such as the near time-independence of OH. In this chapter, we will search for general trends to distinguish between equilibrium and shock-dominated clouds with the adopted chemical network discussed above, and leave the consideration of the dependence on chemical network to future work.

4.2.2 Heating and Cooling Processes

The chemical reactions strongly depend on the temperature of the gas, and so we follow Gong et al. (2016) by simultanously solving the rate of change of the gas energy per H nucleus, e, given by

$$\frac{de}{dt} = \Gamma - \Lambda, \tag{4.2.17}$$

where Γ and Λ are the total heating and cooling rate per H. The gas temperature is then calculated from the energy with

$$T = \frac{e}{c_v}, \tag{4.2.18}$$

where $c_v = (1/2)k_{\rm B}f$ is the specific heat at constant volume with $f = \sum f_{\rm M} x({\rm M})$ degrees of freedom and $k_{\rm B}$ is the Boltzmann constant. We allow 5 degrees of freedom for H_2 to account for pure rotational states, and assume all other major species are

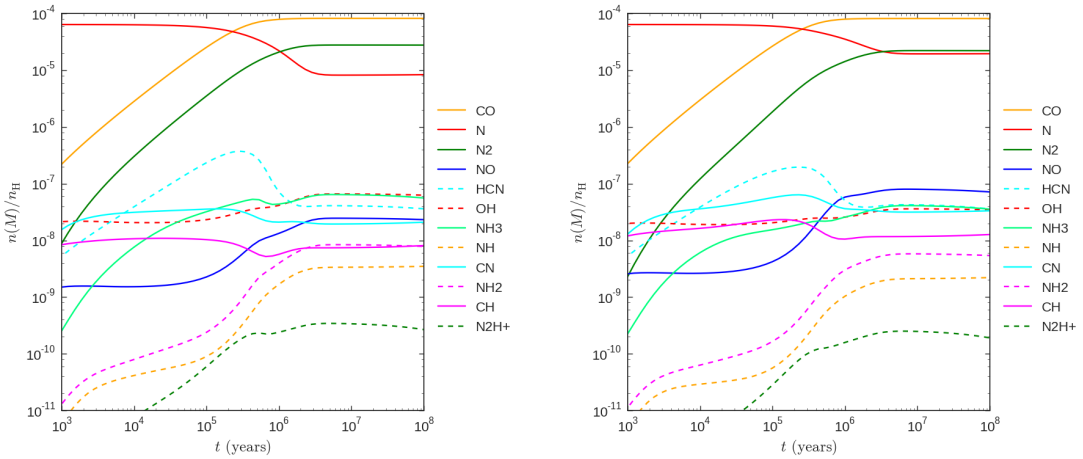

Figure 4.1: Example time-dependent solutions of chemical abundances showing selected species using our chemical network (left) and a modified network (right, see text for details). For this model, $\zeta = 1.3 \times 10^{-17}$ s^{-1} H^{-1}, $\chi = 10$, $A_V = 10$, $n_{\rm H} = 10^4$ cm^{-3}, $N_{\rm H} \sim 1.6 \times 10^{22}$ cm^{-2} and temperature fixed at 10 K.

not excited and so only have 3 translational degrees of freedom. The specific heat we use is then

$$c_v = \frac{3}{2} k_{\rm B} \left(x\left({\rm H}\right) + x\left({\rm H}^+\right) + x\left({\rm He}\right) + x\left({\rm He}^+\right) + x\left(e\right) \right) + \frac{5}{2} k_{\rm B} x\left({\rm H}_2\right). \qquad (4.2.19)$$

In this section we outline the interstellar heating and cooling processes included in our model.

Heating

The main source of heating is from cosmic-ray ionization by electrons. The volume rate of heating from this process is given by

$$\Gamma_{\rm CR} = \zeta q_{\rm CR} n_{\rm H}, \qquad (4.2.20)$$

where ζ is the cosmic-ray ionization rate and $q_{\rm CR}$ is the energy added per primary ionization event. We adopt the formalism of Krumholz (2014b), where the density dependence of $q_{\rm CR}$ in molecular clouds is given by a piecewise fit to the numerical

results of Glassgold et al. (2012):

$$\frac{q_{\rm CR}}{\rm eV} = \begin{cases} 10, & \text{for } \log n_{\rm H} \leq 2, \\ 10 + 3\left(\log n_{\rm H} - 2\right)/2, & \text{for } 2 < \log n_{\rm H} \leq 4, \\ 13 + 4\left(\log n_{\rm H} - 4\right)/3, & \text{for } 4 < \log n_{\rm H} \leq 7, \\ 17 + \left(\log n_{\rm H} - 7\right)/3, & \text{for } 7 < \log n_{\rm H} \leq 10, \\ 18, & \text{for } \log n_{\rm H} > 10, \end{cases} \tag{4.2.21}$$

where $n_{\rm H}$ is expressed in units of $\rm cm^{-3}$.

We include photoelectric heating using the expression of Bakes and Tielens (1994), which gives the volume heating rate as

$$\Gamma_{\rm PE} = 10^{-24} \left(\frac{n_{\rm H}}{\rm cm^{-3}}\right) \epsilon \hat{G}_0 \, \rm erg \, cm^{-3} \, s^{-1}, \tag{4.2.22}$$

where $\hat{G}_0 = \exp\left(-3.02 A_V\right) G_0$ is the dust-attenuated interstellar radiation field in units of Habing. The heating efficiency ϵ is given by

$$\epsilon = \frac{4.87 \times 10^{-2}}{1 + 4 \times 10^{-3} \left(G_0 T^{1/2} / n_e\right)^{0.73}} + \frac{3.65 \times 10^{-2} \left(T/10^4\right)^{0.7}}{1 + 2 \times 10^{-4} \left(G_0 T^{1/2} / n_e\right)}, \tag{4.2.23}$$

where n_e is the electron density.

Cooling

The main source of cooling in molecular gas is through line emission. We use the cooling functions of Neufeld and Kaufman (1993) and Neufeld et al. (1995) for rotational and vibrational cooling by CO, H_2 and H_2O. They give the cooling rate per volume $\Lambda(M) = n(M) n(\rm H_2) L_M$ for a molecule M using a cooling rate coefficient L obtained by fitting to four parameters of the form

$$\frac{1}{L_M} = \frac{1}{L_0} + \frac{n(\rm H_2)}{L_{\rm LTE}} + \frac{1}{L_0} \left(\frac{n(\rm H_2)}{n_{1/2}}\right)^{\alpha} \left(1 - \frac{n_{1/2} L_0}{L_{\rm LTE}}\right). \tag{4.2.24}$$

The parameters L_0, $L_{\rm LTE}$, $n_{1/2}$ and α are tabulated for temperatures up to a few thousand K, and depend on an optical depth parameter $\tilde{N}$. We use the OH rotational line cooling function of Omukai et al. (2010), who provide tabulated parameters using the same formalism of Neufeld and Kaufman (1993). Finally, we use the expression for $\tilde{N}(M)$ given Neufeld and Kaufman (1993) for a volume averaged static sphere of radius r

$$\tilde{N}(M) = \frac{2 n(M) r}{27 \Delta v}, \tag{4.2.25}$$

where we take Δv to be the cloud linewidth.

The molecular cooling functions assume that the coolants are collisionally excitated by H_2. To include collisions by atomic H and by electrons we follow Glover et al. (2010) in replacing $n(H_2)$ in equation (4.2.24) with an effective density $n_{\rm eff}$. For CO rotational cooling, this effective density is

$$n_{\rm eff,CO,rot} = n(H_2) + \frac{\sqrt{2}\sigma_{\rm H}}{\sigma_{H_2}} n(H) + \left(\frac{1.3 \times 10^{-8} \, {\rm cm^3 \, s^{-1}}}{\sigma_{H_2} v_e} \right) n_e, \tag{4.2.26}$$

where $\sigma_H = 2.3 \times 10^{-15}$ cm^2, $\sigma_{H_2} = 3.3 \times 10^{-16} \left(T/1000 \, {\rm K} \right)^{-1/4}$ cm^2 and $v_e = 1.03 \times 10^4 \left(T/{\rm K} \right)^{1/2}$ cm s^{-1}. For H_2O rotational cooling,

$$n_{\rm eff,H_2O,rot} = n(H_2) + 10 n(H) + \left(\frac{k_e}{k_{H_2}} \right) n_e, \tag{4.2.27}$$

where k_e is given by

$$k_e = {\rm dex} \left(-8.020 + 15.749/T^{1/6} - 47.137/T^{1/3} + 76.648/T^{1/2} - 60.191/T^{2/3} \right) \tag{4.2.28}$$

and

$$k_{H_2} = 7.4 \times 10^{-12} T^{1/2} \, {\rm cm^3 \, s^{-1}}. \tag{4.2.29}$$

For CO vibrational cooling

$$n_{\rm eff,CO,vib} = n(H_2) + 50 n(H) + \left(\frac{L_{\rm CO,e}}{L_{\rm CO,0}} \right) n_e, \tag{4.2.30}$$

where

$$L_{\rm CO,e} = 1.03 \times 10^{-10} \left(\frac{T}{300} \right)^{0.938} \exp \left(\frac{-3080}{T} \right), \tag{4.2.31}$$

$$L_{\rm CO,0} = 1.14 \times 10^{-14} \exp \left(\frac{-68}{T^{1/3}} \right) \exp \left(\frac{-3080}{T} \right). \tag{4.2.32}$$

For H_2O vibrational cooling

$$n_{\rm eff,H_2O,vib} = n(H_2) + 10 n(H) + \left(\frac{L_{\rm H_2O,e}}{L_{\rm H_2O,0}} \right) n_e, \tag{4.2.33}$$

where

$$L_{\rm H_2O,e} = 2.6 \times 10^{-6} T^{-1/2} \exp \left(\frac{-2325}{T} \right) \tag{4.2.34}$$

$$L_{\rm H_2O,0} = 0.64 \times 10^{-14} \exp \left(\frac{-47.5}{T^{1/3}} \right) \exp \left(\frac{-2325}{T} \right). \tag{4.2.35}$$

Finally, the effective density for H_2 rotational and vibrational cooling is given by Meijerink and Spaans (2005) as

$$n_{\mathrm{eff,H_2}} = n\left(\mathrm{H_2}\right) + 7n\left(\mathrm{H}\right) + 16n_e. \tag{4.2.36}$$

In addition to molecular cooling, we include cooling from C^+ (at 158 μm) with a volume cooling rate given by Krumholz (2014a)

$$\Lambda\left(\mathrm{C^+}\right) = 6.6 \times 10^{-10} \exp\left(-\frac{91\,\mathrm{K}}{T}\right) x\left(\mathrm{C^+}\right) k_{\mathrm{B}} T \left(\frac{n_{\mathrm{H}}^2}{2}\right), \tag{4.2.37}$$

where $x\left(\mathrm{C^+}\right)$ is the abundance of C^+. We also include the energy lossed by collisions with with grains using the expression of Hollenbach and McKee (1989) for the volume cooling rate

$$\Lambda\left(\mathrm{dust}\right) = 1.2 \times 10^{-31} n_{\mathrm{H}}^2 \left(\frac{T}{1000\,\mathrm{K}}\right)^{1/2} \left(\frac{\mu\mathrm{m}}{s_{\mathrm{min}}}\right)^{1/2} \left(1 - 0.8\exp(-75\,\mathrm{K}/T)\right)\left(T - T_{\mathrm{dust}}\right), \tag{4.2.38}$$

where s_{min} is the minimum size of dust grains and T_{dust} is the dust temperature. Finally, we set an artificial temperature floor in all our models (including shock models) equal to 10 K.

4.3 Shocked Clouds

We extend the two-fluid MHD shock models of chapter 2 to include the heating and cooling processes described above, as well as the expanded chemical network. The details of the models, such as the form of the differential equations and how we solve them, can be found in that chapter. Here we highlight the modifications to the models such as the implementation of ion-neutral chemical reactions. A summary of the parameters for the equilibrium cloud and shock models is shown in table 4.3.

4.3.1 Physical Processes

The shock models inherit the chemical rate coefficients described above, except that the differential equation governing the abundance must be modified as the fluid elements are now advected through a shock front. The continuity equation for each species is

$$\frac{\partial}{\partial t}\left(n(M)\right) + \nabla \cdot \left(n(M)\mathbf{v}\right) = S(M). \tag{4.3.1}$$

Table 4.3: Summary of model parameters

Parameter	Value(s)
Equilibrium Cloud	
Volume density ($n_{\rm H}$)	10^4 cm^{-3}
Column density ($N_{\rm H}$)	8×10^{22} cm^{-2}
Extinction ($A_{\rm V}$)	$\sim$50
ISRF (χ)	10^3
Ionization rate (ζ)	10^{-16}, 10^{-15}, 10^{-14} s^{-1}
Equilibrium temperature ($T_{\rm eq}$)	10, 27, 51 K
Linewidth (Δv)	20 km s^{-1}
Cloud size (L)	5 pc
Dust temperature (T_d)	20 K
Dust size (s)	0.1 μm
Initial He abundance (x(He))	0.1
Initial C abundance (x(C))	8.30×10^{-5}
Initial N abundance (x(N))	6.40×10^{-5}
Initial O abundance (x(O))	1.04×10^{-4}
Initial S abundance (x(S))	8.00×10^{-8}
Initial Fe abundance (x(Fe))	1.50×10^{-9}
Initial Mg abundance (x(Mg))	3.00×10^{-9}
Shock Models	
Shock speed ($v_{\rm s}$)	6, 7, 8 km s^{-1}
Preshock density (n_0)	10^3 cm^{-3}
Magnetic field ($B_{\rm fast}/B_{\rm slow}$)	34 μG/172 μG
Alfvén velocity ($v_{\rm A,fast}/v_{\rm A,slow}$)	2 / 10 km s^{-1}
Preshock temperature (T_0)	11 K
Adiabatic index (γ)	7/5

In a static shock with slab geometry, propagating in the z direction at a velocity v_s into a medium with total hydrogen number density n_0, this reduces to

$$\frac{d}{dz}\left(x(M)\right) = \frac{S(M)}{n_0 v_s}, \tag{4.3.2}$$

where $x(M) = n(M)/n_{\rm H}$ is the abundance of species M. $S(M)$ is given as in the equilibrium cloud models described above.

We use an energy equation for the neutral fluid given by

$$\frac{\partial}{\partial t}\left(\frac{1}{2}\rho v^2 + u + P\right) + \nabla \cdot \left(\left(\frac{1}{2}\rho v^2 + u + P\right)\mathbf{v}\right) = \Gamma - \Lambda, \tag{4.3.3}$$

where ρ is the mass density, v is the fluid velocity in the frame of reference comoving with the shock, P is the gas pressure, u is the internal energy, Γ is the heating rate per volume and Λ is the cooling rate per volume. This reduces, in the static plane-parallel assumption, to

$$v\frac{dP}{dz} + \gamma P\frac{dv}{dz} = (\gamma - 1)\left(\Gamma - \Lambda\right), \tag{4.3.4}$$

where we have assumed that the internal energy is proportional to the pressure

$$u = \frac{P}{\gamma - 1}. \tag{4.3.5}$$

For the present work, we will assume the adiabatic index $\gamma = 7/5$, appropriate for molecular gas at $\sim$1000 K. Heating of the neutral fluid (G_n) and ion fluid (G_i) by ion-neutral collisions is given by

$$G_n^{(in)} = \frac{\alpha\rho_i\rho_n}{\mu_i + \mu_n}\left(3k_{\rm B}\left(T_i - T_n\right) + \mu_i\left|\mathbf{v}_i - \mathbf{v}_n\right|^2\right), \tag{4.3.6}$$

$$G_i^{(in)} = \frac{\alpha\rho_i\rho_n}{\mu_i + \mu_n}\left(3k_{\rm B}\left(T_n - T_i\right) + \mu_n\left|\mathbf{v}_i - \mathbf{v}_n\right|^2\right), \tag{4.3.7}$$

where $\mu_{n,i}$ is the mean mass per neutral ($1.4m_{\rm H}$) or ion. The ion fluid is unable to cool efficiently, and so $G_i^{(in)} = 0$ (Chernoff, 1987), giving an expression for the ion temperature

$$T_i \sim T_n + \frac{\mu_n}{3k_{\rm B}}\left(v_{nz} - v_{iz}\right)^2. \tag{4.3.8}$$

With this approximation, the collisional heating of the neutrals reduces to

$$G_n^{(in)} = \alpha\rho_i\rho_n\left|\mathbf{v}_i - \mathbf{v}_n\right|^2. \tag{4.3.9}$$

We modify the expression for the effective temperature used for ion-neutral reactions (equation (4.2.3)) to include the effect of streaming

$$T_{eff} = \frac{m_n T_i + m_i T_n}{m_n + m_i} + \frac{1}{2}\frac{m_n m_i}{(m_n + m_i)\, k_b} \left(v_{nz} - v_{iz}\right)^2, \tag{4.3.10}$$

where v_{nz} and v_{iz} are the neutral and ion fluid velocities in the shock direction, respectively (Draine, 1980).

For recombination two-body reactions (DR and RR), an effective temperature is unecessary because $m_e \ll m_{n,i}$, so we use the electron temperature. However, the electron temperature only differs from the neutral temperature significantly for stronger shocks ($v_{\rm s} > 10$ km s^{-1} (Chernoff, 1987)). Hence for this work we set the electron temperature equal to the neutral temperature.

For the cooling functions of Neufeld and Kaufman (1993) and Neufeld et al. (1995) we use the optical depth parameter appropriate for a plane-parallel slab of gas

$$\tilde{N}(M) = \frac{n(M)d}{9\Delta v}, \tag{4.3.11}$$

where d is the thickness of the region of the shock with temperatures elevated above the temperature floor, Δv is the change in the neutral velocity across the defined slab, and $n(M)$ is the average density of the coolant M in this region.

4.3.2 CMZ conditions

We will model a typical molecular cloud in the CMZ as a 5 parsec cloud with a total hydrogen number density $n_{\rm H} = 10^4$ cm^{-3}, a linewidth of $\sim$20 km s^{-1} giving a velocity dispersion $\sigma \sim 8$ km s^{-1}, and dust temperature $T_d \sim 20$ K (Ginsburg et al., 2016).

In chapter 3 we showed that in a simulation of a turbulent molecular cloud the most observationally important shocks had velocities $v_s \sim \sigma$. Hence we model shocks with velocities $v_{\rm s} = 6$, 7 and 8 km s^{-1} as representative of turbulence-driven shocks in CMZ clouds. Chapter 3 showed that the typical shock in a turbulent cloud has preshock densities around an order of magnitude lower than the average cloud density. We therefore model shocks with preshock densities $n_0 = 10^3$. The chemical composition and temperature of the preshock gas is obtained by modeling gas at this density as in section 4.2.

Slow shocks are required to have a velocity below the intermediate speed $v_{\rm int} = v_{\rm A} \cos\theta$, where θ is the angle between the magnetic field and shock propagation direction. We choose an Alfvén velocity $v_{\rm A} = 10$ km s^{-1} to allow for 8 km s^{-1} slow shocks propagating at $\theta = 30°$. This corresponds to a magnetic field strength of $\sim$172 μG for preshock density $n_0 = 10^3$ cm^{-3}.

Fast shock velocities are required to be greater than the fast speed, which reduces to $v_{\rm fast} = \sqrt{v_{\rm A}^2 + c_{\rm s}^2}$ when propagating perpendicular to the magnetic field direction. Using the scaling law of Crutcher (1999),

$$B\,(\mu{\rm G}) = b\sqrt{n_{\rm H}\,({\rm cm}^{-3})} \tag{4.3.12}$$

for $b = 1$, we get a magnetic field strength of $\sim$34 μG for preshock density $n_0 = 10^3$ cm^{-3}, and an Alfvén velocity $v_{\rm A} \sim 2$ km s^{-1}. These are strong magnetic fields compared to typical Milky Way molecular clouds of the same density, but there is evidence for up to milligauss strength large scale fields in various locations of the CMZ (e.g. Yusef-Zadeh and Morris, 1987; Bradford et al., 2005). Given the necessary relationships between shock type and magnetic field strength (as discussed in section 2.2.1), detection of shock signatures also indirectly probes the magnetic field. For example, detection of slow shock signatures determines a lower limit to the preshock magnetic field strength, while detection of fast shock signatures determines an upper limit.

An elevated cosmic-ray ionization rate in the CMZ has been put forward to explain high column densities of H_3^+ (Oka et al., 2005; Goto et al., 2008), as well as the high gas temperatures (Yusef-Zadeh et al., 2013b,a). Ginsburg et al. (2016) suggest that heating by this ionization is unable to explain the variation in high temperatures, and consider the dissipation of turbulence as the dominant heat source in the CMZ. We test both hypotheses here by considering a range of ionization rates, ranging from the Milky Way rate of 10^{-16} s^{-1} H^{-1} (Hollenbach et al., 2012) up to the elevated rate of 10^{-14} s^{-1} H^{-1}.

4.3.3 Line-of-sight model

We wish to compare the chemical abundances found in a molecular cloud containing turbulence-driven shocks to one in chemical equilibrium. For a line-of-sight through a cloud of size L, the column density of a species M will be

$$N_{\rm turb}(M) = n(M)L(1-f) + \sum n_i(M)Lf_i, \tag{4.3.13}$$

where $n(M)$ is the number density of M in the equilibrium state, $n_i(M)$ is the number density in some non-equilibrium state such as inside a shock front or post-shock cooling layer, and f_i is the fraction of the line-of-sight in that non-equilibrium state. The total fraction of non-equilibrium gas $f = \sum f_i$, and setting this to zero gives the column density assuming the entire cloud is in equilibrium, $N_{\rm eq}(M)$. A schematic of a line-of-sight through a cloud is shown in Fig. 4.2.

Two non-equilibrium states are considered: inside the hot shock front and in the post-shock cooling layer. We also separately consider fast and slow shocks for

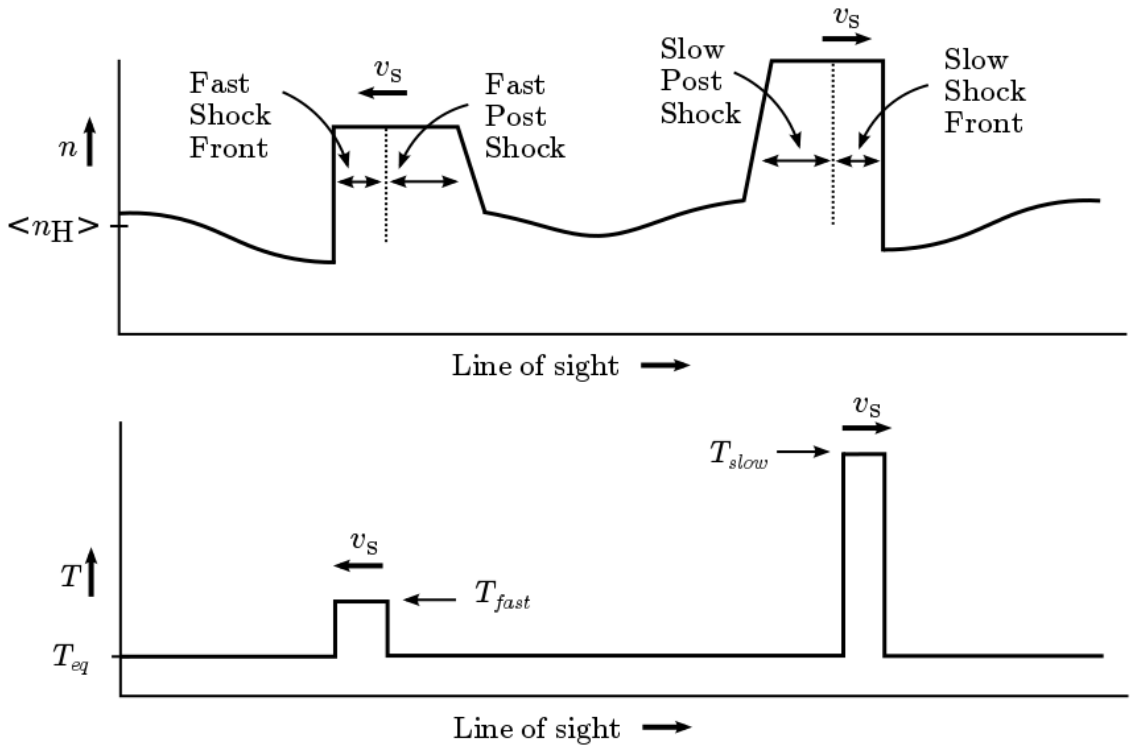

Figure 4.2: Schematic of a line-of-sight through a fast and slow shock. Note that the shock thicknesses are vastly exaggerated—the fraction of gas in shock fronts is ∼0.1%.

each of these states. The hot shock front will be defined as the region in which the temperature is more than the background temperature. The post-shock cooling layer is simply behind this region.

The boundary definitions are illustrated in Figs. 4.3 and 4.4 for a fast and slow shock, respectively. Both profiles shown are for shocks propagating at 8 km s^{-1} into gas with preshock hydrogen density $n_0 = 10^3$ cm^{-3}. The direction of the magnetic field is 89°.9 with respect to the fast shock front normal, and 30° to the slow shock front normal. The fundamental difference between fast and slow shocks is shown in the velocity profile. Fast shocks are driven by magnetic pressure, which drives the ion fluid through the neutrals. Thus the fast shock structure is governed by the long ion-neutral collision timescale. In contrast, slow shocks are driven by gas pressure, which drives the neutral fluid through the ions. Slow shocks are therefore governed by the short neutral-ion collision timescale. The cooling timescale is between the two, and so slow shocks heat up to dramatically higher temperatures ($\gtrsim$2000 K at this velocity) than fast shocks (∼350 K), as seen in the middle panel of Figs. 4.3 and 4.4.

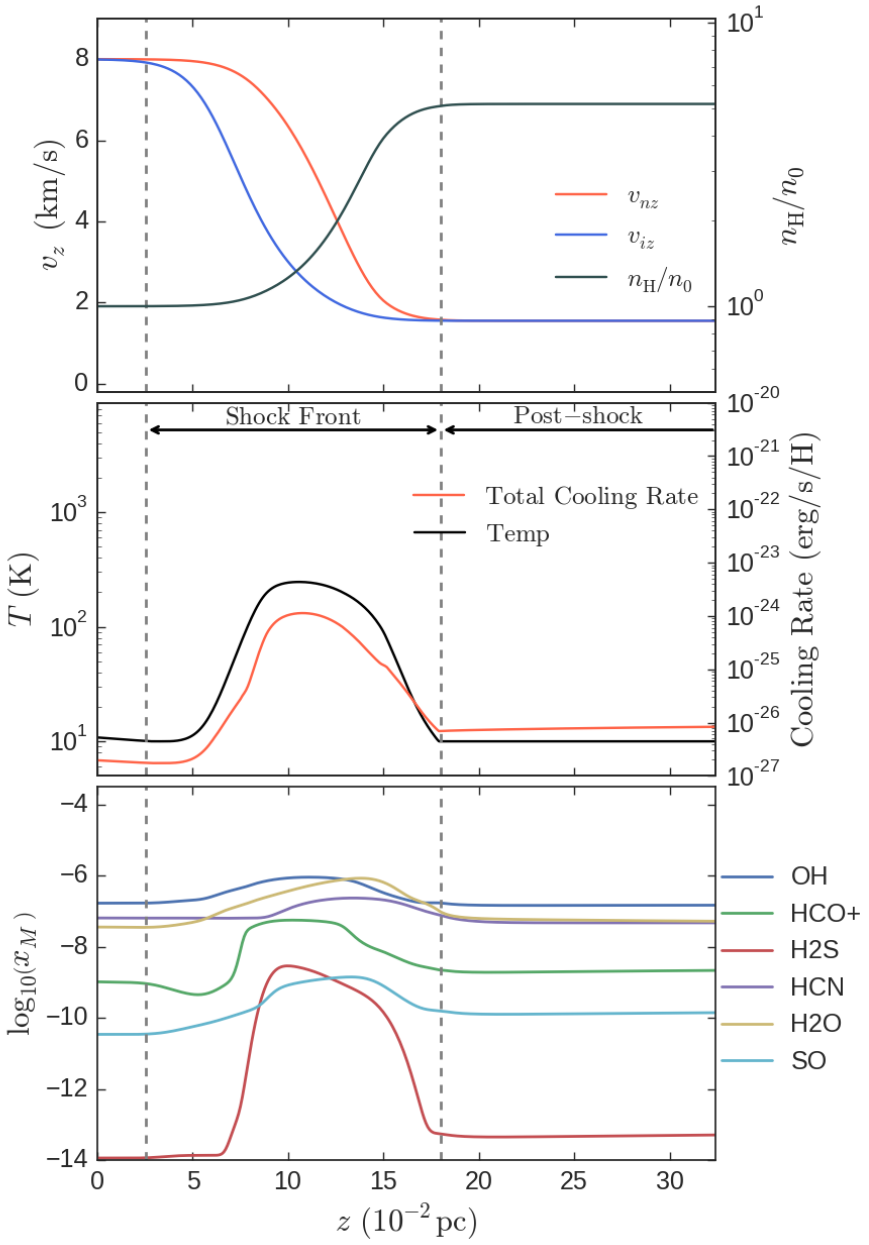

Figure 4.3: Typical fast shock. (Top) Velocity and compression ratio profiles. (Middle) Temperature and cooling rate profiles. (Bottom) Abundances of selected species. Vertical dashed lines define the hot shock front and post-shock zones.

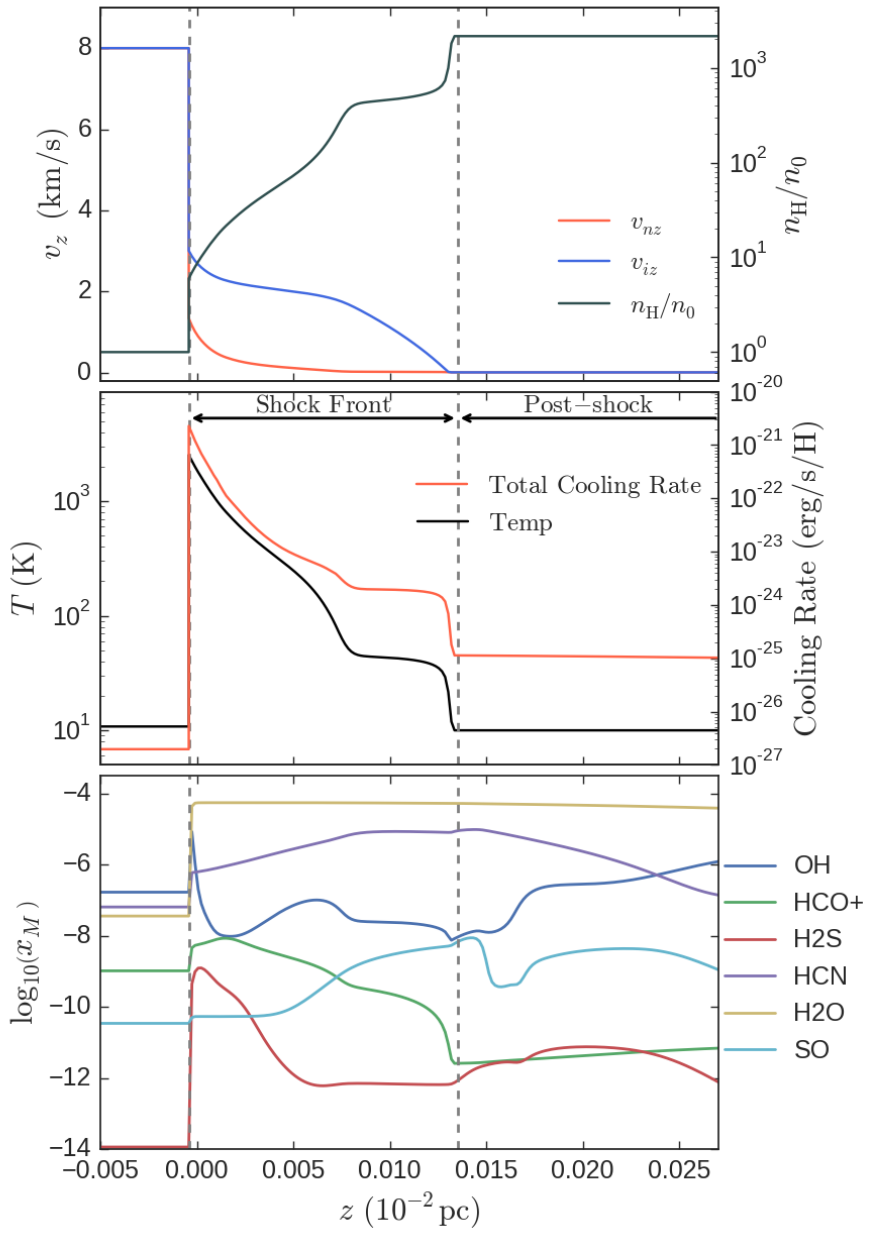

Figure 4.4: Same as Fig. 4.3 except for a typical slow shock.

The vast differences in temperatures reached by fast and slow shocks results in different chemistry driven within and behind the shocks. The chemical abundance profiles of selected species is shown in the lower panel of Figs. 4.3 and 4.4. In fast shocks, most species—such as OH, H_2O and H_2S for example–roughly follow the temperature profile and drop back to preshock abundances. In slow shocks the high temperatures drive chemical changes that persist into the post-shock region. For example, O is quickly converted to OH and then H_2O via the reactions

$$H_2 + O \rightarrow OH + H, \tag{4.3.14}$$

$$H_2 + OH \rightarrow H_2O + H \tag{4.3.15}$$

at temperatures greater than 10^3 K, which increases the H_2O abundance by more than 3 orders of magnitude. HCN is another molecule that maintains its enhancement—due to reactions with CN—into the post-shock region. OH and HCO^+ have complicated abundance profiles that react sensitively to the temperature profile, however in the post-shock region the OH abundance has increased by an order of magnitude above its preshock value whereas HCO^+ drops by 2 orders of magnitude.

4.4 Results

To isolate enhancements of abundances due to shock heating, we compare models of shocked clouds to models with elevated cosmic-ray ionization rates. In Fig. 4.5 we show the abundances of all included species for the equilibrium cloud models with hydrogen density $n_H = 10^4$ cm^{-3} and three ionization rates, $\zeta = 10^{-16}$, 10^{-15} and 10^{-14} s^{-1} H^{-1}. The heating and cooling settles at equilibrium temperatures of ∼19 K, ∼27 and ∼51 K. The elemental ions H^+, He^+, C^+, O^+, S^+ all increase with ionization rate, but N^+ decreases due to rapid reactions with H_2, initiating the formation of nitrogen-hydrides. Our results are similar to the studies of cosmic-ray ionization by Bayet et al. (2011) and Meijerink et al. (2011). They also find that elevated ionization rates cause significant reductions of sulphur-bearing species such as SO, CS and H_2S, and nitrogen-bearing species such as CN, HCN and NH_3. In addition, they also find strong enhancements of ion species such as CH^+, H_2O^+ and OH^+. The sulphur-bearing molecules are reduced because atomic sulphur is increasingly destroyed by charge exchange reactions with H^+. The reduced abundances of HCN and NH_3 are likewise dominated by charge exchange with H^+, but CN destruction is dominated by dissociative recombination with He^+ in the $\zeta = 10^{-14}$ s^{-1} case.

To compute the turbulent column density we consider the total fraction of the line-of-sight in non-equilibrium gas, $f_{\rm tot}$, to be the sum of four fractions

$$f_{\rm tot} = f_{\rm F} + f_{\rm F,pst} + f_{\rm S} + f_{\rm S,pst}, \tag{4.4.1}$$

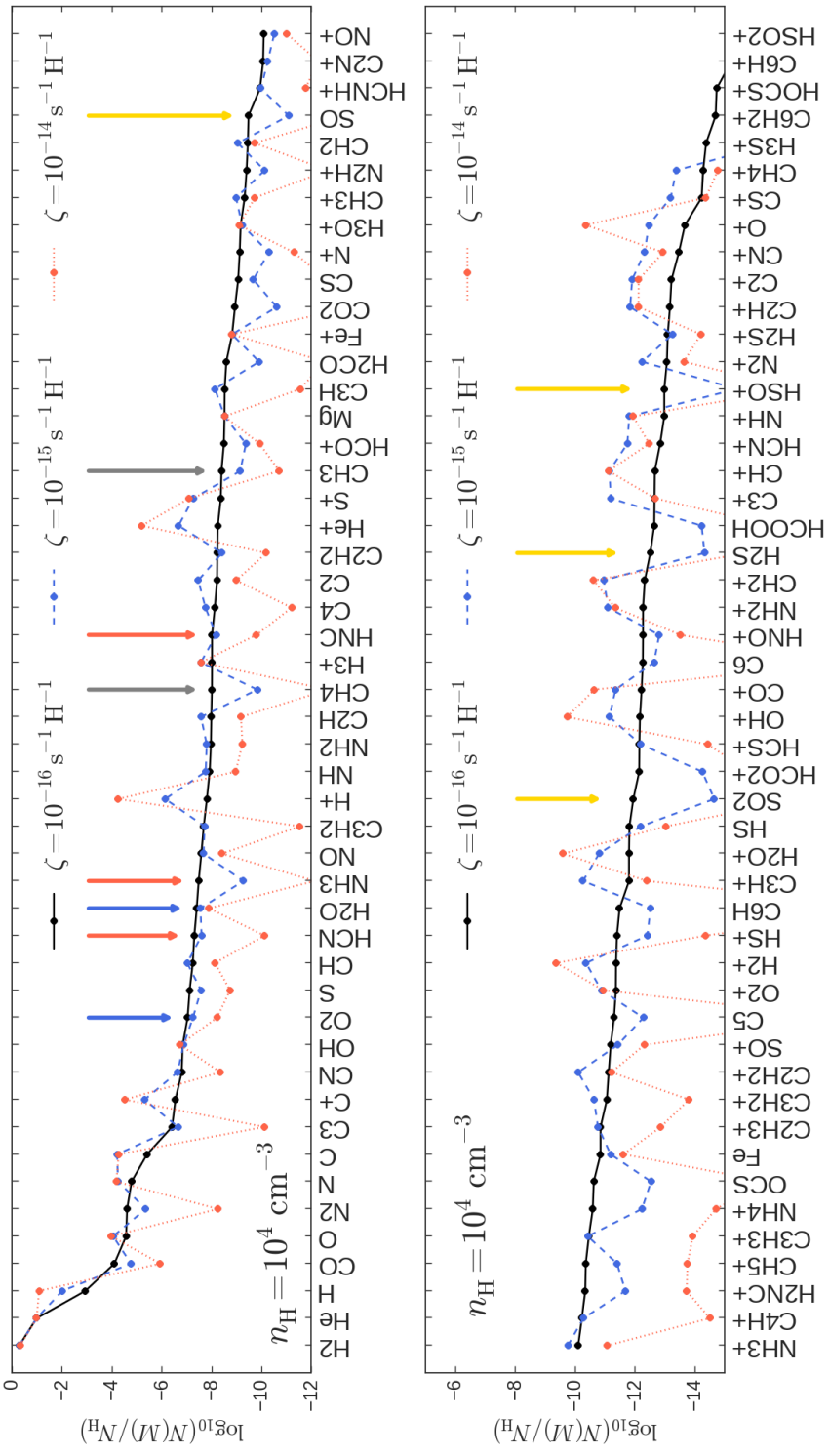

Figure 4.5: Abundances with respect to total hydrogen of all species for equilibrium cloud models with $n_{\rm H} = 10^4$ cm^{-3} and $\zeta = 10^{-16}$ s^{-1} H^{-1} (black solid), $\zeta = 10^{-15}$ s^{-1} H^{-1} (blue dashed) and $\zeta = 10^{-14}$ s^{-1} H^{-1} (red dotted). The coloured arrows indicate interesting species focussed on in the text e.g. oxygen-bearing species (blue arrows), nitrogen-bearing species (red arrows), carbon-bearing species (grey arrows) and sulphur-bearing species (yellow arrows).

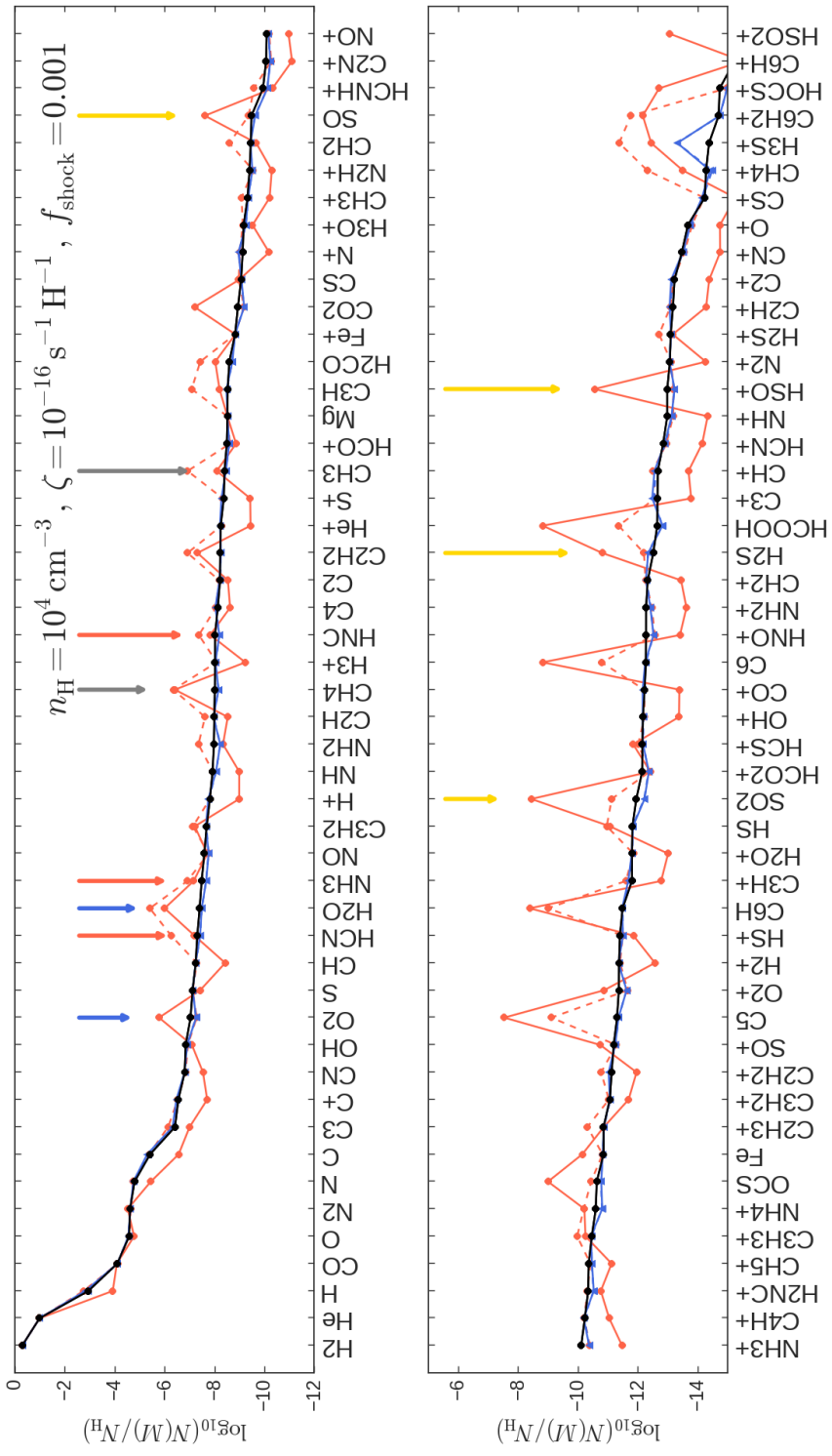

Figure 4.6: Abundances with respect to total hydrogen of all species for the shocked cloud model with $n_{\rm H} = 10^4$ cm^{-3} and $\zeta = 10^{-16}$ s^{-1} H^{-1}. The black solid line indicates the equilibrium model values (as in Fig. 4.5), whereas the blue triangles and red circles refer to turbulent cloud models including exclusively fast shocks and exclusively slow shocks, respectively. In the turbulent cloud models, the fraction of the line-of-sight in shock fronts is 0.1%, and the fraction in post-shock gas is $f_{\rm pst} = 2.4\%$ (solid red) or not included (dashed red). The coloured arrows indicate the same species emphasised in Fig. 4.5.

where $f_{\rm F}$ and $f_{\rm S}$ are the fractions of gas in fast and slow shock fronts, respectively, and $f_{\rm F,pst}$ and $f_{\rm S,pst}$ are the corresponding post-shock states. By modeling molecular cloud turbulent dissipation via C-type fast shocks, Pon et al. (2012) found the volume filling factor of shocked gas to be in the range 0.02–0.5%. From observations of turbulent clouds, Pon et al. (2014, 2016a) found volume filling factors around 0.1%. Finally, in a simulation of a turbulent molecular cloud, chapter 3 found the volume of gas shock heated above 50 K from slow shocks alone to be 0.03%. We thus adopt the line-of-sight fraction of gas inside of shock fronts, $f_{\rm shock} = f_{\rm F} + f_{\rm S} = 0.1\%$. Finally, the fraction of gas in post-shock states is a major uncertainty. Chapter 3 notes, in a cloud simulation, that only $\sim$2.5% of gas was denser than the average post-shock density. So we consider this an upper limit on the total fraction $f_{\rm tot}$.

In Fig. 4.6 we show the abundances of all included species for the shocked cloud models with hydrogen density $n_{\rm H} = 10^4$ cm^{-3} and ionization rates $\zeta = 10^{-16}$ s^{-1} H^{-1}. In this model, line-of-sight fraction in shock fronts $f_{\rm shock} = 0.1\%$ and we consider either no post-shock contribution or $f_{\rm pst} = 2.4\%$. The abundances for the purely fast shock case, $f_{\rm shock} = f_{\rm F}$ (blue dashed line), negligibly differ for the equilibrium cloud abundances except for H_3S^+. In the exclusively slow shock case, the abundances of many species are enhanced and others are depleted, and so we focus on this case.

The oxygen-bearing species—indicated by blue arrows in Figs. 4.5 and 4.6—H_2O and O_2 may be good indicators of shocked chemistry. The abundance of H_2O is enhanced by $\sim$2 orders of magnitude in the hot shock fronts, while O_2 is enhanced by about an order of magnitude in the post-shock regions only. In addition, both species are reduced with increasing cosmic-ray ionization rate, and so these molecular abundances can distinguish between the presence of shocks and an enhanced ionization rate.

The nitrogen-bearing species HCN, HNC and NH_3—indicated by red arrows in Figs. 4.5 and 4.6—are sensitive to shocked regions. These nitrogen species all show about an order of magnitude enhancement in abundance in the hot shock fronts, but are not enhanced when including the post-shock regions. They are each strongly reduced (2–5 orders of magnitude) in the equilibrium models with enhanced ionization rates, suggesting that observations of unusually large abundances of nitrogen-bearing species strongly distinguishes between high ionization rates and the presence of shocks along the line of sight.

Sulphur-bearing species—indicated by yellow arrows in Figs. 4.5 and 4.6—are especially sensitive to shocked regions, with SO, SO_2, H_2S and HSO^+ showing strong enhancements (2–4 orders of magnitude) when the post-shock region is included (red solid line). When only the shock front is included in the line of sight, these species are only slightly enhanced, with SO_2 increased by about an order of magnitude. All four of these species are also strongly reduced in the equilibrium models with enhanced ionization rates, and so avoid that degeneracy along with nitrogen species.

Table 4.4: Summary of selected abundance enhancements

Species	$\log_{10}(x_{\rm eq})^a$	$\log_{10}\frac{x^b_{\rm sh}}{x_{\rm eq}}$	$\log_{10}\frac{x^c_{\rm pst}}{x_{\rm eq}}$	$\log_{10}\frac{x^d_{z14}}{x_{\rm eq}}$
		Oxygen Species		
H_2O	-7.1	2.0	1.4	-0.5
O_2	-6.4	-0.2	1.3	-1.2
		Nitrogen Species		
HCN	-7.2	1.1	0.1	-2.8
HNC	-7.7	0.7	0.2	-1.8
NH_3	-7.5	0.6	0.3	-4.7
		Sulphur Species		
SO	-9.1	0.1	1.9	-3.9
SO_2	-11.3	0.8	3.5	-5.6
H_2S	-12.2	0.3	1.7	-3.2
HSO^+	-12.4	-0.2	2.4	-4.4
		Carbon hydrides		
CH_3	-8.4	1.5	0.3	-2.3
CH_4	-7.8	1.7	1.6	-4.7

[a] Line-of-sight including only equilibrium gas.
[b] Hot slow-shock fronts contribute 0.1% of line-of-sight.
[c] Further 2.4% of line-of-sight from post-shock regions.
[d] Equilibrium gas but for ionization rate $\zeta = 10^{-14}$ H^{-1} s^{-1}.

Finally, the carbon hydrides CH_3 and CH_4 both show strong enhancement, increasing by 2 orders of magnitude in the hot shock fronts. Both of these species remain enhanced over their equilibrium values if post-shock regions are included. In addition, equilibrium abundances of both species strongly decrease with increasing cosmic-ray ionization rate, making their abundance a distinguishing feature between the two models.

These results—summarised in table 4.4—suggest that the chemical signatures of turbulent dissipation in shock waves is to be found in the abundance enhancement, over equilibrium values, of key sulphur- and nitrogen-bearing species as well as carbon hydrides. In appendix B.1, we repeat this analysis with parameters typical to Milky Way clouds. When only the hot shock fronts are included, the chemical abundances negligibly differ from the equilibrium case. This is because at the lower velocity dispersions and shock speeds ($\sim$3 km s^{-1}), the temperatures do not reach high enough values to drive strong chemical changes. However, sulphur-abundances are again sensitive to the inclusion of post-shock regions along the line-of-sight. Hence the strong turbulence in the CMZ is more likely to show observable chemical signatures of turbulent dissipation than clouds in the Milky Way.

4.5 Discussion

We have developed a chemical model of a line-of-sight through shocked turbulent clouds by considering dark cloud chemistry interspersed with a small fraction (0.1%) of hot, shocked gas. The chemical signatures of the shocked regions can be found in the enhanced abundances—compared to equilibrium cloud chemistry—of H_2O, several sulphur-bearing species such as SO, SO_2 and H_2S, as well as the nitrogen-bearing species HCN, HNC and NH_3. The sulphur-bearing species are further enhanced if the abundances of the cold post-shock region remains in a fraction (2.4%) of the line-of-sight before returning to equilibrium abundances. Here we discuss caveats of the model, before providing estimates of rotational line emission from selected molecules.

4.5.1 Caveats

The usual caveats about shock models apply here. The shock temperature, which determines the chemistry, depends on the accuracy of the cooling function. We use molecular cooling functions of Neufeld and Kaufman (1993) and Neufeld et al. (1995), which assume an ortho:para ratio of 3:1 for H_2O and a ratio appropriate for thermal equilibrium for H_2. These ratios do not necessarily hold, and the H_2 ortho:para ratio could be followed if we adopted the full chemical network of Le Gal et al. (2014). Along the same lines, uncertainties in reaction rate coefficients could

be important. We also have not considered the effects of dust grains in this model. Several key species, such as CO, H_2O and O_2, freeze onto dust grain surfaces. Depleting these species not only affects the gas-phase chemistry, it also changes the cooling rates within the shocks and so affects their structure. Properly accounting for this freeze-out, as well as desorption and sputtering within shocks is key to improving the accuracy of the present models.

The model of the line-of-sight is highly simplified. We have assumed a single extinction value for our comparison, unshocked gas. This means there is no edge structure to the cloud. Given that a 0.1% contribution from hot shock fronts can significantly enhance key abundances, it is possible that low extinction chemistry at the edges of a cloud could wash out this signature. We will leave to future work the variation of extinction along the line-of-sight.

Despite these limitations, the models do serve to illustrate that turbulence-driven shocks can produce distinct chemical signatures even if the shock fronts occupy a tiny fraction of the line-of-sight.

4.5.2 Observational prospects

Several key species sensitive to shocked gas—summarised in table 4.4—have been previously observed in the CMZ. For example, Jones et al. (2012) detected emission from SO, HCN and HNC rotational lines in the frequency range ∼85.3–93.2 GHz using the *MOPRA* telescope. Belloche et al. (2013) detect emission in Sgr B2 from HCN, H_2S, SO, SO_2 and OCS in various frequency bands between 80 and 267 GHz using the *IRAM* telescope. Also in Sgr B2, Etxaluze et al. (2013) detected emission from HCN, H_2O, H_2S and NH_2 using the *Herschel* space telescope. By way of example, we estimate the rotational line emission from HCN and HNC and compare to the results of Jones et al. (2012).

We use the non local thermodynamic equilibrium radiative transfer code, RADEX (van der Tak et al., 2007), to estimate molecular line emission. For a given radiating molecule, RADEX requires as input the density of H_2 as the collisional partner, the column density of the radiating molecule, the temperature and the linewidth.

For the shock front region of the fast shock shown in Fig. 4.3, the density-weighted average temperature is 92 K, the average H_2 density is 1.0×10^3 cm^{-3} and the neutral velocity changes by 6.4 km s^{-1}. The column densities of HNC and HCN in this slab are 5.3×10^{13} and 1.5×10^{14} cm^{-2}, respectively. For the slow shock shown in Fig. 4.4, the density-weighted average temperature is 66 K, the average H_2 density is 1.4×10^5 cm^{-3}. The column densities of HNC and HCN in this slab are 7.0×10^{13} and 8.9×10^{14} cm^{-2}, respectively. For the comparison unshocked cloud, we use the abundances from the $\zeta = 10^{-16}$ H^{-1} s^{-1} case and assume a depth of 5 pc. The temperature is 10 K, H_2 density is 5.0×10^3 cm^{-3} and the linewidth is 20 km s^{-1}. The column densities of HNC and HCN in this cloud are 1.5×10^{14}

and 7.5×10^{14} cm^{-2}, respectively. We found negligible emission was produced in the cases of elevated cosmic-ray ionization rates due to the strong reduction in their abundances, so we ignore those cases.

With the above parameters, the low-lying rotational lines of HNC and HCN computed using RADEX are shown in Fig. 4.7. For both species, at any upper J, emission originating from a single slow shock is the strongest, followed by emission from the 5 pc cloud and then from a single fast shock. Jones et al. (2012) measured the 1–0 transitions of both species and measured average line fluxes of HNC in the range 30-76 K km s^{-1} and HCN in the range 100-199 K km s^{-1} for various regions in the CMZ. The slow shock emission is within these ranges for both HNC and HCN. In contrast, the 5 pc ambient cloud model underpredicts the emission from both species. The line ratio HNC 1–0 / HCN 1–0 was measured by Jones et al. between 0.22 and 0.38 in different regions of the CMZ. In the slow shock this ratio is 0.22 and in the ambient cloud it is 0.52. The measured ratio therefore favours the slow shock prediction.

Another distinguishing feature would be line ratios of different transitions from the same molecule. For example, HCN 2–1/1–0 is $\sim$1 for the slow shock, but is 0.3 for the 5 pc cloud model. Optical depth effects could create uncertainty for these lines, so observations of higher J lines would reduce ambiguity. The 8–7 to 10–9 lines of HCN have been observed in the CMZ cloud Sgr B2 by the *Herschel Space Telescope* (Etxaluze et al., 2013). We will analyse these lines in future.

RADEX is also able to compute rotational line emission from para- and ortho-NH_3 and para- and ortho-H_2S. Both NH_3 and H_2S are enhanced in the shock models, but we do not follow their ortho-to-para ratios. NH_3 has been extensively observed in the CMZ at elevated temperatures (Mills and Morris, 2013; Ott et al., 2014). We leave analysis of these species to future work.

In this section we have provided observational predictions for turbulent dissipation in shock waves in the form of rotational line emission for HNC and HCN. Previous observations of emission from these molecules in CMZ clouds is roughly consistent with clouds containing slow MHD shocks.

4.6 Conclusion

In order to find direct signatures of the dissipation of turbulence in the CMZ, we have extended the MHD shock models of chapter 2 with an updated chemical network and new cooling and heating functions. Fast and slow shocks with velocities $v_s = 6$–8 km s^{-1} were computed for preshock conditions appropriate to the CMZ. A model was developed of a line-of-sight through turbulent molecular clouds comprising gas in ambient unshocked regions, hot shock fronts and post-shock cooling layers. The unshocked region was modeled as a time-dependent photodissociation region. The

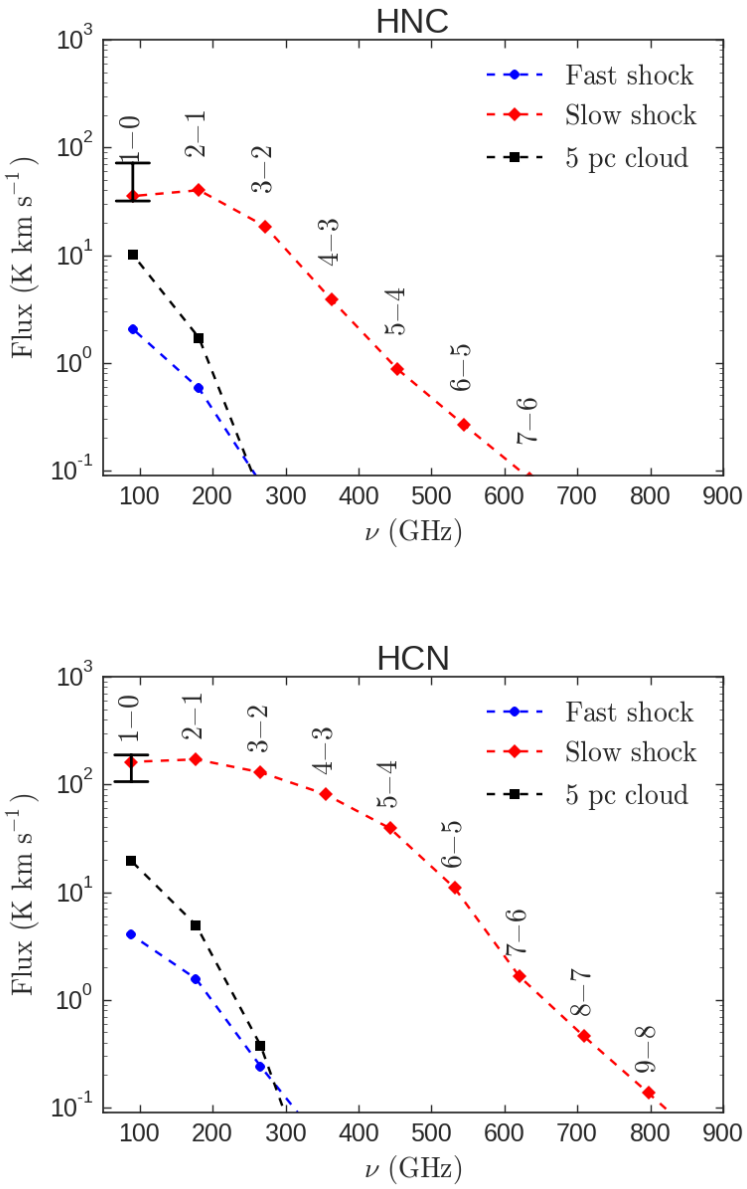

Figure 4.7: Integrated line fluxes of HNC (upper) and HCN (lower). In each panel, emission is shown for the fast shock in Fig. 4.3 (blue circles), the slow shock in Fig. 4.4 (red diamonds) and the unshocked cloud (black squares). The vertical bar at the 1–0 transitions indicate the range of average values from various regions in the CMZ (Jones et al., 2012).

average chemical abundances of several species, namely H_2O, HCN, HNC, NH_3, CH_3, CH_4, SO_2 and H_2S, were enhanced by 1–2 orders of magnitude above unshocked values even when the hot shock fronts contribute only 0.1% of the line-of-sight.

The radiative transfer code RADEX was used to compute the emission from rotational lines of HCN and HNC. Recent observations of lines from these species in CMZ clouds were shown to be broadly consistent with the presence of shocks. This provides direct evidence for the dissipation of turbulence via shock waves, further supporting the hypothesis that turbulence is the main driver of widespread elevated temperatures in CMZ clouds.

Chapter 5

Two-fluid dusty shocks

Abstract

Dust plays a key role in the thermodynamics and evolution of the interstellar medium. In protoplanetary discs, pressure gradients decouple the dust from the gas. The subsequent drag significantly impacts the early evolution of planetary systems, and has proven numerically challenging to model. We provide simple benchmarking problems for dusty gas codes by numerically solving the two-fluid dust-gas equations for steady, plane-parallel shock waves. We show that there are two distinct shock solutions to these equations, analogous to C- and J-type magnetohydrodynamic shocks. These solutions can be used to test the implementation of drag in numerical codes seeking to simulate dust and gas. We also provide an application of J-type dust-gas shocks to studying the structure of accretion shocks onto protoplanetary discs. We find that two-fluid effects are most important for grains larger than 1 μm, and that dust emission from the accretion shock is senstive to the dust-to-gas ratio of the infalling material.

5.1 Introduction

Dust plays a key role in numerous astrophysical evironments. In the interstellar medium (ISM), dust is heavily involved in controlling the thermodynamics by being a major coolant, collisional partner and source of opacity. It allows us to probe the magnetic field by measuring the polarization in thermal dust emission (Planck Collaboration et al., 2016a), and is crucial to the formation of H_2 in molecular clouds by providing a catalytic surface and by attenuating the dissociating ultraviolet radiation field (Glover and Clark, 2012). Thermal dust emission is observed with telescopes such as Spitzer (e.g. Stephens et al., 2014), Herschel (e.g. Launhardt et al., 2013), and ALMA (e.g. ALMA Partnership et al., 2015), and these observations are used to obtain properties of the gas. Thus it is crucially important not only to understand the properties of dust grains, but also their coupled evolution with the gas phase in order to rigorously relate dust emission to properties of the ISM. In protoplanetary discs, the radial pressure gradient causes gas to flow at below the Keplerian velocity. The pressureless dust component rotates at the Keplerian velocity, so the two fluids drift with respect to each other and accurate modeling requires a careful treatment of the drag.

The importance of coupled gas-dust modelling has motivated the development of numerical codes designed to simulate gas and dust in various astrophysical systems. For example, radial gradients of gas pressure in protoplanetary discs induce dust clumping leading to planetesimal formation (Bai and Stone, 2010a), large dust-to-gas variations occur in turbulent molecular clouds and dust filaments do not necessarily correlate with gas filaments (Hopkins and Lee, 2016), and dust-gaps are cleared more easily than gas-gaps in protoplanetary discs (Paardekooper and Mellema, 2006b). Both grid-based (Johansen et al., 2006; Bai and Stone, 2010b) and particle-based smoothed particle hydrodynamics codes (Laibe and Price, 2012a; Lorén-Aguilar and Bate, 2014) have been used to study dusty gas flows in the ISM. However, Laibe and Price (2011) highlight a lack of simple analytic solutions to benchmark dusty gas codes in astrophysical conditions. The main goal of this work is to provide such a simple solution by computing the structure of steady-state, planar two-fluid dusty gas shock waves. Unlike the standard shock-tube tests, steady shocks comprise only one hydrodynamic component with a structure that can be computed by simply integrating the governing ordinary differential equations, as we do in section 5.3. The numerical simulation is also simple: drive a piston represented by reflective boundary conditions into a uniform medium. This simple test can be used to benchmark how numerical codes behave with different dust-to-gas ratios, or e.g. linear, quadratic, or Epstein forms of the drag coefficients.

Two-fluid dusty shocks are not just ideal benchmarks for numerical codes. Supersonic flows occur ubiquitously in astrophysical systems. For example, in the

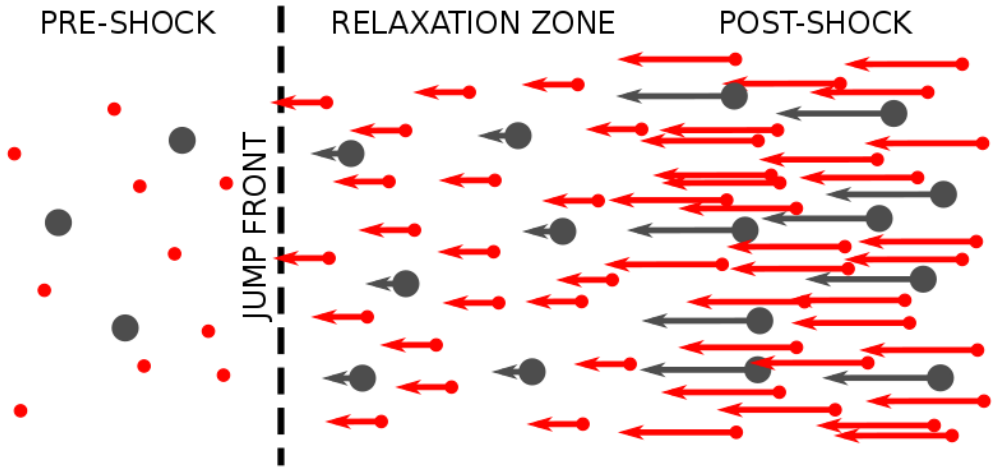

Figure 5.1: Sketch of a J-type dust-gas two-fluid shock in the frame of reference where the preshock fluid is stationary. The red, smaller circles refer to gas particles whereas the larger black circles refer to dust particles. The black dashed line marks the jump transition in the gas fluid that takes place on the order of a few mean free paths.

inside-out collapse model of protostellar cores, material becomes thermally unsupported and free-falls onto the protoplanetary disc at a few km/s. The sound speed in the gas is only ∼0.2 km/s, and so a shock wave forms as the material decelerates to settle onto the disc. In section 5.4 we provide an application of our two-fluid shock solutions to study this type of accretion shock.

5.2 Theory

In this section we outline the set of equations that describe the two-fluid dust-gas system. We use these equations to derive the dispersion relation for linear waves in the combined fluid, and discuss how this affects the possible dust-gas shock structures. We characterise the initial stationary states to outline the criteria for J- and C-type shocks to occur and discuss their structure.

5.2.1 Fluid Equations

For a fluid with gas density ρ, velocity $\mathbf{v}$ and pressure P the equations of continuity and conservation of momentum can be written

$$\frac{\partial \rho}{\partial t} + \nabla \cdot (\rho \mathbf{v}) = 0, \tag{5.2.1}$$

$$\rho \frac{\partial \mathbf{v}}{\partial t} + \rho \left(\mathbf{v} \cdot \nabla\right) \mathbf{v} = -\nabla P - \mathbf{F}_{\text{drag}}, \tag{5.2.2}$$

where $\mathbf{F}_{\rm drag}$ is the rate at which momentum is added to the gas via drag from the dust fluid. The energy equation can be written

$$\frac{\partial}{\partial t}\left(\frac{1}{2}\rho v^2 + u + P\right) + \nabla \cdot \left(\left(\frac{1}{2}\rho v^2 + u + P\right)\mathbf{v}\right) = \Gamma - \Lambda, \tag{5.2.3}$$

where u is the internal energy per unit volume, Γ is the heating rate per volume and Λ is the cooling rate per volume. The analogous equations for the coextensive dust fluid with density ρ_d and velocity $\mathbf{v}_d$ are

$$\frac{\partial \rho_d}{\partial t} + \nabla \cdot (\rho_d \mathbf{v}_d) = 0, \tag{5.2.4}$$

$$\rho_d \frac{\partial \mathbf{v}_d}{\partial t} + \rho_d \left(\mathbf{v}_d \cdot \nabla\right)\mathbf{v}_d = \mathbf{F}_{\rm drag}, \tag{5.2.5}$$

where we have assumed the dust to be pressureless. Finally, we use the ideal equation of state

$$P = \frac{\rho k_B T}{\mu}, \tag{5.2.6}$$

where μ is the mean mass per gas particle, T is the gas temperature and k_B is the Boltzmann constant.

In section 5.4, we introduce heating and cooling functions appropriate to astrophysical applications so that the gas temperature varies. Here, for the purposes of computing simple benchmarking problems, we assume the gas is isothermal so that equation (5.2.3) is ignored, and the ideal gas law becomes

$$P = \rho c_s^2, \tag{5.2.7}$$

where c_s is the isothermal sound speed.

The form of the drag term has been thoroughly discussed by Laibe and Price (2012b) for various regimes of astrophysical interest. It is generally proportional to a power law of the drift velocity between the two fluids. If we consider the linear drag regime, the drag term on the total fluid can be written as

$$\mathbf{F}_{\rm drag} = K\left(\mathbf{v} - \mathbf{v}_d\right) \tag{5.2.8}$$

for drag coefficient K. A linear analysis gives the dispersion relation for waves with angular frequency ω and wavenumber k

$$\left(\omega^2 - k^2 c_s^2\right) + \frac{i}{\omega \tau_s}\left(\omega^2 - k^2 \tilde{c}_s^2\right) = 0, \tag{5.2.9}$$

where

$$\tau_s = \frac{\rho_0 \rho_{d0}}{K\left(\rho_0 + \rho_{d0}\right)}$$

is the drag stopping time—the characteristic time to damp the differential velocity between the dust and gas fluids—for unperturbed gas and dust density ρ_0 and ρ_{d0}, respectively. The combined fluid sound speed

$$\tilde{c}_s = c_s \left(1 + D\right)^{-1/2}, \tag{5.2.10}$$

with the dust-to-gas ratio

$$D = \frac{\rho_{d0}}{\rho_0}. \tag{5.2.11}$$

In the limit of weak coupling between the dust and gas ($K \to 0$, $\tau_s \to \infty$) we recover the dispersion relation for ordinary sound waves in a gas with phase velocity $\omega/k = c_s$. In the strong coupling limit ($K \to \infty$, $\tau_s \to 0$) the second term of equation (5.2.9) dominates, and so waves travel at the combined sound speed $\tilde{c}_s$.

The two signal speeds in the system, c_s and $\tilde{c}_s$, determine the possible structures of dust-gas shocks. The dust-gas mixture will behave as a single fluid far ahead and behind a shock and so the combined sound speed $\tilde{c}_s$ is the relevant signal speed that, in the frame of reference comoving with the shock, the fluid velocity must transition across. As $\tilde{c}_s$ is necessarily less than c_s, we will see that two distinct classes of shocks arise depending on whether the shock speed is greater or less than the gas signal speed c_s.

For a supersonic shock (shock velocity $v_s > c_s$) the preshock fluid is overrun by high density gas in a thin shock front a few mean free paths wide that resembles an ordinary gas dynamic shock. The dust particles cannot respond quickly, and so there is a relaxation zone wherein the dust particles are accelerated until the two fluids flow at the same velocity. This structure is qualitatively sketched in Fig. 5.1.

When the shock speed is between the two signal speeds, sound waves in the gas fluid can travel ahead of the shock front and compress the gas and dust in such a way that all the fluid variables remain continuous through the shock. We will call these two classes J-type and C-type shocks in analogy to the kinds of magnetised two-fluid shocks outlined by Draine (1986), where ion-magnetosonic waves can travel ahead of a jump front to form a "magnetic precursor". In the next section we will characterise these classes in further detail.

5.2.2 Shock Classification

Assuming a steady state, one-dimensional structure varying in the z-direction and a power law drag term with index β, the gas fluid equations (5.2.1) and (5.2.2) in

the frame of reference comoving with the shock reduce to

$$\frac{d}{dz}(\rho v) = 0, \tag{5.2.12}$$

$$\frac{d}{dz}\left(\rho v^2 + P\right) = K\left|v_d - v\right|^{\beta}, \tag{5.2.13}$$

and the dust fluid equations (5.2.4) and (5.2.5) reduce to

$$\frac{d}{dz}(\rho_d v_d) = 0, \tag{5.2.14}$$

$$\frac{d}{dz}\left(\rho_d v_d^2\right) = -K\left|v_d - v\right|^{\beta}. \tag{5.2.15}$$

The pre-shock state, defined by the gas density ρ_0, dust density ρ_{d0}, shock velocity v_s and initial pressure P_0 is a stationary point. In order to classify this state, we perturb the initial state and let the perturbation grow (or decay) exponentially as follows:

$$v = v_s + \delta v e^{\lambda z}, \tag{5.2.16}$$

$$v_d = v_s + \delta v_d e^{\lambda z}, \tag{5.2.17}$$

$$\rho = \rho_0 + \delta\rho e^{\lambda z}, \tag{5.2.18}$$

$$\rho_d = \rho_{d0} + \delta\rho_d e^{\lambda z}, \tag{5.2.19}$$

$$P = P_0 + \delta P e^{\lambda z} = \rho_0 c_s^2 + c_s^2 \delta\rho e^{\lambda z}. \tag{5.2.20}$$

Substituting these perturbed variables back into Equations (5.2.12) to (5.2.15), assuming linear drag ($\beta = 1$), ignoring terms of second order in perturbations and solving for λ gives the eigenvalue

$$\lambda = -\frac{K}{\rho_{d0} v_s}\frac{1+D}{D}\frac{v_s^2 - \tilde{c}_s^2}{v_s^2 - c_s^2}. \tag{5.2.21}$$

This expression implies that for supersonic shocks ($v_s > c_s > \tilde{c}_s$), the eigenvalue $\lambda < 0$ and hence the perturbation decays. That is, the initial state is a stable stationary point. Hence it requires an initial discontinuity (jump) to get across the sound speed. In this kind of shock, the gas fluid is highly compressed over a few mean free paths. The dust cannot respond quickly, and so this jump is determined by the hydrodynamic jump conditions.

By replacing v_s with the post-shock solution v_{post} we can explore the final state. A shock in the total gas-dust fluid is a transition across the total speed $\tilde{c}_s$, and so $v_{\text{post}} < \tilde{c}_s$. Thus the eigenvalue near the post-shock state $\lambda < 0$, which defines a stable point, so jumping near this state will settle onto it. Two-fluid dust-gas J-type

shocks were first discussed by Carrier (1958), and have been thoroughly studied for various non-astrophysical applications (see review by Igra and Ben-Dor, 1988, and references therein).

For C-type shock solutions to exist we require a positive eigenvalue in equation (5.2.21), so that perturbations smoothly grow away from the preshock state. The shock speed must then be in the range

$$\tilde{c}_s < v_s < c_s \tag{5.2.22}$$

and hence the Mach number is necessarily below unity for this type of shock. Without cooling, this shock will smoothly settle onto the post-shock state. However, with cooling there is the potential for the gas sound speed to drop (as the gas compresses in the shock) faster than the velocity. If $c_s = v$ in the shock somewhere, a jump will be required. Otherwise, the fluid variables will remain continuous throughout the shock. This kind of shock was first investigated by Kriebel (1964) and further developed by Miura (1972). In the next section, we discuss how these two kinds of shocks could be used to benchmark dusty gas numerical codes.

5.3 Benchmark Problems

In this section we describe the first order differential equation that we solve to investigate the structure of two-fluid dust-gas shocks. These isothermal shock solutions are ideal tests for benchmarking numerical codes that wish to simulate dusty gas. Our PYTHON code that returns the shock solutions described in this section is publicly available on the Python Package Index[1] and BitBucket[2].

In the standard shock-tube problem (Sod, 1978) the simple setup breaks up into a shock wave, rarefaction wave and a contact discontinuity. In the two-fluid dust-gas version of this problem there is no known analytic solution, but Saito et al. (2003) find that a steady-state shock solution fits one of the components well. Unlike the Sod shock-tube, the steady shocks we compute here are very simple, comprising just one hydrodynamic structure. A numerical code can then be tested against the steady solution by setting up a reflective boundary representing a piston as the driver of the shock, as in Toth (1994).

[1] https://pypi.python.org/pypi/DustyShock
[2] https://bitbucket.org/AndrewLehmann/dustyshock

5.3.1 Numerical Integration

We get the dimensionless derivative of the dust velocity from combining equations (5.2.14) and (5.2.15):

$$\frac{dw_d}{d\xi} = -\left|w_d - w\right|^{\beta} \tag{5.3.1}$$

for the normalised velocities and position defined by

$$w_d = \frac{v_d}{v_s}, \tag{5.3.2}$$

$$w = \frac{v}{v_s}, \tag{5.3.3}$$

$$\xi = \frac{K}{\rho_{d0} v_s^{2-\beta}} z, \tag{5.3.4}$$

where v_s is the shock velocity and ρ_{d0} is the preshock dust mass density. Combining equations (5.2.13) and (5.2.15), and making use of isothermality, gives

$$\frac{d}{dz}\left(\rho v^2 + \rho c_s^2 + \rho_d v_d^2\right) = 0, \tag{5.3.5}$$

which states that the sum of the gas and dust ram pressures and the thermal pressure is conserved through the shock. The sum of pressures at any point in the shock retains the preshock value, so that

$$\rho v^2 + \rho c_s^2 + \rho_d v_d^2 = \rho_0 v_s^2 + \rho_0 c_s^2 + \rho_{d0} v_s^2. \tag{5.3.6}$$

From this equation, we derive a quadratic equation in the gas velocity

$$w^2 + \left[D\left(w_d - 1\right) - 1 - \mathcal{M}^{-2}\right] w + \mathcal{M}^{-2} = 0, \tag{5.3.7}$$

where we have used the sonic Mach number $\mathcal{M} \equiv v_s/c_s$, assuming that initially the gas and dust flow together at the shock velocity v_s. The two roots of the quadratic represent supersonic and subsonic (with regards to c_s) gas velocities, and closes equation (5.3.1).

The fluid variables defining the shock structure are obtained by integrating the first order ordinary differential equation (ODE) defined by equation (5.3.1). In this paper we use the open source PYTHON module *scikits.odes*[3]. This module solves initial value problems for ODEs using variable-order, variable-step, multistep methods.

[3]https://github.com/bmcage/odes

J-type shock solutions

For J-type shocks, the preshock fluid is in a stable stationary state with gas fluid velocity equal to the supersonic root of equation (5.3.7). As discussed in section 5.2.2, a hydrodynamic jump in the gas fluid is required to cross the sound speed c_s. For the isothermal shocks computed here, the density immediately jumps from ρ_0 to

$$\rho_j = \mathcal{M}^2 \rho_0. \tag{5.3.8}$$

The velocity switches from the supersonic to the subsonic root of equation (5.3.7). Integration of equation (5.3.1) then gives the post-jump structure.

An example of the velocity structure of an isothermal J-type shock in the frame of reference comoving with the shock is shown in Fig. 5.2. The upper panel shows shock structures computed with Mach number $\mathcal{M} = 2.0$ using a linear drag term ($\beta = 1$) and initial dust-to-gas ratios varying from 0.01–1. After the initial hydrodynamic jump in the gas, the dust lags behind the gas, but both eventually settle to the same velocity (below $\tilde{c}_s$). The combined fluid velocities far ahead (v_s) and behind (v_2) the shock front are related by

$$\frac{v_2}{v_s} = \left(\frac{\tilde{c_s}}{v_s}\right)^2 = (1+D)^{-1}\,\mathcal{M}^{-2}. \tag{5.3.9}$$

Hence reducing D changes the shock structure by increasing the post-shock velocity that the solution settles to. This effect allows this steady state solution to test how a numerical code behaves with different dust-to-gas ratios.

The lower panel of Fig. 5.2 shows isothermal shock solutions with the same conditions as the upper panel except that they are computed using a quadratic drag term

$$F_{\text{drag}} = K\,|v - v_d|^2\,. \tag{5.3.10}$$

The structure is qualitatively similar to the linear drag case, however the shock thickness is an order of magntitude larger (in the dimensionless position variable ξ). From equation (5.3.1) the shock thickness

$$\Delta\xi \sim (\Delta w)^{1-\beta}\,. \tag{5.3.11}$$

Δw is necessarily between 0 and 1, and so the shock thickness increases with the index of the power-law drag. For this reason, the solution with quadratic drag has an extended tail of very small but finite Δw. In real units, however, the shock thickness

$$\Delta z = \frac{\rho_{d0} v_s^{2-\beta}}{K}\,|\Delta w|^{1-\beta}\,. \tag{5.3.12}$$

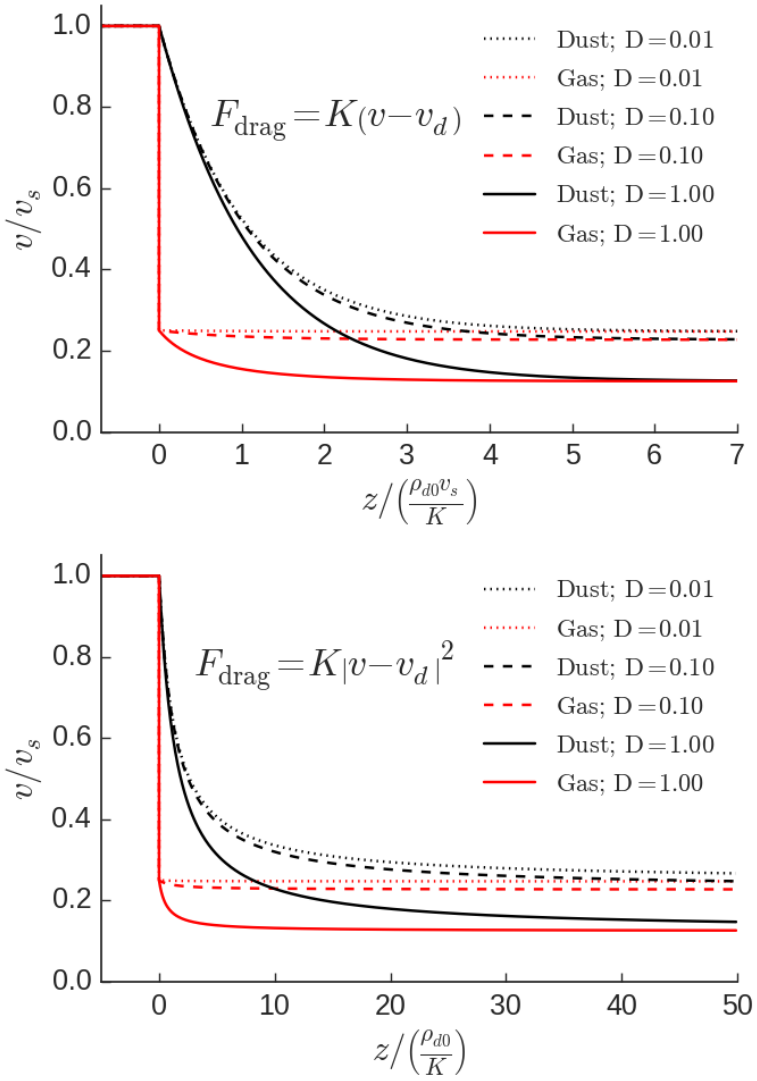

Figure 5.2: J-type gas-dust shocks with Mach number $\mathcal{M} = 2$ and initial dust-to-gas ratios $D = 1$ (solid lines), $D = 0.1$ (dashed lines) and $D = 0.01$ (dotted lines). The red lines give the gas velocity and the black lines gives the dust velocity, both normalised to the shock velocity. The upper panel are solutions computed with a linear drag term while the lower panel uses a quadratic drag term. Note that the z-scale normalisation differs according to equation (5.3.4).

If the same value of K and ρ_{d0} is used in the different drag cases, the size of the shock in the linear regime ($\beta = 1$) is larger than the shock in the quadratic regime ($\beta = 2$) by the factor $v_s|\Delta w|$. For astrophysical shocks of the order of a few km s^{-1}, this means shocks with linear drag will be $\sim 10^4$ times larger than shocks with quadratic drag. Note that the drag coefficient K has different dimensions in the different drag regimes.

These stark differences allow a numerical code's implementation of different drag coefficients to be tested by the shock problem. Note that regardless of the form of the drag term, the shock solution settles onto the same post-shock velocity. This is because the jump conditions relate the velocities of the *combined* fluid on either side of the shock.

The different shock structures resulting from different drag terms could be used to test a numerical code's implementation of the drag. However, in many codes artificial viscosity is used to smear a discontinuity over a finite distance. The scaling factor in equation (5.3.12) can be adjusted until the relaxation tail of the J-type analytic shock solution spreads over many computational cells, so that the behaviour of a numerical code in certain regimes of the drag coefficient (small K) and/or dust density (large ρ_{d0}) can be tested. The C-type shock solution in the following section avoids this limitation because it lacks any discontinuity. The structure also depends on the dust-gas interaction more crucially than in J-type shocks, and may therefore be a more appropriate test problem for dusty gas numerical codes.

C-type shock solutions

C-type shocks are necessarily subsonic, and so the shock structure can be obtained by integrating equation (5.3.1) using the subsonic root of equation (5.3.7).

An example of the velocity structure of isothermal C-type shocks is shown in Fig. 5.3 using a linear drag term ($\beta = 1$). The pre-shock variables are the same as for the J-type shock discussed above, except that the Mach number $\mathcal{M} = 0.95$. Sound waves in the gas fluid stream ahead of the shock and gradually compress the preshock medium. As the two fluids smoothly settle onto the post-shock state the drift velocity remains small compared to the drift velocities reached in the J-type shocks. When computed with a quadratic drag term ($\beta = 2$, lower panel), the structure is an order of magnitude wider (in the dimensionless variable ξ) than in the linear case, explained by equation (5.3.11). Similarly to the J-type shock with quadratic drag, there is an extended tail of very small but finite Δw.

Recall that the shock velocity v_s for C-type dusty gas shocks is restricted to the range

$$\tilde{c}_s = \frac{c_s}{\sqrt{1+D}} < v_s < c_s. \tag{5.3.13}$$

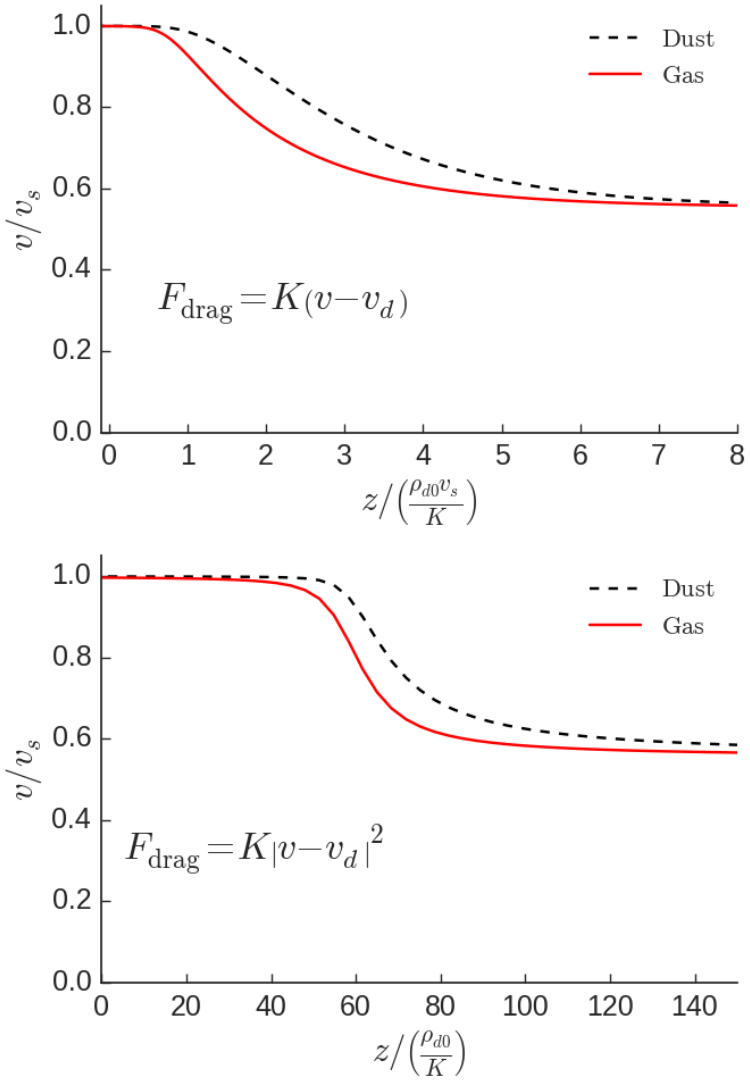

Figure 5.3: Same as Fig. 5.2 but for a C-type shock with Mach number $\mathcal{M} = 0.95$ and $D = 1$.

This means that when the initial dust-to-gas ratio becomes small—such as the typical interstellar value of 0.01—v_s cannot be much larger than $\tilde{c}_s$, resulting in a very weak shock. For this reason, C-type dusty shocks may not be relevant to the general ISM. However, strong variations of D have been found in simulations of turbulent molecular clouds when dust-gas decoupling has been modeled (Hopkins and Lee, 2016), and values as high as unity have been used in protostellar discs (e.g. Dipierro et al., 2015) to account for dust migration to the inner parts of the disc.

We have presented two potential benchmarking problems for numerical codes seeking to simulate dusty gas systems. These problems allow a code to test the implementation of different forms of drag, the strength of the drag (K) and the dust-to-gas mass density ratio (D). In the following section we provide an astrophysical application of two-fluid dust-gas shocks.

5.4 Protoplanetary Disc Accretion Shock

Here we present an astrophysical application of two-fluid dust-gas shocks. At very early stages of star formation, the system is characterised by an embedded protostellar disc surrounded by an infalling envelope of dust and gas. The material falls, due to gravity, through an accretion shock and then eventually settles onto the disc. Here we model this accretion shock as a two-fluid dust-gas shock. We first derive the defining shock parameters using simple physical considerations. Then we detail the astrophysical drag, heating and cooling terms. Finally, we discuss the structure of the accretion shock.

5.4.1 Shock Parameters

In this section we consider typical physical properties of protoplanetary discs in order to constrain the appropriate preshock conditions to model the accretion shock. We then consider the shock geometry by equating the disc thermal pressure with the shock's ram pressure.

The accretion rate onto a protoplanetary disc in the inside-out collapse model of a singular isothermal sphere can be approximated (Larson, 2003) as

$$\dot{M} \sim \frac{c_s^3}{G} = 2 \times 10^{-6}\,\mathrm{M}_\odot\,\mathrm{yr}^{-1}, \tag{5.4.1}$$

where G is the gravitational constant, and we have assumed the typical interstellar medium sound speed $c_s = 0.2$ km s^{-1}. This mass is spread over the area of the disc,

so that the mass flux of the accretion shock is

$$\rho_0 v_s = \frac{\dot{M}}{\pi R_d^2} \sim \frac{c_s^3}{G\pi R_d^2} \tag{5.4.2}$$

$$\sim 1.7 \times 10^{-11} \left(\frac{R_d}{100\,\mathrm{au}}\right)^{-2} \mathrm{g\,s^{-1}\,cm^{-2}}, \tag{5.4.3}$$

where R_d is the disc radius. The material accretes in free-fall and thus reaches the protoplanetary disc at the escape speed. The gas meets a disc in Keplerian motion, and so the shock velocity

$$v_s \sim \sqrt{\frac{GM_*}{r}}, \tag{5.4.4}$$

where r is the distance from the central protostar with mass M_*. Using this velocity and equation (5.4.3) for a solar mass protostar we get a preshock density of

$$\rho_0 \sim 4 \times 10^{-17} \left(\frac{R_d}{100\,\mathrm{au}}\right)^{-2} \left(\frac{r}{50\,\mathrm{au}}\right)^{1/2} \mathrm{g\,cm^{-3}}. \tag{5.4.5}$$

This corresponds to a total hydrogen number density, $n_\mathrm{H} \approx n(\mathrm{H}) + 2n(\mathrm{H_2})$, of

$$n_0 = \frac{\rho_0}{1.4 m_\mathrm{H}} \sim 2 \times 10^7 \left(\frac{R_d}{100\,\mathrm{au}}\right)^{-2} \left(\frac{r}{50\,\mathrm{au}}\right)^{1/2} \mathrm{cm^{-3}}. \tag{5.4.6}$$

The shock will be located where its ram pressure is balanced by the thermal pressure of the disc. That is, where

$$n_0 v_s^2 = n_\mathrm{disc}(r, z) c_\mathrm{disc}(r)^2, \tag{5.4.7}$$

where the disc density and sound speed are functions of radial distance from the star, r, and vertical distance from the disc, z. These functions can be approximated in the minimum mass solar nebula model (Wardle, 2007) as

$$n_\mathrm{disc}(r, z) \sim 5.8 \times 10^{14}\,\mathrm{cm^{-3}} \left(\frac{r}{\mathrm{au}}\right)^{-11/4} \exp\left(-\frac{z^2}{2h^2}\right), \tag{5.4.8}$$

$$c_\mathrm{disc}(r) \sim 0.99\,\mathrm{km\,s^{-1}} \left(\frac{r}{\mathrm{au}}\right)^{-1/4}, \tag{5.4.9}$$

with the scale height, h, is given by

$$\frac{h}{r} \sim 0.03 \left(\frac{r}{\mathrm{au}}\right)^{1/4}. \tag{5.4.10}$$

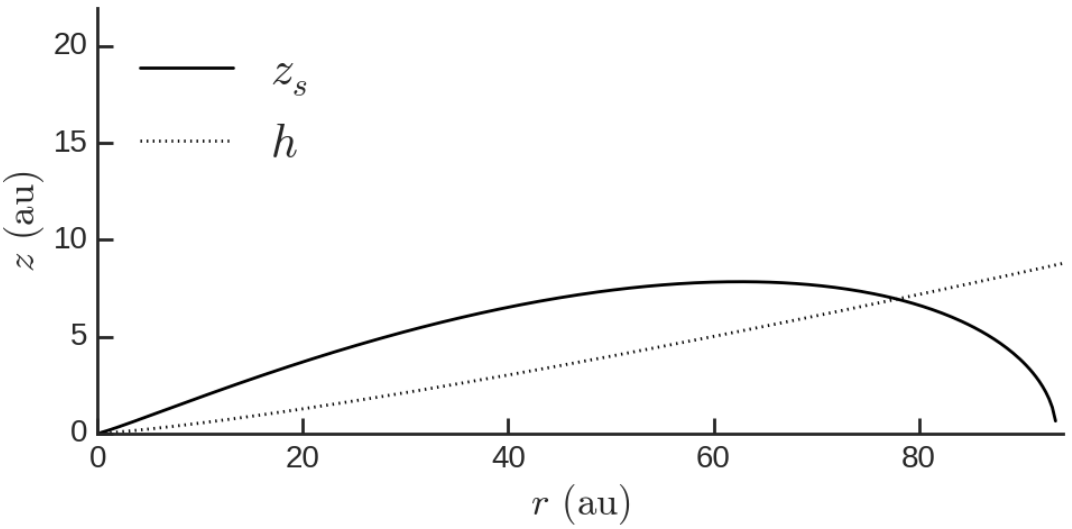

Figure 5.4: Location of shock (solid line), where the ram pressure of free-falling material balances the thermal pressure of the protoplanetary disc. The dotted line marks the scale height for comparison.

Subsituting these approximations into equation (5.4.7) and rearranging for the vertical height gives

$$z_s^2 = 2h^2 \ln\left(2.62 \times 10^5 \left(\frac{R_d}{100\,\mathrm{au}}\right)^2 \left(\frac{r}{\mathrm{au}}\right)^{-11/4}\right). \tag{5.4.11}$$

The location where the shock ram pressure balances the disc thermal pressure (z_s) is shown in Fig. 5.4 for a disc radius $R_d = 100$ au. Beyond $r \sim 95$ au, the disc density and sound speed has dropped so low that its thermal pressure never balances the shock ram pressure. In this region the shock will run up against the material freely falling from the other side of the disc. A sketch of the system is shown in Fig. 5.5. In the next section we model this accretion shock using representative values of the shock velocity and preshock density between 30–80 au, i.e. $v_s \sim 4$ km s^{-1} and $\rho_0 \sim 4 \times 10^{-17}$ g cm^{-3}, respectively. These parameters could be used to model an isothermal shock. However, heating and cooling impact the shock structure, and provide observational predictions through radiation. So in the next section we derive an ODE for the temperature profile of the shock, to be solved simultaneously with equation (5.3.1), and describe the appropriate heating and cooling terms.

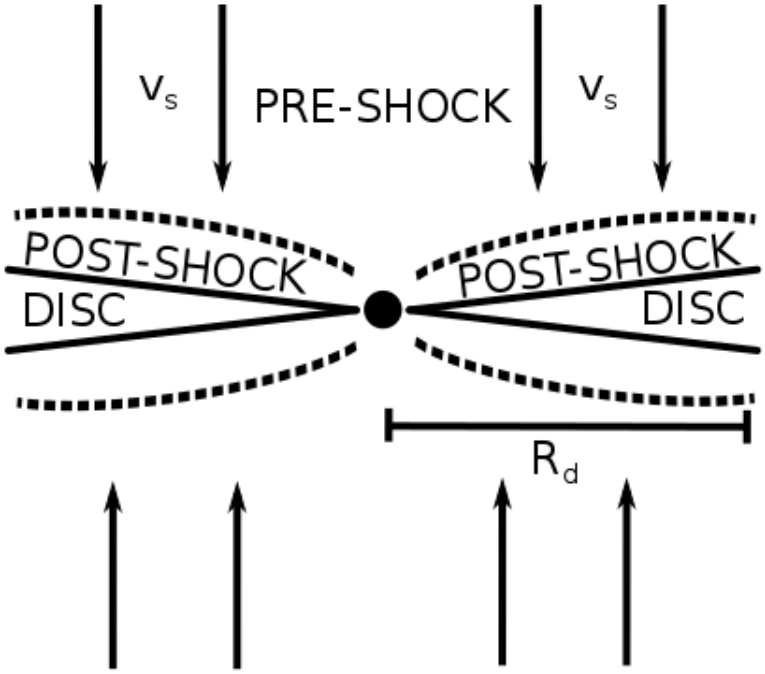

Figure 5.5: Sketch of model for accretion shock (dashed) onto protoplanetary disc.

5.4.2 Physical Processes

At 4 km s^{-1}, this shock is highly supersonic so we use the J-type model described in section 5.2.2. In this section we outline the modifications to the fluid equations to introduce astrophysically relevant drag, heating and cooling.

When the grain size is small compared to the surrounding gas mean free path the Epstein drag regime applies (Epstein, 1924) and the drag term, or momentum rate of change change per volume due to elastic scattering, can be expressed as (Draine, 1986):

$$F = \frac{\sigma \rho \rho_d}{m_d} \sqrt{\frac{2 k_B T}{\pi \mu}} \left(v_d - v\right) I\left(v, v_d, T\right), \tag{5.4.12}$$

where σ is the dust cross-section, m_d is the mass of a dust particle, μ is the mean mass per gas particle ($(7/3)m_{\rm H}$ in molecular gas), T is the gas temperature and k_B is the Boltzmann constant. The function $I(v, v_d, T)$ is well approximated by (Kwok, 1975):

$$I(v, v_d, T) \approx \frac{8}{3} \left(1 + \frac{9\pi}{64} \frac{\frac{1}{2}\mu \left|v - v_d\right|^2}{k_B T}\right)^{1/2}. \tag{5.4.13}$$

The derivative of the dust velocity through the shock can then be written as

$$\frac{dv_d}{dz} = \alpha v_s \sqrt{\frac{k_B T}{\mu}} I(v, v_d, T) \frac{v - v_d}{v_d v}, \tag{5.4.14}$$

where

$$\alpha = \frac{\rho_0 r_d^2 \sqrt{2\pi}}{m_d} \tag{5.4.15}$$

for preshock gas density ρ_0 and dust radius r_d. We have assumed that the dust cross-section is πr_d^2.

The energy equation (5.2.3) reduces, in the static plane-parallel case, to

$$v\frac{dP}{dz} + \gamma P \frac{dv}{dz} = (\gamma - 1)(\Gamma - \Lambda), \tag{5.4.16}$$

where we have assumed that the internal energy is proportional to the pressure

$$u = \frac{P}{\gamma - 1}. \tag{5.4.17}$$

For the present work, we will assume the adiabatic index $\gamma = 7/5$, appropriate for molecular gas at the high temperatures ($\sim$1000 K) reached in post-shock regions. Combining equation (5.4.16) with equations (5.2.12) and (5.2.13), along with the ideal gas law $P = \rho k_B T/\mu$, we derive the gas temperature derivative

$$\frac{1}{T}\frac{dT}{dz} = \frac{1}{\rho_0 v_s^3} \frac{\gamma - 1}{w^2 - \gamma\tau} \left(\left(\frac{w^2}{\tau} - 1 \right) (\Gamma - \Lambda) + vF \right), \tag{5.4.18}$$

where $\tau = k_B T/\mu v_s^2$. We also modify equation (5.3.7) to account for the variable temperature

$$w^2 + \left[D(w_d - 1) - 1 - \mathcal{M}^{-2} \right] w + \frac{k_B T}{\mu v_s^2} = 0. \tag{5.4.19}$$

Finally, the temperature jumps from the preshock value T_{g0} to T_j across the initial discontinuity following

$$\frac{T_j}{T_{g0}} = \left(1 + \frac{2\gamma}{\gamma + 1} \left(\mathcal{M}^2 - 1 \right) \right) \frac{\mathcal{M}^2 (\gamma - 1) + 2}{\mathcal{M}^2 (\gamma + 1)}. \tag{5.4.20}$$

From Draine (1986), the rate of change of the thermal energy per unit volume of the gas due to elastic scattering by dust with a velocity-independent cross section, σ, is

$$\Gamma_{\rm drag} = \frac{\sigma \rho \rho_d}{m_d^2} \sqrt{\frac{8 k_B T}{\pi \mu}} \left[k_B (T - T_d) I_2 + k_B T_d I_3 \right], \tag{5.4.21}$$

where

$$I_2 \approx \left(1 + \frac{9\pi}{64}\frac{\frac{1}{2}\mu\left|v - v_d\right|^2}{k_B T}\right)^{1/2}\left(4 + \frac{8}{3}\frac{\frac{1}{2}\mu\left|v - v_d\right|^2}{k_B T}\right), \tag{5.4.22}$$

and

$$I_3 \approx \left(1 + \frac{9\pi}{64}\frac{\frac{1}{2}\mu\left|v - v_d\right|^2}{k_B T}\right)^{1/2}\frac{8}{3}\frac{\frac{1}{2}\mu\left|v - v_d\right|^2}{k_B T}. \tag{5.4.23}$$

To calculate the dust temperature we assume that the frictional heating per grain, $\Gamma_{\rm drag}/n_d$, is always balanced by the power radiated by a dust grain. Following Draine (2011), grains lose energy by infrared emission at a rate, per grain,

$$\Lambda_d = 4\pi r_d^2 \left\langle Q_{\rm abs}\right\rangle \sigma_B T_d^4, \tag{5.4.24}$$

where σ_B is the Stefan-Boltzmann constant and $\langle Q_{\rm abs}\rangle$ is the Planck-averaged emission efficiency, which for carbon grains is

$$\left\langle Q_{\rm abs}\right\rangle_{\rm C} \sim 8\times 10^{-7}\left(\frac{r_d}{0.1\mu{\rm m}}\right)\left(\frac{T_d}{\rm K}\right)^2. \tag{5.4.25}$$

We include rotational line cooling from CO and H_2 using the cooling functions of Neufeld and Kaufman (1993) and Neufeld et al. (1995). They give the cooling rate per volume $\Lambda(M) = n(M)n({\rm H_2})L_{\rm M}$ for a molecule M using a cooling rate coefficient $L_{\rm M}$ obtained by fitting to four parameters of the form

$$\frac{1}{L_{\rm M}} = \frac{1}{L_0} + \frac{n({\rm H_2})}{L_{\rm LTE}} + \frac{1}{L_0}\left(\frac{n({\rm H_2})}{n_{1/2}}\right)^{\alpha}\left(1 - \frac{n_{1/2}L_0}{L_{\rm LTE}}\right). \tag{5.4.26}$$

The parameters L_0, $L_{\rm LTE}$, $n_{1/2}$ and α are tabulated for temperatures up to a few thousand K, and depend on an optical depth parameter $\tilde{N}$. Modeling the shock as a plane-parallel slab of thickness d, this parameter is given as

$$\tilde{N}({\rm CO}) = \frac{n({\rm CO})d}{9\Delta v}. \tag{5.4.27}$$

We have chosen a CO abundance $x({\rm CO}) = 1.24\times 10^{-4}$ with respect to the total hydrogen density and molecular hydrogen abundance $x({\rm H_2}) = 0.5$, both constant throughout the shock. We thus use an optical depth parameter $\tilde{N}({\rm CO}) \sim 10^{15}$ cm^{-2}/(km/s), appropriate for a shock thickness of 1 au and Δv=4 km s^{-1}.

Finally, we choose a preshock gas and dust temperature $T_{g0} = T_{d0} = 10$ K, corresponding to an isothermal sound speed $c_s = 0.188$ km s^{-1}, and we do not allow either temperature to fall below their initial value.

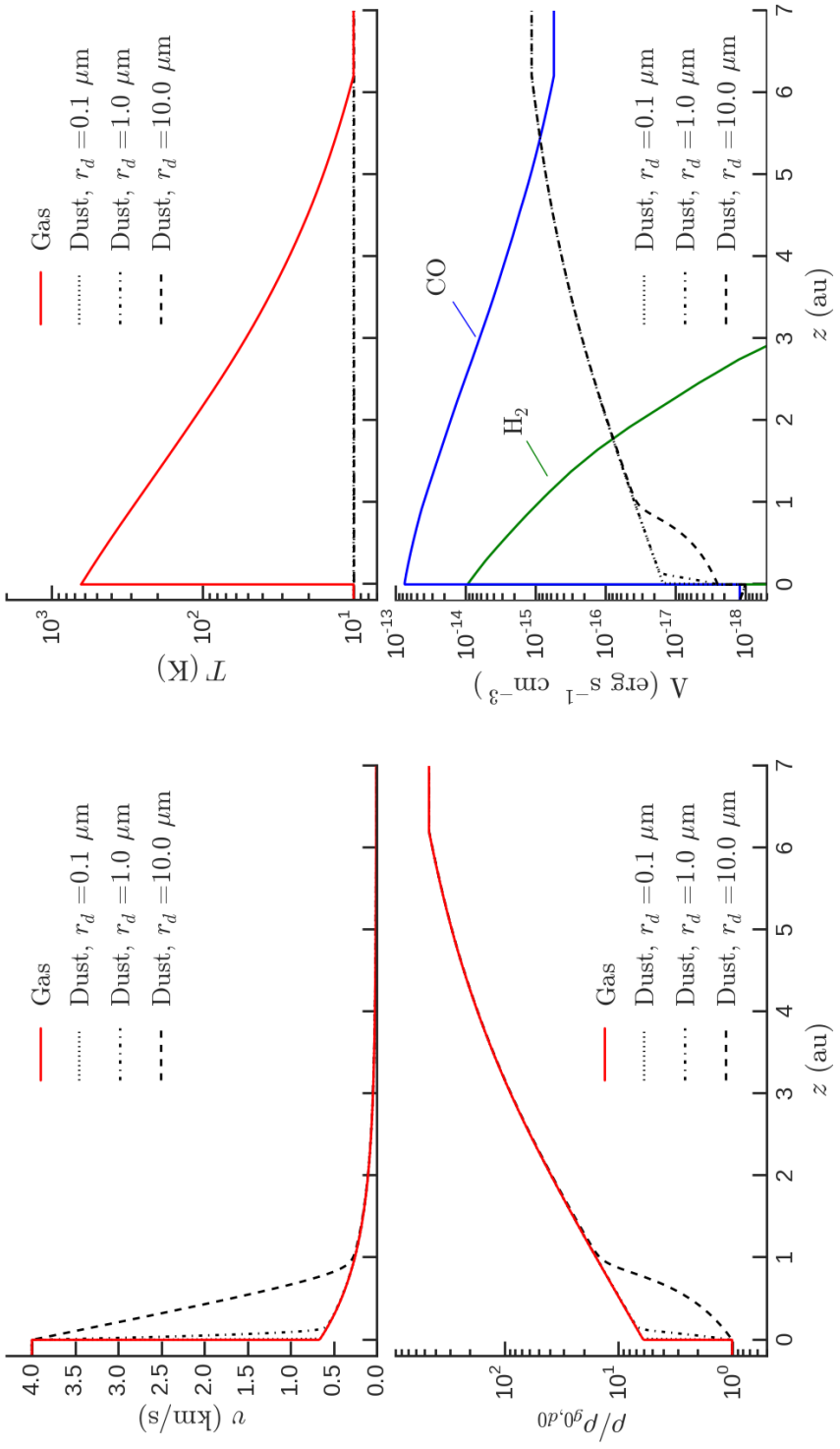

Figure 5.6: Accretion shock profiles for v_s=4 km s^{-1}, $\rho_0 = 4 \times 10^{-17}$ g cm^{-3}, preshock dust-to-gas ratio $D = 0.01$ and three different dust sizes, r_d=0.1 (dotted), 1 (dash-dotted) and 10 (dashed) μm. Upper left panel shows the velocity profiles, lower left panel shows the density profiles, upper right shows the temperature profile and lower panel shows the cooling profiles. The gas velocity, density and temperature profiles (solid red lines) and the H_2 and CO cooling rates cannot be distinguished in the three cases. Note that in the density profile, the gas and dust densities are normalised by their respective preshock densities, which differs by a factor of 100 in this case.

Here we estimate the thickness of the dust-gas drift region for the $v_s \sim 4$ km s^{-1} shock we are considering. The gas temperature immediately behind the shock will jump from 10 to $\sim 10^3$ K (equation (5.4.20)). The velocity jumps as

$$\frac{v_j}{v_s} = \frac{\gamma - 1}{\gamma + 1} + \frac{2}{\mathcal{M}^2 (\gamma + 1)}, \tag{5.4.28}$$

which gives $v_j \sim v_s/6$. If we estimate the drift velocity $\Delta v = v_d - v \sim v_s/2$, assume spherical carbon dust particles with average mass density ~ 2.2 g cm^{-3}, then we the size over which the dust will drift with respect to the gas is approximately

$$\Delta z \sim \frac{v_d v}{\alpha v_s I} \left(\frac{k_B T}{\mu} \right)^{-1/2} \sim 0.05 \, \text{au} \left(\frac{r_d}{\mu \text{m}} \right). \tag{5.4.29}$$

Hence the shock remains thin compared to the size of the system shown in Fig. 5.4.

5.4.3 Results and Discussion

With the heating and cooling processes in place, we numerically integrate the coupled ODEs as discussed in section 5.3.1 for J-type shocks. We first investigate the effect of different sizes of dust grains by considering a constant initial dust-to-gas ratio $D = 0.01$. The resulting velocity, density, temperature and cooling rate profiles computed for dust sizes $r_d = 0.1$, 1 and 10 μm are shown in Fig. 5.6.

When $r_d = 0.1$ μm, the region of the shock with any drift between the dust and gas velocities is negligible compared to the size of the shock, and so closely resembles a one-fluid shock. However, when $r_d = 10$ μm this region is about half the size of the shock and agrees with the estimate of equation (5.4.29). Hence we expect two-fluid effects to be more prominent in accretion shocks where the dust has coagulated into large grains ($r_d > 1$ μm). In this initial region of dust-gas drift, the dust to gas ratio decreases from its initial value to a minimum 6 times smaller than D immediately after the jump. The ratio returns to its preshock value after $\sim$1 au in the $r_d = 10$ μm case. Note that the shock thickness $\sim$6 au, which is approaching the limits of validity for this model.

In the lower right panel of Fig. 5.6, the volume cooling rates of CO and H_2 negligibly differ in shocks with different dust sizes. This is because the gas temperature (upper right panel of Fig. 5.6) is the same in all shocks. Note that the dust is never heated above 10 K in any of the shock models. The volume cooling rate of the dust, however, is sensitive to the dust size only in the drift region. When the dust-to-gas ratio returns to its preshock value, the dust cooling rate remains the same for all dust sizes.

We next consider the dependence on the initial dust-to-gas ratio. The canonical value in the interstellar medium is $D = 0.01$, however values as high as unity have

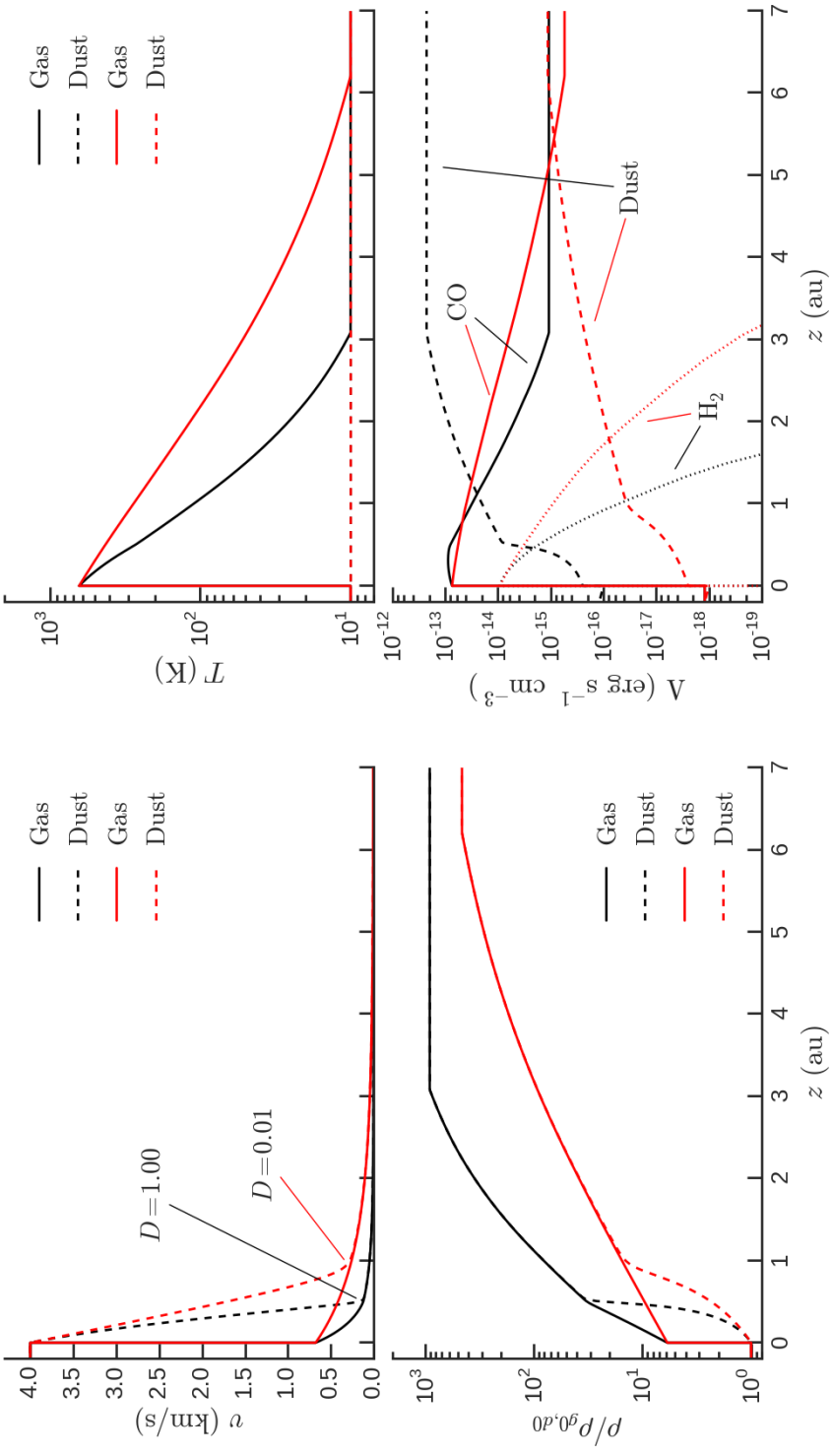

Figure 5.7: Accretion shock profiles for v_s=4 km s^{-1}, $\rho_0 = 4 \times 10^{-17}$ g cm^{-3}, and dust size $r_d = 10$ μm. Upper left panel shows the velocity profiles, lower left panel shows the density profiles, upper right shows the temperature profile and lower panel shows the cooling profiles. Red lines refer to shocks with initial dust-to-gas ratio $D = 0.01$ while black lines have $D = 1$. Dashed lines refer to dust variables and solid lines refer to gas variables in the velocity and density profiles. In the cooling profile, solid lines refer to CO, dotted lines refer to H_2 and dashed lines refer to dust. Note that in the density profile, the gas and dust densities are normalised by their respective preshock densities, which differs in the $D = 0.01$ case.

been used in protostellar discs (e.g. Dipierro et al., 2015) to account for dust migration to the inner parts of the disc. The velocity, density, temperature and cooling profiles for accretion shocks with $D = 0.01$ and $D = 1$ are shown in Fig. 5.7 for the case where the dust size $r_d = 10$ μm. The profiles are similar, with the larger dust-to-gas ratio resulting in a more compressed structure. There is strong CO and H_2 emission in these shocks as well as those shown in Fig. 5.6, due to the high temperatures reached ($\sim 10^3$ K). This suggests that observing rotational lines of CO or H_2 are good tracers of the presence of an accretion shock, but are not sensitive to the shock parameters. On the other hand, while CO is the dominant coolant when $D = 0.01$, dust cooling dominates after $\sim$1 au when $D = 1$. This means dust emission probes the initial dust-to-gas ratio of the accretion shock.

We have presented an astrophysical application of two-fluid dust-gas shocks by studying the accretion shock above a protoplanetary disc. We have simplified the system by not including any chemical reactions or evaporation of grain mantles. At the temperatures reached ($\sim 10^3$ K) there is significant driving of neutral-neutral reactions, and coolants such as H_2O and OH could be produced. Cooling by these molecules could change the detailed structure of the shock and/or provide radiative signatures of the shock parameters. Our simple treatment has shown that a detailed analysis of dust-gas shocks could be useful to investigate infalling material onto protoplanetary discs. In addition, we have only considered a shock velocity appropriate for a solar mass protostar. Lower mass protostars would lead to lower shock velocities (equation (5.4.4)) and therefore lower postshock temperatures (equation (5.4.20)). Thus, detailed shock models at a range of velocities could provide radiative signatures of protostellar mass.

5.5 Conclusion

We have numerically solved the two-fluid dust-gas equations assuming a steady-state, planar structure. Two distinct shock solutions exist where the gas fluid drags the dust fluid along through a discontinuity (J-type) or smoothly (C-type) until both fluids settle onto post-shock values. These shocks are ideal tests for benchmarking the behaviour of numerical codes seeking to simulate dusty gas with different expressions for the drag or dust-to-gas mass density ratios. Our PYTHON code that returns shock solutions for user defined parameters is publicly available on the Python Package Index[4] and BitBucket[5].

We used a J-type two-fluid dust-gas shock to study the accretion shock settling material onto a protoplanetary disc. We found that two-fluid effects are most likely to be important for larger grains ($r_d > 1$ μm). Dust emission from within the shock

[4]https://pypi.python.org/pypi/DustyShock
[5]https://bitbucket.org/AndrewLehmann/dustyshock

front was found to be a sensitive probe of the dust-to-gas ratio that eventually falls onto the protoplanetary disc. This work shows that a detailed analysis of two-fluid dust-gas shocks could be a fruitful avenue to investigating the composition of infalling material onto protoplanetary systems.

Chapter 6

Conclusion

Shock waves are ubiquitous in the violent interstellar medium, and particularly in molecular clouds. In this thesis, multifluid treatments of shocks have been used to study the turbulent dissipation of molecular clouds and the material accreting onto protoplanetary discs. The chemical processing within hot shock fronts and the radiative signatures of shocks probe key processes determining the physical conditions of these systems. I summarise the main results of the thesis here and then consider future directions motivated by this work.

I presented the first published two-fluid models of slow magnetohydrodynamic (MHD) shocks. Slow shocks were shown to be structurally and observationally distinct from the well-studied C-type fast MHD shocks. While fast shocks are driven by magnetic pressure, slow shocks are driven by gas pressure. Consequently slow shocks are thinner and hotter than fast shocks of the same velocity. The radiative transfer tool RADEX was used to show stronger excitation of rotational lines of CO above $J = 6$–5 in slow shocks due to the higher temperatures. Furthermore, these high-J lines may have already been detected in observations of infrared dark clouds. Subsequent analysis of the same infrared dark clouds have confirmed that a slow shock interpretation remains consistent with the data (Pon et al., 2016b).

The observational differences between different families of MHD shocks motivated the development a publicly available algorithm, SHOCKFIND, to detect and characterise the shocks in simulations of magnetised molecular clouds. This work resulted in the first predicted mixture of shock families in a turbulent molecular cloud. Both fast and slow shocks were present at significant levels. Their distributions of shock speeds, Alfvénic Mach numbers and preshock parameters were used in combination with the detailed shock models from Chapter 2 to predict a small volume (0.1%) of shock heated gas, and to produce synthetic emission maps.

Models of photodissociation regions with enhanced cosmic-ray ionization rates were developed to compare against updated shock models to study the molecular clouds near the centre of the galaxy. The unusually high temperatures observed

in these clouds have been explained by either turbulent dissipation in shocks or elevated ionization rates. Building on the models in chapter 2, I expanded the chemical network and added heating and cooling functions. I developed a line-of-sight model that crosses regions of shocked and ambient gas, providing chemical signatures of the turbulent dissipation. In particular, with 0.1% of the line of sight occupied by shock-heated gas, abundance enhancements of 1–2 orders of magnitude were found for sulphur-bearing species such as SO_2 and H_2S, as well as nitrogen-bearing species such as HCN and NH_3. RADEX was used to compare rotational line emission from HCN from fast and slow shocks to unshocked gas. Emission of the $J = 1$–0 line from slow shocks was shown to be consistent with observations of various regions of the Central Molecular Zone.

Finally, two-fluid dust-gas shocks were then presented as benchmarking problems for numerical codes seeking to simulate dusty gas. Two classes of shock solutions analogous to C- and J-type magnetised shocks were presented. These shocks fill the need for simple analytic solutions to calibrate the bahaviour of numerical codes for different dust-to-gas ratios and implementations of drag. In addition, two-fluid dusty shocks were used to study the accretion shock occurring when freefalling material runs up against a protoplanetary disc. This simple application motivates a detailed treatment of dusty shocks, as the chemical composition of protoplanetary discs may be strongly shaped by the passage through such a shock.

The work in this thesis shows the importance and wide applicability of multi-fluid shock waves in molecular clouds. Furthermore, I have shown that two-fluid treatments are essential to accurately model the structure of shocks and to obtain accurate radiative signatures. Such radiation can be used to test the physical processes giving rise to the shock waves.

6.1 Future Work

The SHOCKFIND algorithm can be applied to any MHD simulation. In future, I plan to characterise the shocks in simulations of molecular clouds with different turbulence parameters. Correlations between driving modes, initial magnetic field strength and inclusion of non-ideal MHD effects with the mixture of shocks could provide robust observational predictions of these processes. In addition, SHOCKFIND could be combined with the filament finding algorithm, DISPERSE, to study the ubiquitously observed filaments in turbulent clouds. These have often been explained as occuring at the line of intersection of colliding planar shocks. This could be studied in simulations, and synthetic observations could test this hypothesis in real clouds.

Shock models can always be improved. For the purposes of studying molecular clouds, one obvious improvement is to include dust chemistry in the model. This means modeling the adsorption of gas species onto grains and desorption back into

the gas phase, as well as the grain surface chemistry. Depletion of key species onto dust can significantly affect the remaining gas-phase chemistry. In addition, some species are more efficiently produced on dust before being desorbed into the gas-phase. The addition of dust chemistry would significantly improve the accuracy of the chemical signatures of shocks presented in this thesis. Furthermore, modeling the shattering of dust grains due to collisions with other grains would allow a study of the grain-size distribution of material falling onto protoplanetary discs.

Another key improvement to the shock models is in the treatment of radiative transfer. I post-processed the shock models using a radiative transfer tool, RADEX, to estimate rotational line emission. The population densities of the rotational levels of the important coolants could be calculated in parallel with the dynamical equations, providing a more accurate treatment of the radiative cooling. Observations of regions shocked by protostellar outflows have revealed strong emission from low-lying rotational lines of H_2, and so improved shock models could be used to model these regions.

Finally, fast shocks have long been treated as the only kind of magnetised shock in molecular cloud studies. This thesis shows that it is worth revisiting studies in which fast shock jump relations have been assumed, such as in theories where shocks set the initial mass function.

Appendices

Appendix A

SHOCKFIND tests

A.1 Cylinder Radius

Here we check the effect of varying the radius of the cylinder used to define average pre- and post-shock variables (step (iii) in section 3.3.1). Appendix A.1 shows the Mach number distributions for fast and slow shocks for runs of SHOCKFIND on the same locations, but with cylinder radii of $R = 1$, 3 and 5 in units of cell size. A radius of $R = 1$ defines the minimum cylinder size to represent a line that does not suffer aliasing effects. This size, however, is still affected by small scale numerical noise. Averaging over larger radii, $R = 3$ and $R = 5$, removes the effect of the numerical noise. There is little difference between these two larger radii, and so we choose $R = 3$ as the compromise between noise and lowering computational time.

A.2 Overcounting the shocked cells

In Fig. A.2 we show a close up of the detected shocked cells of a curved shock front. In this figure, it can be seen that the thickness of the shock front is 3 or 4 rows of detected cells. As the shock front area is required to link our work to the results of one-dimensional shock models, we are overcounting if we consider every detected cell as a unique unit of shocked area. In order to avoid this over counting we only use (as step (viii) of section 3.3.1) cells that occur at the local convergence maxima (filled squares in Fig. A.2) along the extracted line (step (iii) of section 3.3.1).

A.3 Convergence Test

Here we check that the search thresholds capture converged distributions of shocks. The convergence threshold defined in Sec. 3.4.1 searches down to $S = 2.7\%$ of cells

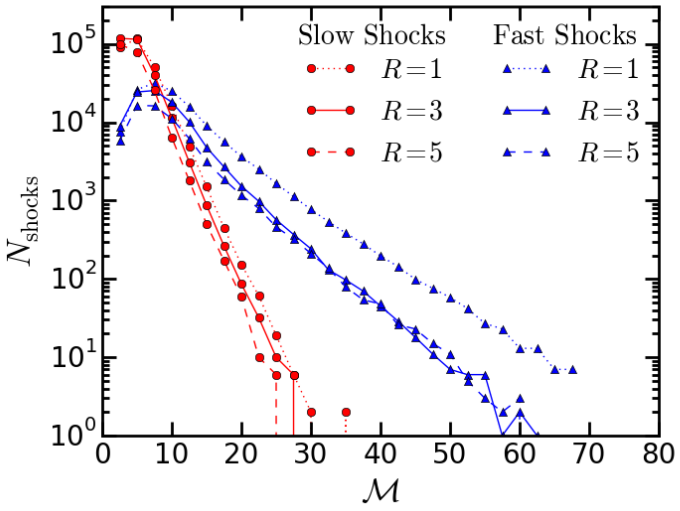

Figure A.1: Mach number distributions for the search described in section 3.4 but with averaging cylinder radiis of $R = 1$ (dotted), 3 (solid) and 5 (dashed).

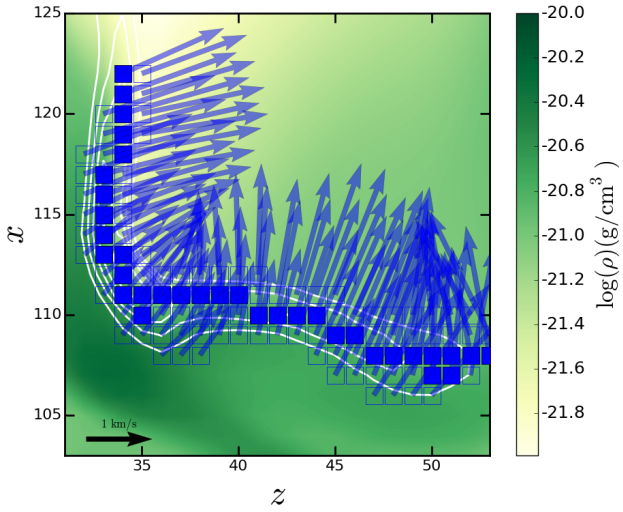

Figure A.2: Constant y slice of mass density (filled contours), convergence (white contours), detected shocked cells (squares) and arrows proportional to shock velocity in this plane. The filled squares denote cells at convergence peaks along the line defined by the shock velocity vector at that cell.

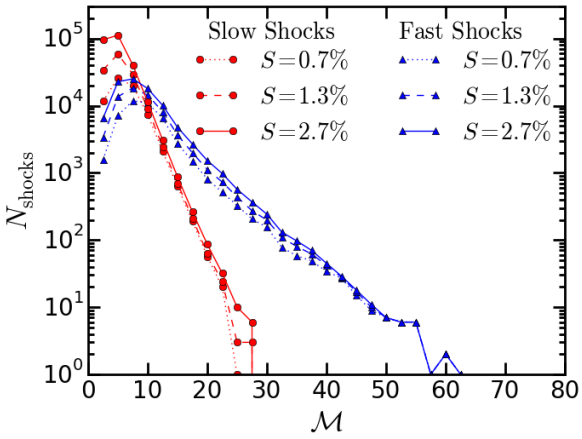

Figure A.3: Mach number distributions for searches of S = 0.7%, 1.3%, and 2.7% of possible shocked cells (those with $\nabla \cdot \mathbf{v} < 0$).

with negative divergence ($\nabla \cdot \mathbf{v}$), i.e., of all possible shocked cells. Fig. A.3 shows the effect of doubling the number of cells searched on the Mach number distributions of fast and slow shocks. The distributions are converged for the most observationally important shocks ($\mathcal{M} > 5$).

Appendix B

Milky Way clouds

B.1 Milky Way clouds

Here we repeat our line-of-sight model but for cloud and shock parameters appropriate for ordinary Milky Way molecular clouds. We model a typical Milky Way cloud as having a size of 5 pc, average total hydrogen number density $n_{\rm H} = 10^3$ cm^{-3}, a linewidth of 7 km s^{-1} for a velocity dispersion $\sigma \sim 3$ km s^{-1}, a dust temperature of 10 K, column density $N_{\rm H} \sim 8 \times 10^{21}$ cm^{-2}, extinction $A_V \sim 5$, UV radiation field $\chi = 1$ and elemental abundances unchanged from table 4.3. We also consider two ionization rates $\zeta = 10^{-17}$ and 10^{-16} H^{-1} s^{-1}, leading to equilibrium temperatures of 10 and 12 K, respective.

The shock models for these clouds have shock speeds v_s =1, 2 or 3 km s^{-1} and preshock density $n_0 = 10^2$ cm^{-3}. The fast shocks have a preshock Alfvén velocity of 0.6 km s^{-1}, giving a preshock magnetic field strength of $\sim$3 μG. The slow shocks have a preshock Alfvén velocity of 4 km s^{-1}, giving a preshock magnetic field strength of $\sim$22 μG.

The abundances of all species from the equilibrium and turbulent cloud models are shown in Fig. B.1. When only the shock fronts are included, there is negligible difference between all the models. At these low shock speeds the temperatures do not reach high enough values to drive strong chemical changes. When the post-shock regions are included, then the sulphur-bearing species SO, SO_2, H_2S and HSO^+, oxygen species O_2 and O_2^+, as well as CH_4 show significant enhancement above their equilibrium values.

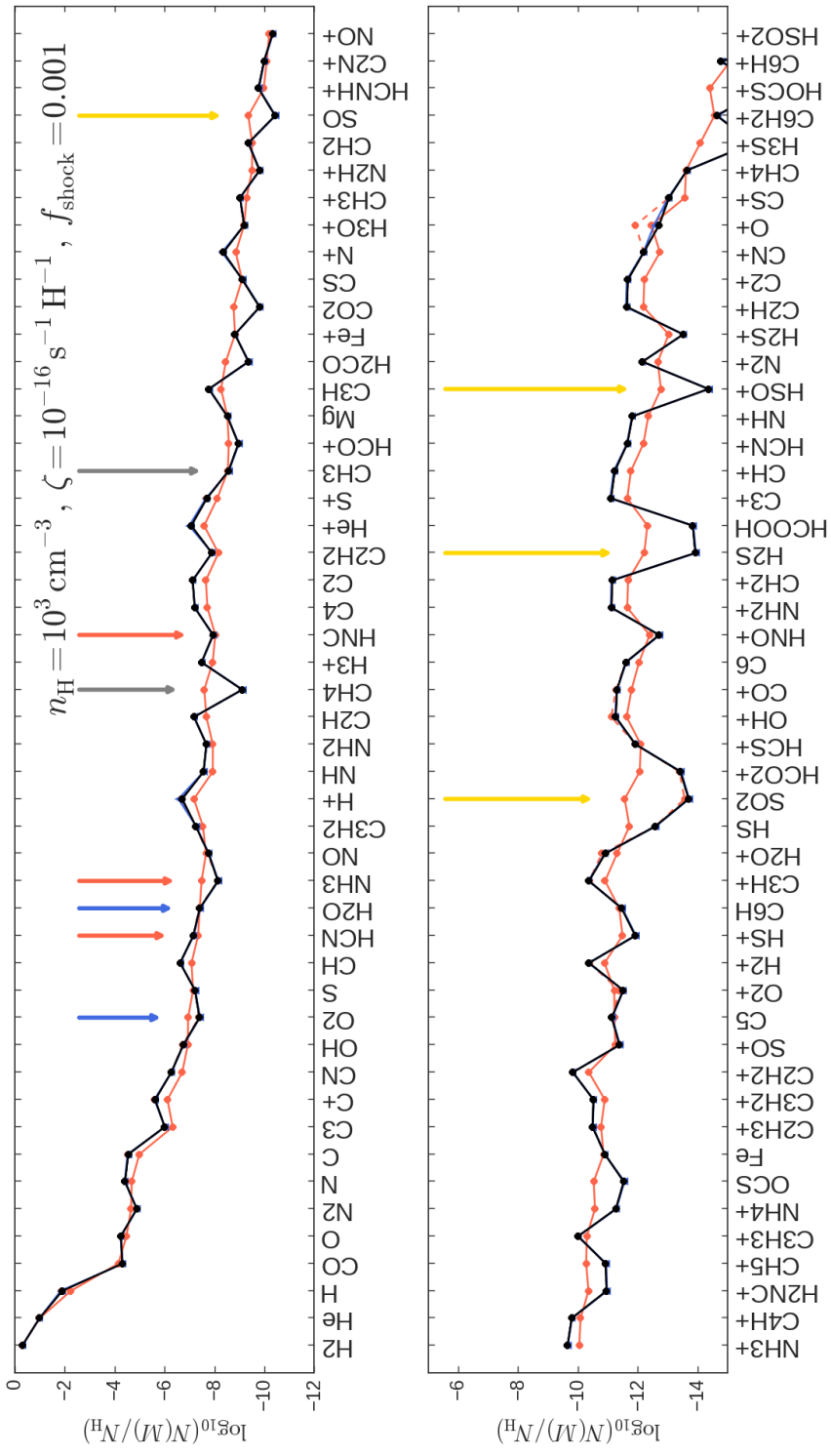

Figure B.1: Abundances of all species for shocked cloud model with $n_{\rm H} = 10^3$ cm^{-3} and $\zeta = 10^{-16}$ s^{-1} H^{-1}. The black solid line indicates the equilibrium model values (as in Fig. 4.5), whereas the blue triangles and red circles refer to turbulent cloud models including exclusively fast shocks and exclusively slow shocks, respectively. In the turbulent cloud models, the fraction of the line-of-sight in shock fronts is 0.1%, and the fraction in post-shock gas is $f_{\rm pst} = 2.4\%$ (solid red) or not included (dashed red). The coloured arrows indicate the same species emphasised in Fig. 4.5.

Bibliography

ALMA Partnership, Brogan, C. L., Pérez, L. M., Hunter, T. R., et al. (2015). The 2014 ALMA Long Baseline Campaign: First Results from High Angular Resolution Observations toward the HL Tau Region. *ApJ*, 808:L3.

André, P., Di Francesco, J., Ward-Thompson, D., Inutsuka, S.-I., Pudritz, R. E., and Pineda, J. E. (2014). From Filamentary Networks to Dense Cores in Molecular Clouds: Toward a New Paradigm for Star Formation. *Protostars and Planets VI*, pages 27–51.

Ao, Y., Henkel, C., Menten, K. M., Requena-Torres, M. A., Stanke, T., Mauersberger, R., Aalto, S., Mhle, S., and Mangum, J. (2013). The thermal state of molecular clouds in the Galactic center: evidence for non-photon-driven heating. *A&A*, 550:135.

Arons, J. and Max, C. E. (1975). Hydromagnetic Waves in Molecular Clouds. *ApJ*, 196:L77.

Arzoumanian, D., André, P., Didelon, P., Knyves, V., Schneider, N., Men'shchikov, A., Sousbie, T., Zavagno, A., Bontemps, S., di Francesco, J., Griffin, M., Hennemann, M., Hill, T., Kirk, J., Martin, P., Minier, V., Molinari, S., Motte, F., Peretto, N., Pezzuto, S., Spinoglio, L., Ward-Thompson, D., White, G., and Wilson, C. D. (2011). Characterizing interstellar filaments with Herschel in IC 5146. *A&A*, 529:L6.

Bai, X.-N. and Stone, J. M. (2010a). The Effect of the Radial Pressure Gradient in Protoplanetary Disks on Planetesimal Formation. *ApJ*, 722:L220–L223.

Bai, X.-N. and Stone, J. M. (2010b). Particle-gas Dynamics with Athena: Method and Convergence. *ApJS*, 190:297–310.

Bakes, E. L. O. and Tielens, A. G. G. M. (1994). The photoelectric heating mechanism for very small graphitic grains and polycyclic aromatic hydrocarbons. *ApJ*, 427:822–838.

Bally, J. (2016). Protostellar Outflows. *ARA&A*, 54:491–528.

Balsara, D. S. (1996). Wave Propagation in Molecular Clouds. *ApJ*, 465:775.

Basu, S. and Murali, C. (2001). Constraints on Stirring and Dissipation of MHD Turbulence in Molecular Clouds. *ApJ*, 551:743–746.

Bayet, E., Williams, D. A., Hartquist, T. W., and Viti, S. (2011). Chemistry in cosmic ray dominated regions. *MNRAS*, 414:1583–1591.

Becklin, E. E. and Gehrz, R. D. (2009). SOFIA: Stratospheric Observatory for Infrared Astronomy. volume 417, page 101.

Belloche, A., Mller, H. S. P., Menten, K. M., Schilke, P., and Comito, C. (2013). Complex organic molecules in the interstellar medium: IRAM 30 m line survey of Sagittarius B2(N) and (M). *A&A*, 559:A47.

Bergin, E. A. and Tafalla, M. (2007). Cold Dark Clouds: The Initial Conditions for Star Formation. *ARA&A*, 45:339–396.

Blandford, R. D. and Payne, D. G. (1982). Hydromagnetic flows from accretion discs and the production of radio jets. *MNRAS*, 199:883–903.

Blitz, L. and Shu, F. H. (1980). The origin and lifetime of giant molecular cloud complexes. *ApJ*, 238:148–157.

Bradford, C. M., Stacey, G. J., Nikola, T., Bolatto, A. D., Jackson, J. M., Savage, M. L., and Davidson, J. A. (2005). Warm Molecular Gas Traced with CO J = 7–>6 in the Galaxy's Central 2 Parsecs: Dynamical Heating of the Circumnuclear Disk. *ApJ*, 623:866–876.

Brandenburg, A. and Dobler, W. (2002). Hydromagnetic turbulence in computer simulations. *Computer Physics Communications*, 147:471–475.

Brunt, C. M. and Heyer, M. H. (2002). Interstellar Turbulence. II. Energy Spectra of Molecular Regions in the Outer Galaxy. *ApJ*, 566:289–301.

Burkhart, B., Lazarian, A., Balsara, D., Meyer, C., and Cho, J. (2015). Alfvénic Turbulence Beyond the Ambipolar Diffusion Scale. *ApJ*, 805:118.

Burkhart, B., Lazarian, A., Ossenkopf, V., and Stutzki, J. (2013). The Turbulence Power Spectrum in Optically Thick Interstellar Clouds. *ApJ*, 771:123.

Burton, M. G., Hollenbach, D. J., and Tielens, A. G. G. (1992). Mid-infrared rotational line emission from interstellar molecular hydrogen. *ApJ*, 399:563–572.

Carrier, G. F. (1958). Shock waves in a dusty gas. *JFM*, 4(04):376–382.

Chapman, J. F. and Wardle, M. (2006). Dust grain dynamics in C-type shock waves in molecular clouds. *MNRAS*, 371:513–529.

Chernoff, D. F. (1987). Magnetohydrodynamic shocks in molecular clouds. *ApJ*, 312:143–169.

Crutcher, R. M. (1999). Magnetic Fields in Molecular Clouds: Observations Confront Theory. *ApJ*, 520:706–713.

Crutcher, R. M., Troland, T. H., Goodman, A. A., Heiles, C., Kazes, I., and Myers, P. C. (1993). OH Zeeman observations of dark clouds. *ApJ*, 407:175–184.

Crutcher, R. M., Wandelt, B., Heiles, C., Falgarone, E., and Troland, T. H. (2010). Magnetic Fields in Interstellar Clouds from Zeeman Observations: Inference of Total Field Strengths by Bayesian Analysis. *ApJ*, 725:466–479.

Cunningham, A. J., Klein, R. I., Krumholz, M. R., and McKee, C. F. (2011). Radiation-hydrodynamic Simulations of Massive Star Formation with Protostellar Outflows. *ApJ*, 740:107.

de Graauw, T., Helmich, F. P., Phillips, T. G., Stutzki, J., Caux, E., Whyborn, N. D., Dieleman, P., Roelfsema, P. R., Aarts, H., Assendorp, R., Bachiller, R., Baechtold, W., Barcia, A., Beintema, D. A., Belitsky, V., Benz, A. O., Bieber, R., Boogert, A., Borys, C., Bumble, B., Cas, P., Caris, M., Cerulli-Irelli, P., Chattopadhyay, G., Cherednichenko, S., Ciechanowicz, M., Coeur-Joly, O., Comito, C., Cros, A., de Jonge, A., de Lange, G., Delforges, B., Delorme, Y., den Boggende, T., Desbat, J.-M., Diez-González, C., di Giorgio, A. M., Dubbeldam, L., Edwards, K., Eggens, M., Erickson, N., Evers, J., Fich, M., Finn, T., Franke, B., Gaier, T., Gal, C., Gao, J. R., Gallego, J.-D., Gauffre, S., Gill, J. J., Glenz, S., Golstein, H., Goulooze, H., Gunsing, T., Gsten, R., Hartogh, P., Hatch, W. A., Higgins, R., Honingh, E. C., Huisman, R., Jackson, B. D., Jacobs, H., Jacobs, K., Jarchow, C., Javadi, H., Jellema, W., Justen, M., Karpov, A., Kasemann, C., Kawamura, J., Keizer, G., Kester, D., Klapwijk, T. M., Klein, T., Kollberg, E., Kooi, J., Kooiman, P.-P., Kopf, B., Krause, M., Krieg, J.-M., Kramer, C., Kruizenga, B., Kuhn, T., Laauwen, W., Lai, R., Larsson, B., Leduc, H. G., Leinz, C., Lin, R. H., Liseau, R., Liu, G. S., Loose, A., Lpez-Fernandez, I., Lord, S., Luinge, W., Marston, A., Martn-Pintado, J., Maestrini, A., Maiwald, F. W., McCoey, C., Mehdi, I., Megej, A., Melchior, M., Meinsma, L., Merkel, H., Michalska, M., Monstein, C., Moratschke, D., Morris, P., Muller, H., Murphy, J. A., Naber, A., Natale, E., Nowosielski, W., Nuzzolo, F., Olberg, M., Olbrich, M., Orfei, R., Orleanski, P., Ossenkopf, V., Peacock, T., Pearson, J. C., Peron, I., Phillip-May, S.,

Piazzo, L., Planesas, P., Rataj, M., Ravera, L., Risacher, C., Salez, M., Samoska, L. A., Saraceno, P., Schieder, R., Schlecht, E., Schlder, F., Schmlling, F., Schultz, M., Schuster, K., Siebertz, O., Smit, H., Szczerba, R., Shipman, R., Steinmetz, E., Stern, J. A., Stokroos, M., Teipen, R., Teyssier, D., Tils, T., Trappe, N., van Baaren, C., van Leeuwen, B.-J., van de Stadt, H., Visser, H., Wildeman, K. J., Wafelbakker, C. K., Ward, J. S., Wesselius, P., Wild, W., Wulff, S., Wunsch, H.-J., Tielens, X., Zaal, P., Zirath, H., Zmuidzinas, J., and Zwart, F. (2010). The Herschel-Heterodyne Instrument for the Far-Infrared (HIFI). *A&A*, 518:L6.

de Hoffmann, F. and Teller, E. (1950). Magneto-Hydrodynamic Shocks. *Phys. Rev.*, 80:692–703.

Dipierro, G., Price, D., Laibe, G., Hirsh, K., Cerioli, A., and Lodato, G. (2015). On planet formation in HL Tau. *MNRAS*, 453:L73–L77.

Draine, B. T. (1980). Interstellar shock waves with magnetic precursors. *ApJ*, 241:1021–1038.

Draine, B. T. (1986). Multicomponent, reacting MHD flows. *MNRAS*, 220:133–148.

Draine, B. T. (2011). *Physics of the Interstellar and Intergalactic Medium*.

Draine, B. T. and Bertoldi, F. (1996). Structure of Stationary Photodissociation Fronts. *ApJ*, 468:269.

Draine, B. T. and Katz, N. (1986a). Magnetohydrodynamic shocks in diffuse clouds. I - Chemical processes. *ApJ*, 306:655–666.

Draine, B. T. and Katz, N. (1986b). Magnetohydrodynamic shocks in diffuse clouds. II - Production of CH(+), OH, CH, and other species. *ApJ*, 310:392–407.

Dubey, A., Fisher, R., Graziani, C., Jordan, IV, G. C., Lamb, D. Q., Reid, L. B., Rich, P., Sheeler, D., Townsley, D., and Weide, K. (2008). Challenges of Extreme Computing using the FLASH code. volume 385, page 145.

Elmegreen, B. G. (2000). Star Formation in a Crossing Time. *ApJ*, 530:277–281.

Elmegreen, B. G. (2007). On the Rapid Collapse and Evolution of Molecular Clouds. *ApJ*, 668:1064–1082.

Elmegreen, B. G. and Burkert, A. (2010). Accretion-Driven Turbulence and the Transition to Global Instability in Young Galaxy Disks. *ApJ*, 712:294–302.

Elmegreen, B. G. and Scalo, J. (2004). Interstellar Turbulence I: Observations and Processes. *ARA&A*, 42:211–273.

Epstein, P. S. (1924). On the Resistance Experienced by Spheres in their Motion through Gases. *Phys. Rev.*, 23:710–733.

Etxaluze, M., Goicoechea, J. R., Cernicharo, J., Polehampton, E. T., Noriega-Crespo, A., Molinari, S., Swinyard, B. M., Wu, R., and Bally, J. (2013). Herschel observations of the Sagittarius B2 cores: Hydrides, warm CO, and cold dust. *A&A*, 556:137.

Falgarone, E. and Phillips, T. G. (1990). A signature of the intermittency of interstellar turbulence - The wings of molecular line profiles. *ApJ*, 359:344–354.

Falgarone, E., Troland, T. H., Crutcher, R. M., and Paubert, G. (2008). CN Zeeman measurements in star formation regions. *A&A*, 487:247–252.

Falle, S. A. E. G. and Komissarov, S. S. (2001). On the inadmissibility of non-evolutionary shocks. *J. Plas. Phys.*, 65:29–58.

Federrath, C. (2013). On the universality of supersonic turbulence. *MNRAS*, 436:1245–1257.

Federrath, C. (2015). Inefficient star formation through turbulence, magnetic fields and feedback. *MNRAS*, 450(4):4035–4042.

Federrath, C. (2016). On the universality of interstellar filaments: theory meets simulations and observations. *MNRAS*, 457:375–388.

Federrath, C. and Klessen, R. S. (2012). The Star Formation Rate of Turbulent Magnetized Clouds: Comparing Theory, Simulations, and Observations. *ApJ*, 761:156.

Federrath, C. and Klessen, R. S. (2013). On the Star Formation Efficiency of Turbulent Magnetized Clouds. *ApJ*, 763:51.

Federrath, C., Schrn, M., Banerjee, R., and Klessen, R. S. (2014). Modeling Jet and Outflow Feedback during Star Cluster Formation. *ApJ*, 790:128.

Federrath, C., Sur, S., Schleicher, D. R. G., Banerjee, R., and Klessen, R. S. (2011). A New Jeans Resolution Criterion for (M)HD Simulations of Self-gravitating Gas: Application to Magnetic Field Amplification by Gravity-driven Turbulence. *ApJ*, 731:62.

Fleck, Jr., R. C. (1981). On the generation and maintenance of turbulence in the interstellar medium. *ApJ*, 246:L151–L154.

Flower, D. R., Le Bourlot, J., Pineau des Forêts, G., and Cabrit, S. (2003). The contributions of J-type shocks to the H2 emission from molecular outflow sources. *MNRAS*, 341:70–80.

Flower, D. R. and Pineau Des Forêts, G. (1998). C-type shocks in the interstellar medium: profiles of CH^+ and CH absorption lines. *MNRAS*, 297:1182–1188.

Flower, D. R. and Pineau Des Forêts, G. (2010). Excitation and emission of H2, CO and H2o molecules in interstellar shock waves. *MNRAS*, 406:1745–1758.

Flower, D. R. and Pineau des Forêts, G. (2013). Characterizing shock waves in molecular outflow sources: the interpretation of Herschel and Spitzer observations of NGC 1333 IRAS 4b. *MNRAS*, 436:2143–2150.

Flower, D. R., Pineau des Forêts, G., Field, D., and May, P. W. (1996). The structure of MHD shocks in molecular outflows: grain sputtering and SiO formation. *MNRAS*, 280:447–457.

Flower, D. R., Pineau des Forêts, G., and Hartquist, T. W. (1985). Theoretical studies of interstellar molecular shocks. I - General formulation and effects of the ion-molecule chemistry. *MNRAS*, 216:775–794.

Flower, D. R., Pineau Des Forêts, G., and Walmsley, C. M. (2006). The abundances of nitrogen-containing molecules during pre-protostellar collapse. *A&A*, 456:215–223.

Fryxell, B., Olson, K., Ricker, P., Timmes, F. X., Zingale, M., Lamb, D. Q., MacNeice, P., Rosner, R., Truran, J. W., and Tufo, H. (2000). FLASH: An Adaptive Mesh Hydrodynamics Code for Modeling Astrophysical Thermonuclear Flashes. *ApJS*, 131:273–334.

Gingold, R. A. and Monaghan, J. J. (1977). Smoothed particle hydrodynamics - Theory and application to non-spherical stars. *MNRAS*, 181:375–389.

Ginsburg, A., Henkel, C., Ao, Y., Riquelme, D., Kauffmann, J., Pillai, T., Mills, E. A. C., Requena-Torres, M. A., Immer, K., Testi, L., Ott, J., Bally, J., Battersby, C., Darling, J., Aalto, S., Stanke, T., Kendrew, S., Diederik Kruijssen, J. M., Longmore, S., Dale, J., Guesten, R., and Menten, K. M. (2016). Dense gas in the Galactic central molecular zone is warm and heated by turbulence. *A&A*, 586:A50.

Glassgold, A. E., Galli, D., and Padovani, M. (2012). Cosmic-Ray and X-Ray Heating of Interstellar Clouds and Protoplanetary Disks. *ApJ*, 756:157.

Glover, S. C. O. and Clark, P. C. (2012). Is molecular gas necessary for star formation? *MNRAS*, 421:9–19.

Glover, S. C. O., Federrath, C., Mac Low, M.-M., and Klessen, R. S. (2010). Modelling CO formation in the turbulent interstellar medium. *MNRAS*, 404:2–29.

Goldreich, P. and Kwan, J. (1974). Molecular Clouds. *ApJ*, 189:441–454.

Gong, M., Ostriker, E. C., and Wolfire, M. G. (2016). A Simple and Accurate Network for Hydrogen and Carbon Chemistry in the ISM. *ArXiv e-prints*, 1610:arXiv:1610.09023.

Goto, M., Usuda, T., Nagata, T., Geballe, T. R., McCall, B. J., Indriolo, N., Suto, H., Henning, T., Morong, C. P., and Oka, T. (2008). Absorption Line Survey of H3+ toward the Galactic Center Sources. II. Eight Infrared Sources within 30 pc of the Galactic Center. *ApJ*, 688:306–319.

Gould, R. J. and Salpeter, E. E. (1963). The Interstellar Abundance of the Hydrogen Molecule. I. Basic Processes. *ApJ*, 138:393.

Gredel, R., Lepp, S., Dalgarno, A., and Herbst, E. (1989). Cosmic-ray-induced photodissociation and photoionization rates of interstellar molecules. *ApJ*, 347:289–293.

Guillet, V., Pineau Des Forêts, G., and Jones, A. P. (2007). Shocks in dense clouds. I. Dust dynamics. *A&A*, 476:263–277.

Gusdorf, A., Pineau Des Forêts, G., Cabrit, S., and Flower, D. R. (2008). SiO line emission from interstellar jets and outflows: silicon-containing mantles and non-stationary shock waves. *A&A*, 490:695–706.

Habing, H. J. (1968). The interstellar radiation density between 912 A and 2400 A. *BAN*, 19:421.

Hacar, A., Kainulainen, J., Tafalla, M., Beuther, H., and Alves, J. (2016). The Musca cloud: A 6 pc-long velocity-coherent, sonic filament. *A&A*, 587:A97.

Heiles, C. and Troland, T. H. (2004). The Millennium Arecibo 21 Centimeter Absorption-Line Survey. III. Techniques for Spectral Polarization and Results for Stokes V. *ApJS*, 151:271–297.

Hennebelle, P. and Chabrier, G. (2008). Analytical Theory for the Initial Mass Function: CO Clumps and Prestellar Cores. *ApJ*, 684:395–410.

Hennebelle, P. and Chabrier, G. (2009). Analytical Theory for the Initial Mass Function. II. Properties of the Flow. *ApJ*, 702:1428–1442.

Hennebelle, P. and Chabrier, G. (2013). Analytical Theory for the Initial Mass Function. III. Time Dependence and Star Formation Rate. *ApJ*, 770:150.

Hennebelle, P. and Falgarone, E. (2012). Turbulent molecular clouds. *A&ARv*, 20(1):55.

Henshaw, J. D., Longmore, S. N., Kruijssen, J. M. D., Davies, B., Bally, J., Barnes, A., Battersby, C., Burton, M., Cunningham, M. R., Dale, J. E., Ginsburg, A., Immer, K., Jones, P. A., Kendrew, S., Mills, E. A. C., Molinari, S., Moore, T. J. T., Ott, J., Pillai, T., Rathborne, J., Schilke, P., Schmiedeke, A., Testi, L., Walker, D., Walsh, A., and Zhang, Q. (2016). Molecular gas kinematics within the central 250 pc of the Milky Way. *MRNAS*, 457:2675–2702.

Heyer, M. H. and Brunt, C. M. (2004). The Universality of Turbulence in Galactic Molecular Clouds. *ApJ*, 615:L45–L48.

Heyminck, S., Graf, U. U., Gsten, R., Stutzki, J., Hbers, H. W., and Hartogh, P. (2012). GREAT: the SOFIA high-frequency heterodyne instrument. *A&A*, 542:L1.

Holdship, J. and Viti, S. (2016). Chemical tracers of pre-brown dwarf cores formed through turbulent fragmentation. *MNRAS*, 455:2371–2376.

Holdship, J., Viti, S., Jimenez-Serra, I., Lefloch, B., Codella, C., Podio, L., Benedettini, M., Fontani, F., Bachiller, R., Tafalla, M., and Ceccarelli, C. (2016). H2s in the L1157-B1 bow shock. *MNRAS*, 463:802–810.

Hollenbach, D., Kaufman, M. J., Neufeld, D., Wolfire, M., and Goicoechea, J. R. (2012). The chemistry of interstellar OH^+, H_2O^+, and H_3O^+: Inferring the Cosmic-Ray Ionization Rates from Observations of Molecular Ions. *ApJ*, 754:105.

Hollenbach, D. and McKee, C. F. (1979). Molecule formation and infrared emission in fast interstellar shocks. I Physical processes. *ApJS*, 41:555–592.

Hollenbach, D. and McKee, C. F. (1980). Molecule formation and infrared emission in fast interstellar shocks. II - Dissociation speeds for interstellar shock waves. *ApJ*, 241:L47–L50.

Hollenbach, D. and McKee, C. F. (1989). Molecule formation and infrared emission in fast interstellar shocks. III - Results for J shocks in molecular clouds. *ApJ*, 342:306–336.

Hollenbach, D. J. and Tielens, A. G. G. M. (1999). Photodissociation regions in the interstellar medium of galaxies. *Rev. Mod. Phys.*, 71:173–230.

Hollenbach, D. J., Werner, M. W., and Salpeter, E. E. (1971). Molecular Hydrogen in H i Regions. *ApJ*, 163:165.

Hopkins, P. F. (2013). A general theory of turbulent fragmentation. *MNRAS*, 430:1653–1693.

Hopkins, P. F. (2015). A new class of accurate, mesh-free hydrodynamic simulation methods. *MNRAS*, 450:53–110.

Hopkins, P. F. and Lee, H. (2016). The fundamentally different dynamics of dust and gas in molecular clouds. *MNRAS*, 456:4174–4190.

Iglesias, E. R. and Silk, J. (1978). Nonequilibrium chemistry in shocked molecular clouds. *ApJ*, 226:851–857.

Igra, O. and Ben-Dor, G. (1988). Dusty Shock Waves. *Applied Mechanics Reviews*, 41(11):379–437.

Immer, K., Kauffmann, J., Pillai, T., Ginsburg, A., and Menten, K. M. (2016). Temperature structures in Galactic center clouds. Direct evidence for gas heating via turbulence. *A&A*, 595:A94.

Isella, A., Guidi, G., Testi, L., Liu, S., Li, H., Li, S., Weaver, E., Boehler, Y., Carperter, J. M., De Gregorio-Monsalvo, I., Manara, C. F., Natta, A., Pérez, L. M., Ricci, L., Sargent, A., Tazzari, M., and Turner, N. (2016). Ringed Structures of the HD 163296 Protoplanetary Disk Revealed by ALMA. *Phys. Rev. Lett.*, 117:251101.

Johansen, A., Henning, T., and Klahr, H. (2006). Dust Sedimentation and Self-sustained Kelvin-Helmholtz Turbulence in Protoplanetary Disk Midplanes. *ApJ*, 643:1219–1232.

Johansen, A., Oishi, J. S., Mac Low, M.-M., Klahr, H., Henning, T., and Youdin, A. (2007). Rapid planetesimal formation in turbulent circumstellar disks. *Nature*, 448:1022–1025.

Jones, P. A., Burton, M. G., Cunningham, M. R., Requena-Torres, M. A., Menten, K. M., Schilke, P., Belloche, A., Leurini, S., Martn-Pintado, J., Ott, J., and Walsh, A. J. (2012). Spectral imaging of the Central Molecular Zone in multiple 3-mm molecular lines. *MNRAS*, 419:2961–2986.

Kainulainen, J., Hacar, A., Alves, J., Beuther, H., Bouy, H., and Tafalla, M. (2016). Gravitational fragmentation caught in the act: the filamentary Musca molecular cloud. *A&A*, 586:A27.

Kamenetzky, J., Glenn, J., Rangwala, N., Maloney, P., Bradford, M., Wilson, C. D., Bendo, G. J., Baes, M., Boselli, A., Cooray, A., Isaak, K. G., Lebouteiller, V., Madden, S., Panuzzo, P., Schirm, M. R. P., Spinoglio, L., and Wu, R. (2012). Herschel-SPIRE Imaging Spectroscopy of Molecular Gas in M82. *ApJ*, 753:70.

Kanagawa, K. D., Muto, T., Tanaka, H., Tanigawa, T., Takeuchi, T., Tsukagoshi, T., and Momose, M. (2015). Mass Estimates of a Giant Planet in a Protoplanetary Disk from the Gap Structures. *ApJ*, 806:L15.

Kennel, C. F., Blandford, R. D., and Coppi, P. (1989). MHD Intermediate Shock Discontinuities. Part 1. Rankine–Hugoniot Conditions. *J. Plas. Phys.*, 42(02):299–319.

Kim, C.-G. and Ostriker, E. C. (2015). Momentum Injection by Supernovae in the Interstellar Medium. *ApJ*, 802:99.

Klessen, R. S. and Hennebelle, P. (2010). Accretion-driven turbulence as universal process: galaxies, molecular clouds, and protostellar disks. *A&A*, 520:A17.

Kolmogorov, A. N. (1962). A refinement of previous hypotheses concerning the local structure of turbulence in a viscous incompressible fluid at high Reynolds number. *JFM*, 13(01):82.

Kriebel, A. R. (1964). Analysis of Normal Shock Waves in Particle Laden Gas. *J. Basic Eng*, 86(4):655.

Kritsuk, A. G., Norman, M. L., Padoan, P., and Wagner, R. (2007). The Statistics of Supersonic Isothermal Turbulence. *ApJ*, 665:416–431.

Kritsuk, A. G., Ustyugov, S. D., Norman, M. L., and Padoan, P. (2009). Simulations of Supersonic Turbulence in Molecular Clouds: Evidence for a New Universality. In Pogorelov, N. V., Audit, E., Colella, P., and Zank, G. P., editors, *Numerical Modeling of Space Plasma Flows: ASTRONUM-2008*, volume 406, page 15, eprint: arXiv:0902.3222.

Krumholz, M. R. (2014a). The big problems in star formation: The star formation rate, stellar clustering, and the initial mass function. *Physics Reports*, 539:49–134.

Krumholz, M. R. (2014b). DESPOTIC - a new software library to Derive the Energetics and SPectra of Optically Thick Interstellar Clouds. *MNRAS*, 437:1662–1680.

Krumholz, M. R., Klein, R. I., and McKee, C. F. (2007). Radiation-Hydrodynamic Simulations of Collapse and Fragmentation in Massive Protostellar Cores. *ApJ*, 656:959–979.

Krumholz, M. R. and McKee, C. F. (2005). A General Theory of Turbulence-regulated Star Formation, from Spirals to Ultraluminous Infrared Galaxies. *ApJ*, 630:250–268.

Kumar, A. and Fisher, R. T. (2013). The astrochemical evolution of turbulent giant molecular clouds: physical processes and method of solution for hydrodynamic, embedded starless clouds. *MNRAS*, 431(1):455–476.

Kwan, J. H., Gatley, I., Merrill, K. M., Probst, R., and Weintraub, D. A. (1977). On the molecular hydrogen emission at the Orion Nebula. *ApJ*, 216:713–723.

Kwok, S. (1975). Radiation pressure on grains as a mechanism for mass loss in red giants. *ApJ*, 198:583–591.

Lada, C. J. (1985). Cold outflows, energetic winds, and enigmatic jets around young stellar objects. *ARA&A*, 23:267–317.

Laibe, G. and Price, D. J. (2011). DUSTYBOX and DUSTYWAVE: two test problems for numerical simulations of two-fluid astrophysical dust-gas mixtures. *MNRAS*, 418:1491–1497.

Laibe, G. and Price, D. J. (2012a). Dusty gas with smoothed particle hydrodynamics - I. Algorithm and test suite. *MNRAS*, 420:2345–2364.

Laibe, G. and Price, D. J. (2012b). Dusty gas with smoothed particle hydrodynamics - II. Implicit timestepping and astrophysical drag regimes. *MNRAS*, 420:2365–2376.

Larson, R. B. (1981). Turbulence and star formation in molecular clouds. *MNRAS*, 194:809–826.

Larson, R. B. (2003). The physics of star formation. *Reports on Progress in Physics*, 66:1651–1697.

Larson, R. L., Evans, II, N. J., Green, J. D., and Yang, Y.-L. (2015). Evidence for Decay of Turbulence by MHD Shocks in Molecular Clouds via CO Emission. *ApJ*, 806(1):70.

Launhardt, R., Stutz, A. M., Schmiedeke, A., Henning, T., Krause, O., Balog, Z., Beuther, H., Birkmann, S., Hennemann, M., Kainulainen, J., Khanzadyan, T.,

Linz, H., Lippok, N., Nielbock, M., Pitann, J., Ragan, S., Risacher, C., Schmalzl, M., Shirley, Y. L., Stecklum, B., Steinacker, J., and Tackenberg, J. (2013). The Earliest Phases of Star Formation (EPoS): a Herschel key project. The thermal structure of low-mass molecular cloud cores. *A&A*, 551:A98.

Lazarian, A., Vishniac, E. T., and Cho, J. (2004). Magnetic Field Structure and Stochastic Reconnection in a Partially Ionized Gas. *ApJ*, 603:180–197.

Le Gal, R., Hily-Blant, P., Faure, A., Pineau des Forêts, G., Rist, C., and Maret, S. (2014). Interstellar chemistry of nitrogen hydrides in dark clouds. *A&A*, 562:A83.

Lehmann, A., Federrath, C., and Wardle, M. (2016). SHOCKFIND - an algorithm to identify magnetohydrodynamic shock waves in turbulent clouds. *MNRAS*, 463(1):1026–1039.

Lehmann, A. and Wardle, M. (2016). Signatures of fast and slow magnetohydrodynamic shocks in turbulent molecular clouds. *MNRAS*, 455(2):2066–2077.

Lesaffre, P., Pineau des Forêts, G., Godard, B., Guillard, P., Boulanger, F., and Falgarone, E. (2013). Low-velocity shocks: signatures of turbulent dissipation in diffuse irradiated gas. *A&A*, 550:106.

Leung, C. M., Kutner, M. L., and Mead, K. N. (1982). On the origin and structure of isolated dark globules. *ApJ*, 262:583–589.

Lithwick, Y. and Goldreich, P. (2001). Compressible Magnetohydrodynamic Turbulence in Interstellar Plasmas. *ApJ*, 562:279–296.

Loenen, A. F., Spaans, M., Baan, W. A., and Meijerink, R. (2008). Mechanical feedback in the molecular ISM of luminous IR galaxies. *A&A*, 488:L5–L8.

Lorén-Aguilar, P. and Bate, M. R. (2014). Two-fluid dust and gas mixtures in smoothed particle hydrodynamics: a semi-implicit approach. *MNRAS*, 443:927–945.

Mac Low, M.-M. and Klessen, R. S. (2004). Control of star formation by supersonic turbulence. *Rev. Mod. Phys.*, 76:125–194.

McCray, R. and Snow, T. P. (1979). The violent interstellar medium. *ARA&A*, 17:213–240.

McElroy, D., Walsh, C., Markwick, A. J., Cordiner, M. A., Smith, K., and Millar, T. J. (2013). The UMIST database for astrochemistry 2012. *A&A*, 550:36.

McKee, C. F., Li, P. S., and Klein, R. I. (2010). Sub-Alfvénic Non-ideal MHD Turbulence Simulations with Ambipolar Diffusion. II. Comparison with Observation, Clump Properties, and Scaling to Physical Units. *ApJ*, 720:1612–1634.

McKee, C. F. and Ostriker, E. C. (2007). Theory of Star Formation. *ARA&A*, 45:565–687.

Meijerink, R. and Spaans, M. (2005). Diagnostics of irradiated gas in galaxy nuclei. I. A far-ultraviolet and X-ray dominated region code. *A&A*, 436:397–409.

Meijerink, R., Spaans, M., Loenen, A. F., and van der Werf, P. P. (2011). Star formation in extreme environments: the effects of cosmic rays and mechanical heating. *A&A*, 525:A119.

Meyer, C. D., Balsara, D. S., Burkhart, B., and Lazarian, A. (2014). Observational diagnostics for two-fluid turbulence in molecular clouds as suggested by simulations. *MNRAS*, 439:2197–2210.

Milam, S. N., Savage, C., Brewster, M. A., Ziurys, L. M., and Wyckoff, S. (2005). The 12c/13c Isotope Gradient Derived from Millimeter Transitions of CN: The Case for Galactic Chemical Evolution. *ApJ*, 634:1126–1132.

Mills, E. A. C. and Morris, M. R. (2013). Detection of Widespread Hot Ammonia in the Galactic Center. *ApJ*, 772:105.

Miura, H. (1972). Weak Shock Waves in a Dusty Gas. *Journal of the Physical Society of Japan*, 33(6):1688–1692.

Molinari, S., Bally, J., Noriega-Crespo, A., Compigne, M., Bernard, J. P., Paradis, D., Martin, P., Testi, L., Barlow, M., Moore, T., Plume, R., Swinyard, B., Zavagno, A., Calzoletti, L., Di Giorgio, A. M., Elia, D., Faustini, F., Natoli, P., Pestalozzi, M., Pezzuto, S., Piacentini, F., Polenta, G., Polychroni, D., Schisano, E., Traficante, A., Veneziani, M., Battersby, C., Burton, M., Carey, S., Fukui, Y., Li, J. Z., Lord, S. D., Morgan, L., Motte, F., Schuller, F., Stringfellow, G. S., Tan, J. C., Thompson, M. A., Ward-Thompson, D., White, G., and Umana, G. (2011). A 100 pc Elliptical and Twisted Ring of Cold and Dense Molecular Clouds Revealed by Herschel Around the Galactic Center. *ApJ*, 735:L33.

Monaghan, J. J. and Kocharyan, A. (1995). SPH simulation of multi-phase flow. *Computer Physics Communications*, 87:225–235.

Morris, M. and Serabyn, E. (1996). The Galactic Center Environment. *ARA&A*, 34:645–702.

Mullan, D. J. (1971). The structure of transverse hydromagnetic shocks in regions oflow ionization. *MNRAS*, 153:145.

Myers, A. T., Klein, R. I., Krumholz, M. R., and McKee, C. F. (2014). Star cluster formation in turbulent, magnetized dense clumps with radiative and outflow feedback. *MNRAS*, 439:3420–3438.

Myers, P. C. (1983). Dense cores in dark clouds. III - Subsonic turbulence. *ApJ*, 270:105–118.

Myers, P. C., Dame, T. M., Thaddeus, P., Cohen, R. S., Silverberg, R. F., Dwek, E., and Hauser, M. G. (1986). Molecular clouds and star formation in the inner galaxy - A comparison of CO, H II, and far-infrared surveys. *ApJ*, 301:398–422.

Nakamura, F. and Li, Z.-Y. (2007). Protostellar Turbulence Driven by Collimated Outflows. *ApJ*, 662:395–412.

Neufeld, D. A. and Dalgarno, A. (1989). Fast molecular shocks. I - Reformation of molecules behind a dissociative shock. *ApJ*, 340:869–893.

Neufeld, D. A. and Kaufman, M. J. (1993). Radiative Cooling of Warm Molecular Gas. *ApJ*, 418:263.

Neufeld, D. A., Lepp, S., and Melnick, G. J. (1995). Thermal Balance in Dense Molecular Clouds: Radiative Cooling Rates and Emission-Line Luminosities. *ApJS*, 100:132.

Offner, S. S. R. and Arce, H. G. (2014). Investigations of Protostellar Outflow Launching and Gas Entrainment: Hydrodynamic Simulations and Molecular Emission. *ApJ*, 784:61.

Oka, T., Geballe, T. R., Goto, M., Usuda, T., and McCall, B. J. (2005). Hot and Diffuse Clouds near the Galactic Center Probed by Metastable H+31,. *ApJ*, 632:882–893.

Omukai, K., Hosokawa, T., and Yoshida, N. (2010). Low-metallicity Star Formation: Prestellar Collapse and Protostellar Accretion in the Spherical Symmetry. *ApJ*, 722:1793–1815.

Ossenkopf, V. and Mac Low, M.-M. (2002). Turbulent velocity structure in molecular clouds. *A&A*, 390:307–326.

Ott, J., Wei, A., Staveley-Smith, L., Henkel, C., and Meier, D. S. (2014). ATCA Survey of Ammonia in the Galactic Center: The Temperatures of Dense Gas Clumps between Sgr A* and Sgr B2. *ApJ*, 785:55.

Paardekooper, S.-J. and Mellema, G. (2006a). RODEO: a new method for planet-disk interaction. *A&A*, 450:1203–1220.

Paardekooper, S.-J. and Mellema, G. (2006b). dust flow in gas disks in the presence of embedded planets. *Astronomy and Astrophysics*, 453:1129–1140.

Padoan, P., Haugblle, T., and Nordlund, Å. (2014). Infall-driven Protostellar Accretion and the Solution to the Luminosity Problem. *ApJ*, 797:32.

Padoan, P., Juvela, M., Goodman, A. A., and Nordlund, Å. (2001). The Turbulent Shock Origin of Proto-Stellar Cores. *ApJ*, 553:227–234.

Padoan, P. and Nordlund, Å. (1999). A super-Alfvénic model of dark clouds. *ApJ*, 526:279.

Padoan, P. and Nordlund, Å. (2002). The Stellar Initial Mass Function from Turbulent Fragmentation. *ApJ*, 576:870–879.

Padoan, P. and Nordlund, Å. (2011). The Star Formation Rate of Supersonic Magnetohydrodynamic Turbulence. *ApJ*, 730:40.

Padoan, P., Nordlund, Å., and Jones, B. J. T. (1997). The universality of the stellar initial mass function. *MNRAS*, 288:145–152.

Padoan, P., Pan, L., Haugblle, T., and Nordlund, . (2016). Supernova Driving. I. The Origin of Molecular Cloud Turbulence. *ApJ*, 822:11.

Pakmor, R., Bauer, A., and Springel, V. (2011). Magnetohydrodynamics on an unstructured moving grid. *MNRAS*, 418:1392–1401.

Pellegrini, E. W., Smith (PI, J. D., Wolfire, M. G., Draine, B. T., Crocker, A. F., Croxall, K. V., van der Werf, P., Dale, D. A., Rigopoulou, D., Wilson, C. D., Schinnerer, E., Groves, B. A., Kreckel, K., Sandstrom, K. M., Armus, L., Calzetti, D., Murphy, E. J., Walter, F., Koda, J., Bayet, E., Beirao, P., Bolatto, A. D., Bradford, M., Brinks, E., Hunt, L., Kennicutt, R., Knapen, J. H., Leroy, A. K., Rosolowsky, E., Vigroux, L., and Hopwood, R. H. B. (2013). Shock Excited Molecules in NGC 1266: ULIRG Conditions at the Center of a Bulge-dominated Galaxy. *ApJ*, 779:L19.

Pety, J. and Falgarone, E. (2000). The elusive structure of the diffuse molecular gas: shocks or vortices in compressible turbulence? *A&A*, 356:279–286.

Pilbratt, G. L., Riedinger, J. R., Passvogel, T., Crone, G., Doyle, D., Gageur, U., Heras, A. M., Jewell, C., Metcalfe, L., Ott, S., and Schmidt, M. (2010). Herschel Space Observatory. An ESA facility for far-infrared and submillimetre astronomy. *A&A*, 518:L1.

Pineau des Forêts, G., Roueff, E., and Flower, D. R. (1990). The formation of nitrogen-bearing species in dark interstellar clouds. *MNRAS*, 244:668–674.

Pineau des Forêts, G., Roueff, E., Schilke, P., and Flower, D. R. (1993). Sulphur-bearing molecules as tracers of shocks in interstellar clouds. *MNRAS*, 262:915–928.

Planck Collaboration, Abergel, A., Ade, P. A. R., Aghanim, N., et al. (2011). *Planck* early results. XXV. Thermal dust in nearby molecular clouds. *A&A*, 536:A25.

Planck Collaboration, Ade, P. A. R., Aghanim, N., Alves, M. I. R., et al. (2016a). *Planck* intermediate results. XXXIII. Signature of the magnetic field geometry of interstellar filaments in dust polarization maps. *A&A*, 586:A136.

Planck Collaboration, Ade, P. A. R., Aghanim, N., Alves, M. I. R., et al. (2016b). *Planck* intermediate results. XXXV. Probing the role of the magnetic field in the formation of structure in molecular clouds. *A&A*, 586:A138.

Pon, A., Caselli, P., Johnstone, D., Kaufman, M., Butler, M. J., Fontani, F., Jiménez-Serra, I., and Tan, J. C. (2015). Mid-J CO shock tracing observations of infrared dark clouds. I. *A&A*, 577:A75.

Pon, A., Johnstone, D., Caselli, P., Fontani, F., Palau, A., Butler, M. J., Kaufman, M., Jiménez-Serra, I., and Tan, J. C. (2016a). Mid-J CO shock tracing observations of infrared dark clouds. II. Low-J CO constraints on excitation, depletion, and kinematics. *A&A*, 587:A96.

Pon, A., Johnstone, D., J. Kaufman, M., Caselli, P., and Plume, R. (2014). Mid-J CO observations of Perseus B1-East 5: evidence for turbulent dissipation via low-velocity shocks. *MNRAS*, 445(2):1508–1520.

Pon, A., Johnstone, D., and Kaufman, M. J. (2012). Molecular Tracers of Turbulent Shocks in Giant Molecular Clouds. *ApJ*, 748:25.

Pon, A., Kaufman, M. J., Johnstone, D., Caselli, P., Fontani, F., Butler, M. J., Jimnez-Serra, I., Palau, A., and Tan, J. C. (2016b). Mid-J CO Shock Tracing Observations of Infrared Dark Clouds. III. SLED Fitting. *ApJ*, 827:107.

Prasad, S. S. and Tarafdar, S. P. (1983). UV radiation field inside dense clouds - Its possible existence and chemical implications. *ApJ*, 267:603–609.

Price, D. J. and Bate, M. R. (2008). The effect of magnetic fields on star cluster formation. *MNRAS*, 385:1820–1834.

Price, D. J. and Bate, M. R. (2009). Inefficient star formation: the combined effects of magnetic fields and radiative feedback. *MRNAS*, 398:33–46.

Price, D. J. and Federrath, C. (2010). A comparison between grid and particle methods on the statistics of driven, supersonic, isothermal turbulence. *MNRAS*, 406:1659–1674.

Robertson, B. and Goldreich, P. (2012). Adiabatic Heating of Contracting Turbulent Fluids. *ApJ*, 750:L31.

Roman-Duval, J., Federrath, C., Brunt, C., Heyer, M., Jackson, J., and Klessen, R. S. (2011). The Turbulence Spectrum of Molecular Clouds in the Galactic Ring Survey: A Density-dependent Principal Component Analysis Calibration. *The Astrophysical Journal*, 740:120.

Ruge, J. P., Flock, M., Wolf, S., Dzyurkevich, N., Fromang, S., Henning, T., Klahr, H., and Meheut, H. (2016). Gaps, rings, and non-axisymmetric structures in protoplanetary disks: Emission from large grains. *A&A*, 590:A17.

Saito, T., Marumoto, M., and Takayama, K. (2003). Numerical investigations of shock waves in gas-particle mixtures. *Shock Waves*, 13(4):299–322.

Sanders, D. B., Scoville, N. Z., and Solomon, P. M. (1985). Giant molecular clouds in the Galaxy. II - Characteristics of discrete features. *ApJ*, 289:373–387.

Schaal, K. and Springel, V. (2015). Shock finding on a moving mesh - I. Shock statistics in non-radiative cosmological simulations. *MNRAS*, 446:3992–4007.

Schilke, P., Walmsley, C. M., Pineau des Forêts, G., and Flower, D. R. (1997). SiO production in interstellar shocks. *A&A*, 321:293–304.

Schneider, N., André, P., Knyves, V., Bontemps, S., Motte, F., Federrath, C., Ward-Thompson, D., Arzoumanian, D., Benedettini, M., Bressert, E., Didelon, P., Di Francesco, J., Griffin, M., Hennemann, M., Hill, T., Palmeirim, P., Pezzuto, S., Peretto, N., Roy, A., Rygl, K. L. J., Spinoglio, L., and White, G. (2013). What Determines the Density Structure of Molecular Clouds? A Case Study of Orion B with Herschel. *ApJ*, 766:L17.

Shetty, R., Beaumont, C. N., Burton, M. G., Kelly, B. C., and Klessen, R. S. (2012). The linewidth-size relationship in the dense interstellar medium of the Central Molecular Zone. *MNRAS*, 425(1):720–729.

Shu, F. H. (1977). Self-similar collapse of isothermal spheres and star formation. *ApJ*, 214:488–497.

Shu, F. H., Adams, F. C., and Lizano, S. (1987). Star formation in molecular clouds: observation and theory. *ARA&A*, 25(1):23–81.

Smith, M. D. and Brand, P. W. J. L. (1990). Signatures of C-shocks in molecular clouds. *MNRAS*, 243:498–503.

Smith, M. D., Mac Low, M.-M., and Heitsch, F. (2000a). The distribution of shock waves in driven supersonic turbulence. *A&A*, 362:333–341.

Smith, M. D., Mac Low, M.-M., and Zuev, J. M. (2000b). The shock waves in decaying supersonic turbulence. *A&A*, 356:287–300.

Smith, R. J., Glover, S. C. O., and Klessen, R. S. (2014). On the nature of star-forming filaments - I. Filament morphologies. *MRNAS*, 445:2900–2917.

Smith, R. J., Glover, S. C. O., Klessen, R. S., and Fuller, G. A. (2016). On the nature of star-forming filaments - II. Subfilaments and velocities. *MRNAS*, 455:3640–3655.

Sod, G. A. (1978). A survey of several finite difference methods for systems of nonlinear hyperbolic conservation laws. *Journal of Computational Physics*, 27:1–31.

Solomon, P. M., Rivolo, A. R., Barrett, J., and Yahil, A. (1987). Mass, luminosity, and line width relations of Galactic molecular clouds. *ApJ*, 319:730–741.

Spitzer, Jr., L. (1990). Theories of the hot interstellar gas. *ARA&A*, 28:71–101.

Springel, V. (2005). The cosmological simulation code GADGET-2. *MNRAS*, 364:1105–1134.

Springel, V. (2010). E pur si muove: Galilean-invariant cosmological hydrodynamical simulations on a moving mesh. *MNRAS*, 401:791–851.

Stephens, I. W., Evans, J. M., Xue, R., Chu, Y.-H., Gruendl, R. A., and Segura-Cox, D. M. (2014). Spitzer Observations of Dust Emission from H II Regions in the Large Magellanic Cloud. *ApJ*, 784:147.

Stone, J., Ostriker, E., and Gammie, C. (1998). Dissipation in compressible magnetohydrodynamic turbulence. *ApJ*, 508:L99.

Stone, J. M., Gardiner, T. A., Teuben, P., Hawley, J. F., and Simon, J. B. (2008). Athena: A New Code for Astrophysical MHD. *ApJS*, 178:137–177.

Takahira, K., Tasker, E. J., and Habe, A. (2014). Do Cloud-Cloud Collisions Trigger High-mass Star Formation? I. Small Cloud Collisions. *ApJ*, 792:63.

Tilley, D. A. and Balsara, D. S. (2011). Two-fluid ambipolar diffusion for molecular clouds with realistic heating and cooling. *MNRAS*, 415:3681–3692.

Toth, G. (1994). Numerical study of two-fluid C-type shock waves. *ApJ*, 425:171–194.

Troland, T. H. and Crutcher, R. M. (2008). Magnetic Fields in Dark Cloud Cores: Arecibo OH Zeeman Observations. *ApJ*, 680:457–465.

van der Tak, F. F. S., Black, J. H., Schier, F. L., Jansen, D. J., and van Dishoeck, E. F. (2007). A computer program for fast non-LTE analysis of interstellar line spectra. With diagnostic plots to interpret observed line intensity ratios. *A&A*, 468:627–635.

Vázquez-Semadeni, E., Ballesteros-Paredes, J., and Rodrguez, L. F. (1997). A Search for Larson-type Relations in Numerical Simulations of the ISM: Evidence for Nonconstant Column Densities. *ApJ*, 474:292–307.

Vázquez-Semadeni, E., Coln, P., Gmez, G. C., Ballesteros-Paredes, J., and Watson, A. W. (2010). Molecular Cloud Evolution. III. Accretion Versus Stellar Feedback. *ApJ*, 715:1302–1317.

Waagan, K., Federrath, C., and Klingenberg, C. (2011). A robust numerical scheme for highly compressible magnetohydrodynamics: Nonlinear stability, implementation and tests. *J. Comput. Phys.*, 230:3331–3351.

Wagner, A. F. and Graff, M. M. (1987). Oxygen chemistry of shocked interstellar clouds. I - Rate constants for thermal and nonthermal internal energy distributions. *ApJ*, 317:423–431.

Walsh, C., Juhsz, A., Meeus, G., Dent, W. R. F., Maud, L. T., Aikawa, Y., Millar, T. J., and Nomura, H. (2016). ALMA Reveals the Anatomy of the mm-sized Dust and Molecular Gas in the HD 97048 Disk. *ApJ*, 831:200.

Wang, P., Li, Z.-Y., Abel, T., and Nakamura, F. (2010). Outflow Feedback Regulated Massive Star Formation in Parsec-Scale Cluster-Forming Clumps. *ApJ*, 709:27–41.

Wardle, M. (2007). Magnetic fields in protoplanetary disks. *Ap&SS*, 311(1-3):35–45.

Wilson, B. A., Dame, T. M., Masheder, M. R. W., and Thaddeus, P. (2005). A uniform CO survey of the molecular clouds in Orion and Monoceros. *A&A*, 430:523–539.

Wolfire, M. G., Hollenbach, D., McKee, C. F., Tielens, A. G. G. M., and Bakes, E. L. O. (1995). The neutral atomic phases of the interstellar medium. *ApJ*, 443:152–168.

Wu, C. C. (1987). On MHD intermediate shocks. *GeoRL*, 14:668–671.

Yang, C.-C. and Johansen, A. (2016). Integration of Particle-gas Systems with Stiff Mutual Drag Interaction. *ApJS*, 224:39.

Yusef-Zadeh, F., Hewitt, J. W., Wardle, M., Tatischeff, V., Roberts, D. A., Cotton, W., Uchiyama, H., Nobukawa, M., Tsuru, T. G., Heinke, C., and Royster, M. (2013a). Interacting Cosmic Rays with Molecular Clouds: A Bremsstrahlung Origin of Diffuse High-energy Emission from the Inner 21 of the Galactic Center. *ApJ*, 762:33.

Yusef-Zadeh, F. and Morris, M. (1987). The linear filaments of the radio arc near the Galactic center. *ApJ*, 322:721–728.

Yusef-Zadeh, F., Wardle, M., Lis, D., Viti, S., Brogan, C., Chambers, E., Pound, M., and Rickert, M. (2013b). 74 MHz Nonthermal Emission from Molecular Clouds: Evidence for a Cosmic Ray Dominated Region at the Galactic Center. *JPCA*, 117:9404–9419.

Zweibel, E. G. and Josafatsson, K. (1983). Hydromagnetic wave dissipation in molecular clouds. *ApJ*, 270:511–518.